UNIVERSITY OF LEEDS

Characterising North Atlantic Eddy Driven Jet Variability

Jacob Perez

Submitted in accordance with the requirements for the degree of PhD in Fluid Dynamics

The University of Leeds

Faculty of Engineering

School of Computing

May 2025

Abstract

The eddy-driven jet (EDJ) over the North Atlantic drives variability in weather and climate over Europe, yet its characterisation has relied on zonally averaged diagnostics that mask its full spatio-temporal complexity. This thesis develops and applies a novel two-dimensional object-based framework to extract key EDJ features such as the latitude, strength, and tilt measured using the daily 850hPa zonal wind fields. The object method shows a unimodal climatologtical distribution of EDJ latitude, in contrast to the trimodal distribution found for the conventional Jet Latitude Index (JLI). The difference is shown to be partly due to the poor performance of the JLI when the jet is weak, broad, tilted or split.

Using this new framework, I demonstrate robust links between EDJ configurations and large-scale modes of atmospheric variability: southerly, weak, and positively tilted jets coincide with negative NAO/East-Atlantic phases and enhanced surface blocking; conversely, northerly, strong, and negatively tilted jets coincide with positive NAO conditions and zonal flow. Using data from the seasonal forecasting model GloSea5, I show that models have skill in predicting the winter EDJ latitude but have no skill for the EDJ tilt and strength. The skillful forecasts for the EDJ latitude exhibit a weak signal-to-noise ratio comparbale to what has been found for the winter NAO.

Finally, I investigate the influence of teleconnections from ENSO, QBO, and MJO with the new methodology. El Niño favours early winter poleward, stronger, westward tilted jets, while La Niña produces the opposite shifts; easterly QBO phases promote persistent equatorward, weakened jets; and certain MJO phases modulate EDJ onset and tilt on subseasonal

timescales. These results underscore the importance of multidimensional jet diagnostics for improved understanding and prediction of mid-latitude climate variability and extremes.

Intellectual Property

The candidate confirms that the work submitted is his own and that appropriate credit has been given where reference has been made to the work of others.

Acknowledgements

I would firstly like to thank everyone on my supervisory team, Prof. Amanda Maycock, Dr. Stephen Griffiths, Dr. Steven Hardiman, and Dr. Christine McKenna. Without your unwavering support and guidance, especially during the pandemic years, I would never have finished this thesis. I am also grateful to the CDT for Fluid Dynamics, thank you to everyone for the continued support throughout my time at the University of Leeds.

Then I want to thank my family, my Mum Janine, my Dad Steven and my sister Rebekah, thank you for all your love and support throughout my academic journey. I know it did not start well, but you never gave up on me and for that I could never thank you enough.

Lastly I would I like to thank Ashleigh, thank you for your unwavering support and advice during stressful times.

Contents

1 Introduction **1**

1.1 Focus 5

1.2 Research Questions 7

1.2.1 Structure of this thesis 7

2 Background **9**

2.1 The General Circulation 9

2.1.1 Jet Streams 10

2.2 The Eddy-Driven Jet Stream 13

2.2.1 Eddies in the atmosphere 13

2.2.2 Wave-Mean Flow Interaction 16

2.2.3 Rossby Wave Propagation 21

2.3 Regimes in the Atmosphere 24

2.3.1 Regimes in Simplified Models 24

2.3.2 Regimes in Observations 27

2.3.3 Correct number of regimes? 33

2.4 Remote Drivers of North Atlantic Variability 36

2.5 Predictability of the EDJ 44

2.6 Summary 45

3 Characterising the North Atlantic eddy-driven jet using two dimensional moment analysis **48**

3.1 Introduction 48

3.2 Data and methods 51

3.2.1 Definition of the JLI and the JAI 51

3.3 Eddy-Driven Jet Objects 52

3.3.1 EDJO identification 52
3.3.2 Moments 53
3.3.3 Example cases 56
3.4 Temporal variability 58
3.4.1 Winter 2016/17 58
3.4.2 Winter 1998/99 59
3.4.3 Persistence 63
3.5 Winter statistics 64
3.5.1 Daily Distributions 64
3.5.2 Source of differences in the JLI and $\overline{\phi}$ 66
3.5.3 Relationship between moments metrics 67
3.6 Relationship of EDJOs and Large-Scale patterns of North Atlantic variability 72
3.6.1 NAO/EA phase space 75
3.6.2 Multiple Object Days 78
3.7 Conclusions and Discussion 79
Appendix: Robustness of EDJO identification 80
3.7.1 Choice of U^*_{850}, L^* and L^*_λ 80
3.7.2 Sensitivity to inclusion of L^* and L^*_λ 80

4 Predictability of the Eddy-Driven Jet 82
4.1 Introduction 82
4.2 Data and Methods 83
4.2.1 Model and Observations 83
4.2.2 EDJO identification 84
4.2.3 Definition of Large-Scale Patterns 85
4.3 Assessing Model Differences 85
4.4 Representation of EDJOs in GloSea5 86
4.4.1 Daily distributions 86
4.4.2 Time varying statistics 88
4.5 North Atlantic Variability and Predictability 91
4.5.1 Seasonal Predictability 96
4.6 Conclusions and Discussion 97

5 Configurations of the Eddy-Driven Jet and their relationship with Surface Climate 102
5.1 Introduction . . . 102
5.2 Spatial Correlations . . . 103
5.2.1 Precipitation . . . 103
5.2.2 2m Temperature . . . 107
5.3 EDJ Configuration and Impacts . . . 108
5.4 UK Extremes . . . 115
5.5 Conclusions and Discussion . . . 121

6 Sub-Seasonal and Seasonal drivers of the Eddy-Driven Jet 124
6.1 Introduction . . . 124
6.2 Data and Methods . . . 125
6.2.1 Datasets . . . 125
6.2.2 El Niño Southern Oscillation . . . 126
6.2.3 Quasi-Biennial Oscillation . . . 126
6.2.4 Statistical Testing for ENSO and the QBO . . . 126
6.2.5 Madden-Julian Oscillation . . . 127
6.3 Seasonal Variability . . . 132
6.3.1 El Niño Southern Oscillation . . . 132
6.3.2 Quasi-Biennial Oscillation . . . 138
6.4 Sub-seasonal variability associated with the MJO . . . 141
6.4.1 NAO and MJO response . . . 141
6.4.2 EDJ and MJO response . . . 142
6.5 Conclusions and Discussion . . . 144
6.5.1 Seasonal variability . . . 146
6.5.2 Sub-seasonal variability . . . 148

7 Conclusions and Further Work 149
7.1 Further Work . . . 152

References 155

List of Figures

1.1 Schematic illustration of Earth's atmospheric circulation cells (Hadley, Ferrel, and Polar cells), displaying their vertical and latitudinal structure from the equator to the pole. Highlighted are key features including the Intertropical Convergence Zone (ITCZ), subtropical and mid-latitude (eddy-driven) jet streams, prevailing wind patterns (easterly trade winds, westerlies, and polar easterlies), and significant atmospheric pressure zones (subtropical highs, subpolar lows, and polar highs). The tropopause marks the boundary separating the troposphere from the stratosphere. Figure taken from Royal Meteorological Society (2025). 2

1.2 Climatological mean zonal wind speeds (ms^{-1}) from NCEP/NCAR reanalysis data, displayed as latitude-pressure cross-sections. The top panel shows the annual climatology, while the middle and bottom panels depict seasonal climatologies for December-January-February (DJF) and June-July-August (JJA), respectively. Positive (red-yellow) values indicate westerly winds, and negative (blue) values indicate easterly winds. Jet streams are clearly identifiable as regions of maximum westerly wind speeds located near the tropopause at approximately 200 hPa (approximately 10–15 km altitude). Figure taken from UC-Davis Climate Dynamics ATM 241 Course Materials (2025). 4

1.3 Eddy-Driven Jet regimes found by the Jet Latitude Index (JLI) of Woollings et al. (2010). 6

2.1 Time and spatial scales of different physical phenomena in the atmosphere Cullen and Brown, 2009. 10
2.2 a) Annual mean zonally-averaged zonal wind (filled contours) and the zonally-averaged temperature (red contours). b) Annual mean zonally averaged zonal winds at the surface. Image taken from Figure 14.2 of Vallis, 2017. 12
2.3 Schematic of the streamlines (black with arrows) and isotherms (coloured) associated with a large-scale atmospheric disturbance. Signs at the bottom are deviations of the zonal wind (u), meridional wind (v) and temperature (T) from there respective zonal average. Figure taken from Hartmann, 2016. 15
2.4 Eliassen-Palm vector (arrows) and divergence (contours) of a baroclinic lifecycle (a - c) and the time average (d) from Edmon et al., 1980. Height on the y-axis in mb and latitude in the x-axis. 19
2.5 Perturbation vorticity field and induced velocity field (dashed arrows) for a meridionally displaced chain of fluid parcels. The heavy wavy line shows original perturbation position; the light line shows westward displacement of the pattern due to advection by the induced velocity. Figure taken from Holton and Hakim, 2013. 22
2.6 The Lorenz butterfly attractor, illustrating the trajectories oscillating between two fixed points in phase space. 25
2.7 Examples of a heteroclinic (left) and a homoclinic orbit (right) taken from Crommelin (2003). Black dots indicate the fixed points, arrows indicate the direction that the trajectory is moving in the phase space. Trajectories in a heteroclinic orbit will connect to the two fixed points and a homoclinic orbit will only connect to one fixed point. 27

2.8 Four regimes of the atmospheric circulation over the North-Atlantic. a) NAO positive, b) NAO negative, c) Scandinavian Blocking and d) Atlantic Ridge. Coloured contours are the 500hPa geopotential height anomaly (m), contours show the 500hPa geopotential height (m). Figure taken from van der Wiel et al. (2019). 30
2.9 Summary of the circulation at different locations in NAO/EA space. The horizontal axis of the grid of plots is the NAO and the vertical axis is the EA. Figure taken from Woollings et al., 2010. 32
2.10 The distribution in the winter 1979–2009 of daily eddy-driven jet latitudes, calculated from a daily zonal wind at 850 hPa at each longitude, in each JLI regime. The shaded value at any point represents the relative frequency with which the eddy-driven jet is found at that latitude, for that particular longitude in the (a) northern, (b) central, and (c) southern eddy-driven jet regime. Figure taken from Parfitt and Kwon (2020). 35
2.11 Time-height section of monthly mean zonal winds (m/s) measured at different equatorial stations. Shaded regions mark the westerlies. Figure taken from Kerzenmacher (2025). 39
2.12 Regression patterns of sea-level pressure anomalies (shading, unit: hPa) against the normalized early winter NAO index in the simultaneous early winter (a) and the subsequent January (b) for all neutral ENSO years. (c, d) and (e, f) Same as (a, b) but for the QBOe winters and the QBOw winters, respectively. Blue hatched regions indicate anomalies significant at the 90% confidence level. Figure taken from Cai et al., 2022. 40
2.13 Composite anomalies of the OLR (filled contours) and 850hPa wind (arrows) for Northern Hemisphere winter of the 8 phases of the Madden-Julian Oscillation. Figure take from Wheeler and Hendon, 2004. 43

3.1 Algorithm for identification of Eddy-Driven Jet Objects (EDJOs). In the map, the black star is the seed point and the black contour is the EDJO found from the seed point. 54
3.2 U_{850} (a,c) and WS_{850} (b,d) for two different days (rows). The dashed blue line denotes the JLI. The light blue dot is the position of $(\overline{\lambda}, \overline{\phi})$ the centre of mass. In b) and d), the magenta circles are the maxima at each meridian, and the magenta line is the result of a linear regression fitted to those maxima following Messori and Caballero (2015). The JAI in b) and d) is calculated from the end points of the magenta line, and the solid black line is the tilt given by α, which comes from the horizontal black line emanating from the centre of mass in a) and c). The values of the indices for the respective methods are given at the top right of each panel. 57
3.3 Time series of $\overline{\phi}$ (black crosses) and the JLI (solid blue line) for the boreal winter 2016/17. Pink triangles represent days with EDJOs. The black arrows indicate starting dates for the consecutive days shown in Figure 3.4. 58
3.4 Example days taken from the arrows shown in Figure 3.3 of the U_{850} field. The dashed blue lines denote the value of the JLI on each day. Solid black contours denote the EDJO. The light blue dots represent the centre of mass $(\overline{\lambda}, \overline{\phi})$ of the EDJO, with the longer black line denoting the major axis and the smaller the minor axis. 60
3.5 Same as Figure 3.4 but for the boreal winter of 1998/99 and red ticks mark the days where no EDJO is defined. 61
3.6 Same as Figure 3.4, but days are taken from the arrows in Figure 3.5. 62

3.7 Frequency per winter of large shifts ($\geq 10°$) in the EDJ latitude between consecutive days. The blue line shows the shifts for the JLI and the red for $\overline{\phi}$ for each winter in 1979-2020. The horizontal dashed lines show the average frequency in the colour of the respective measure of the EDJ latitude. The calculation of large shifts for $\overline{\phi}$ is only done on days where a single EDJO is defined. 63
3.8 Lagged autocorrelation functions for a) $\overline{\phi}$ (black) and the JLI (red); b) α (black) and the JAI (red) and c) U_{mean}, U_{max}, U_{mass} and JLI_{vel}. Solid lines represent the mean and shading two standard errors from the mean. 64
3.9 Distributions of the daily winter a) $\overline{\phi}$, b) JLI, c) $\overline{\phi}$ - JLI, d) α, e) JAI and f) α - JAI. In c) the histograms are coloured according the JLI regimes defined in the figure label, and in f) $\alpha - JAI$ is coloured according to the sign of the JAI. . . . 66
3.10 Distributions of $\overline{\phi}$ - JLI for each of the regimes of the JLI, with a) S, b) C and c) N. Each point is coloured by the value of α. 67
3.11 Composites of U_{850} for intervals of α where a) $0 \leq \alpha \leq 10$, b) $10 \leq \alpha < 20$, c) $20 \leq \alpha < 30$ and d) $\alpha \geq 30$. Horizontal dashed represent the mean value of $\overline{\phi}$ (black) and the JLI (blue) for each composite with there respective values given in the top right of each panel. 68
3.12 Distributions of the EDJO centre-of-mass $(\overline{\lambda}, \overline{\phi})$ for a) all EDJOs and b) the EDJO with the largest U_{mass}. The colours in a) indicate whether a given day is labelled with one (red) or two (blue) EDJOs. The black contours show the two-dimensional kernel density estimate of the distribution. . . . 69
3.13 Distributions of the EDJO centres of mass, partitioned into the S a), C b) and N c) regimes of the JLI. The colours of the points represent the days defined by one (red) or two (blue) EDJOs. The dashed horizontal lines define the cut-offs of the regimes of the JLI. 70
3.14 Scatter plots of $\overline{\phi}$ vs α a), $\overline{\phi}$ vs U_{mean} b) and α vs U_{mean} c). 71
3.15 Scatter plots of $\overline{\phi}$ vs U_{mass} a), α vs U_{mass} and U_{mean} vs U_{mass} 71

3.16 Mean Sea Level Pressure (MSLP) anomaly composites (in hPa) for different phases of the North Atlantic Oscillation (NAO) and East Atlantic pattern (EA). Panels (a) and (b) represent positive (NAO+) and negative (NAO-) phases of the NAO, while panels (c) and (d) represent positive (EA+) and negative (EA-) phases of the EA. 73
3.17 Gridpoint correlations (ρ) of linear regressions of $\overline{\phi}$ a), U_{mean} b), α c), $\overline{\lambda}$ d), U_{mass} e) against the MSLP for the winter (December-February). Stippling denotes statistically significant correlations at the 95% confidence level. The top right of each denotes the correlation that each metric has with the NAO and EA. 74
3.18 Same as Figure 3.18, but for the JLI a), JLI_{vel} b) and JAI c). 75
3.19 Scatter plots of the EA vs NAO for all winter days coloured by $\overline{\phi}$ a), JLI b), α c), JAI d) JLI_{vel} e), U_{mean} f) and U_{mass} g) for EDJOs of the largest mass. Note that e) and f) have different scales, and U_{mean} is bounded below by $U^*_{850} = 8\text{ms}^{-1}$. The values of mean μ and standard deviation σ are given for each quadrant in brackets, and the variance explained R^2. . 77
3.20 (a) Composite U^*_{850} field for winter days with two EDJOs. This represents 4.9% of DJF days. (b,c) Scatterplots of all winter daily EA vs NAO indices coloured by $\overline{\phi}$ for days with two EDJOs. Panel (b) shows the EDJO with the largest U_{mass}, and (c) shows the EDJO with the smaller U_{mass}. . . 78
3.21 Distributions of $\overline{\phi}$ a), α b) and c) the frequency of days with different numbers of EDJOs for a range of U^*_{850} values from $6\,\text{ms}^{-1}$ to $11\,\text{ms}^{-1}$, with colours following the legend in panel (a). 80
3.22 Distributions of $\overline{\phi}$ a), Area b) and the frequency of days with different numbers of EDJOs c) with the inclusion of the L^* and L^*_λ checks (blue), just L^*_λ (red) and just L^* (orange). . . 81

4.1 The number of EDJOs identified for the forecast period in GloSea5 and ERA5 a) and the perecentage difference in the occurrence of EDJOs b). 84

4.2 Distributions of $\overline{\phi}$ a), U_{mean} b), α c) and U_{mass} d) for GloSea5 (red) and ERA5 (black) for November-February between 1994-2016. Red shading represents two standard errors from the ensemble mean in GloSea5. The black vertical line is the mean for ERA5 and the red line shows the ensemble mean for GloSea5. Values of the mean and the standard deviation are given in the top left of each panel and the bias (with two standard errors) and RMSE in the top right. 87

4.3 Two-Dimensional distributions of $\overline{\phi}(^{\circ}\text{N})$ against $U_{\text{mean}}(ms^{-1})$ a), $\overline{\phi}(^{\circ}\text{N})$ against $\alpha(^{\circ})$ b), $\alpha(^{\circ})$ against $U_{\text{mean}}(ms^{-1})$ c), $\overline{\phi}(^{\circ}\text{N})$ against $U_{\text{mass}}(\text{m}^3\text{s}^{-1})$ d) and $\alpha(^{\circ})$ against $U_{\text{mass}}(\text{m}^3\text{s}^{-1})$ for all members of GloSea5 (red) and ERA5 (black) for NDJF between 1994-2016. 89

4.4 Averaged winter evolution of $\overline{\phi}(^{\circ}\text{N})$ a), $U_{\text{mean}}(ms^{-1})$ b), $\alpha(^{\circ})$ c) and $U_{\text{mass}}(\text{m}^3\text{s}^{-1})$ d) for ERA5 (black) and GloSea5 (red). The solid lines are the mean value and the shading represents two standard errors from the mean. 90

4.5 Autocorrelation functions of $\overline{\phi}$ a), U_{mean} b), α c) and U_{mass} d) for ERA5 (black) and GloSea5 (red). The solid read line represents the ensemble mean and the red shading represents the two standard errors from the mean at each lag. 92

4.6 Distributions of the NAO (a) and the EA (b) indices for GloSea5 (red) and ERA5 (black). 93

4.7 Distributions of the Pearson correlation coefficient per member of the daily values in GloSea5 between $\overline{\phi}$ and the NAO a), $\overline{\phi}$ and the EA pattern b), U_{mean} and the NAO c), U_{mean} and the EA pattern d), α and the NAO e), and α and the EA pattern f). The vertical black line is the correlation coefficient for ERA5. 95

4.8 Seasonal plots (NDJF) of $\overline{\phi}$ a), α b), U_{mean} c) and U_{mass} for ERA5 (black) and GloSea5 (red) where red shading is the 2σ model spread. The pearsonr correlation score (ρ) where the p-value for the correlation is given in brackets and the ratio of predictable components (RPC) is given at the top of each plot for p-values less than 0.05. 96

4.9 Same as Figure 4.5 but for the NAO a) and EA b) indices. . 98

5.1 Gridpoint Pearson correlation coefficients of the daily precipitation with $\overline{\phi}$ a), α b), U_{mean} c) and U_{mass} d). Stippling indicates a significant correlation at the 95% level. 104
5.2 Same as Figure 5.1 but for GloSea5. The correlations are calculated each member and then averaged to give the resultant pattern. 105
5.3 Difference in the variance explained (ΔR^2, expressed as a percentage) between ERA5 and GloSea5 for daily wintertime Precipitation for a) $\overline{\phi}$, b) α, c) U_{mean}, and d) U_{mass}. Positive values (red) indicate that the diagnostic explains more variance in ERA5 than in GloSea5, while negative values (blue) indicate greater explained variance in the opposite. 106
5.4 Same as Figure 5.1 but for T2m. 107
5.5 Same as Figure 5.2 but for T2m. 108
5.6 Same as Figure 5.3 but for T2m. Note magnitude of the colourbar has changed. 109
5.7 Anomalies of P (mm/day) in ERA5 for eight composites of the EDJO diagnostics, based on deviations from mean values: $\overline{\phi}$, U_{mass} and α. Each panel represents a different combination of values larger (+) or less than (-) the mean for these EDJ diagnostics, as indicated at the top of the Figure. Brown shades indicate drier-than-average conditions, and blue-green shades indicate wetter-than-average conditions. Red contours indicate the zonal wind at 850hPa. . . . 110
5.8 Same as Figure 5.7 but for GloSea5. 112
5.9 Same as Figure 5.7 but for 2m Temperature and zonal wind contours are in green. 114
5.10 Same as Figure 5.10 but for GloSea5. 115

5.11 Differences between GloSea5 and ERA5 for extreme 2m air temperature and precipitation events over Europe. The extremes are defined based on area-averaged values over the UK. Panels a) and c) show 2m air temperature differences for days above the 95th percentile and below the 5th percentile, respectively. Panels b) and d) show precipitation differences for the same percentiles. 117
5.12 Composite analysis of the evolution of T2m, $\overline{\phi}(^{\circ}\mathrm{N})$, $\alpha(^{\circ})$, and $U_{\mathrm{mass}}(\mathrm{m}^3\mathrm{s}^{-1})$ in ERA5 (black) and GloSea5 (red) during extreme temperature events. Panels a, c, e, and g represent composites around the 95th percentile (warm events), while panels b, d, f, and h represent composites around the 5th percentile (cold events). Solid lines represent the ensemble mean, while shaded regions indicate the 95% spread. The horizontal dashed lines represent the mean value for each dataset, and the vertical magenta line mark the onset of the extreme event. 119
5.13 Same as Figure 5.12 but for P and for wet and dry events. . 120

6.1 OLR anomaly in each phase of the MJO. Positive anomalies are regions of suppressed convection and negative are regions of enhanced convection. The value in the top left of each panel indicates the percentage of days in each phase. 129
6.2 Example RMM1 and RMM2 phase space plot for November - March of 2017/2018. The grey circle indicates the regions where A <1 and colours of each of the lines indicate the respective month. 130

6.3 Time series of the seasonal NINO3.4 index for NDJF for ERA5 between 1960 - 2020 in blue, ERA5 between 1993/4-2015/16 in black and GloSea5 between 1993/4-2015/16 in red. The solid red line is the Glosea5 ensemble mean and the shading represents the 2σ model spread. The black horizontal dashed lines mark the ± 0.5°C anomaly used to define El Niño and La Niña years. The Pearson correlation coefficient (ρ) with p-value (p) and the RPC score are given at the top. 133

6.4 Distributions of $\overline{\phi}$ (a and e), U_{mean} (b and f), U_{mass} (c and g) and α (d and h) for El Niño years (top row) and La Niña (bottom row). Both the full period (blue) and the forecast period (black dashed line) are shown, with the mean and standard deviation given in the top right of each panel. . . . 134

6.5 ERA5 Anomaly distributions of $\overline{\phi}$ (a and d), U_{mean} (b and e) and α (c and f) for November - December (top row) and January - February (bottom row) for El Niño years (pink) and La Niña years (green) for the hindcast period. The values in brackets in each panel are the mean and standard deviation coloured by the phases of ENSO. 135

6.6 Same as Figure 6.5 but for GloSea5. 136

6.7 Same as Figure 6.3 but for the QBO with units of ms^{-1}. The black horizontal dashed line represents the thresholds for defining the QBO west and QBO east years. 138

6.8 Same as Figure 6.5 but for the QBO. 139

6.9 Same as Figure 6.5 but for the QBO, with QBOe in the top row and QBOw in the bottom row. 140

6.10 Same as Figure 6.6 but for the QBO 140

6.11 Contingency tables for the postive NAO (green) and the negative NAO (pink) for each phase of the MJO. Circles mark the lags that are significantly different from the climatology at the 95% level. 142

6.12 Contingency tables for the occurrence of days where the standardised $\overline{\phi}$ exceeds 1 (green) or is less than -1 (pink), for days when the MJO is active at different lags. Points with solid circles indicate significantly different from climatology at the 95% level. 143
6.13 Same as Figure 6.12, but for U_{mean}. 144
6.14 Same as Figure 6.12, but for U_{mass}. 145
6.15 Same as Figure 6.12, but for α. 145

Chapter 1

Introduction

Jet streams are narrow bands of strong zonal winds, with speeds often exceeding 30-40 ms^{-1}, typically found in planetary atmospheres. On Earth, there are two primary jet streams: the subtropical jet stream (STJ) and the mid-latitude jet stream, also known as the eddy-driven jet stream (EDJ), as illustrated in Figure 1.1. The jet streams typically peak near the tropopause which lies at a height of around 10 to 15 km depending on the latitude. The STJ and the EDJ are geographically distinct; the STJ peaks near 30° latitude, while the EDJ peaks between 50° to 60° latitude in each hemisphere. These jets define the boundaries of two major atmospheric circulation cells, the Hadley and Ferrel cells (Figure 1.1).

The EDJ and STJ differ dynamically. The STJ forms near the edge of the poleward extent of the Hadley cell since air moving moves northward or southward in the upper branch, it is deflected to the east because of the Coriolis effect, creating westerly winds in the upper troposphere. Below the STJ, surface winds within the tropics are characterised by easterly trade winds. These easterlies arise as air moves from high-pressure regions near 30° latitude toward the low-pressure zone at the equator, and are deflected by the Coriolis effect, flowing from east to west.

Unlike the STJ, the EDJ is primarily driven by an interaction between the mean circulation and turbulent atmospheric eddies. These eddies are large-scale disturbances in the atmosphere, which arise due to the temperature

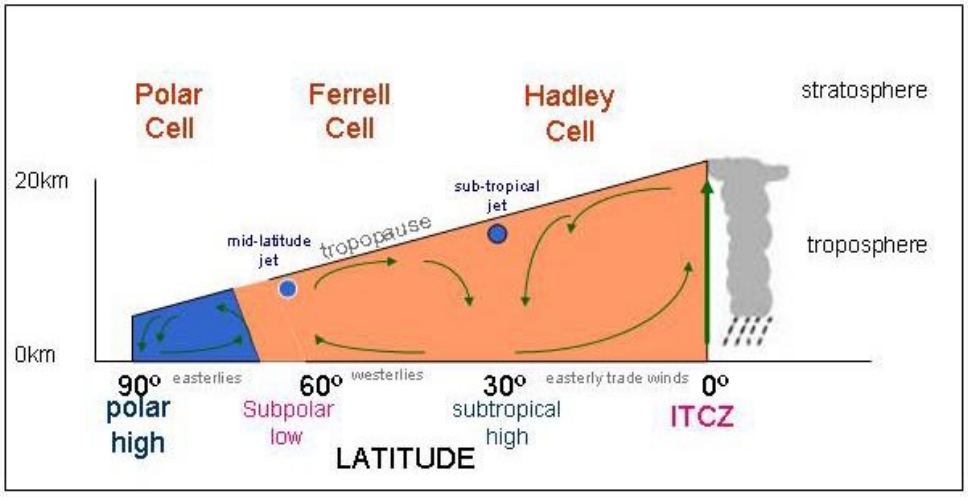

Figure 1.1: Schematic illustration of Earth's atmospheric circulation cells (Hadley, Ferrel, and Polar cells), displaying their vertical and latitudinal structure from the equator to the pole. Highlighted are key features including the Intertropical Convergence Zone (ITCZ), subtropical and mid-latitude (eddy-driven) jet streams, prevailing wind patterns (easterly trade winds, westerlies, and polar easterlies), and significant atmospheric pressure zones (subtropical highs, subpolar lows, and polar highs). The tropopause marks the boundary separating the troposphere from the stratosphere. Figure taken from Royal Meteorological Society (2025).

contrast between the cold air from the poles and the warm air of the tropics meeting in the mid-latitudes. As they meet, the atmosphere becomes unstable, forming baroclinic eddies transport heat and zonal momentum. At the surface, eastward winds are generated as a result of the propagation and breaking of eddies.

Jet streams show pronounced seasonal variability, as shown in Figure 1.2. During boreal winter (December-January-February, DJF; middle panel), the Northern Hemisphere jet streams intensify and shift equatorward due to increased meridional temperature gradients, making them particularly strong and prominent. Conversely, in boreal summer (June-July-August, JJA; bottom panel), the Northern Hemisphere jets weaken and shift poleward as temperature gradients lessen and thermal contrasts diminish. This seasonal shift is especially notable in the subtropical jet, which migrates significantly in response to changes in solar heating patterns.

In the Southern Hemisphere, the jet stream variability is similarly pronounced but occurs in reverse seasons compared to the Northern Hemisphere. The Southern Hemisphere jets reach peak intensity during austral winter (JJA), when the meridional temperature gradient is maximised, becoming particularly robust and nearly circumpolar due to less obstruction by continents and mountains. During austral summer, the jets weaken and shift slightly poleward.

Due to the asymmetries in the Northern Hemisphere created by mountain ranges, continents, and ocean temperatures, both the STJ and EDJ do not uniformly encircle the Earth, exhibiting substantial regional variability in their positions, strengths, and shapes. For example, the Pacific EDJ is stronger and more zonal, whereas the North Atlantic EDJ is weaker and more variable, significantly influenced by its smaller ocean basin and extensive surrounding orography.

Understanding these seasonal patterns and their variability is essential as they profoundly influence global weather systems. Changes in jet position and strength directly affect storm tracks, precipitation distributions, and temperature anomalies, affecting short-term weather events and long-term climatic conditions, including the occurrence and intensity of extreme

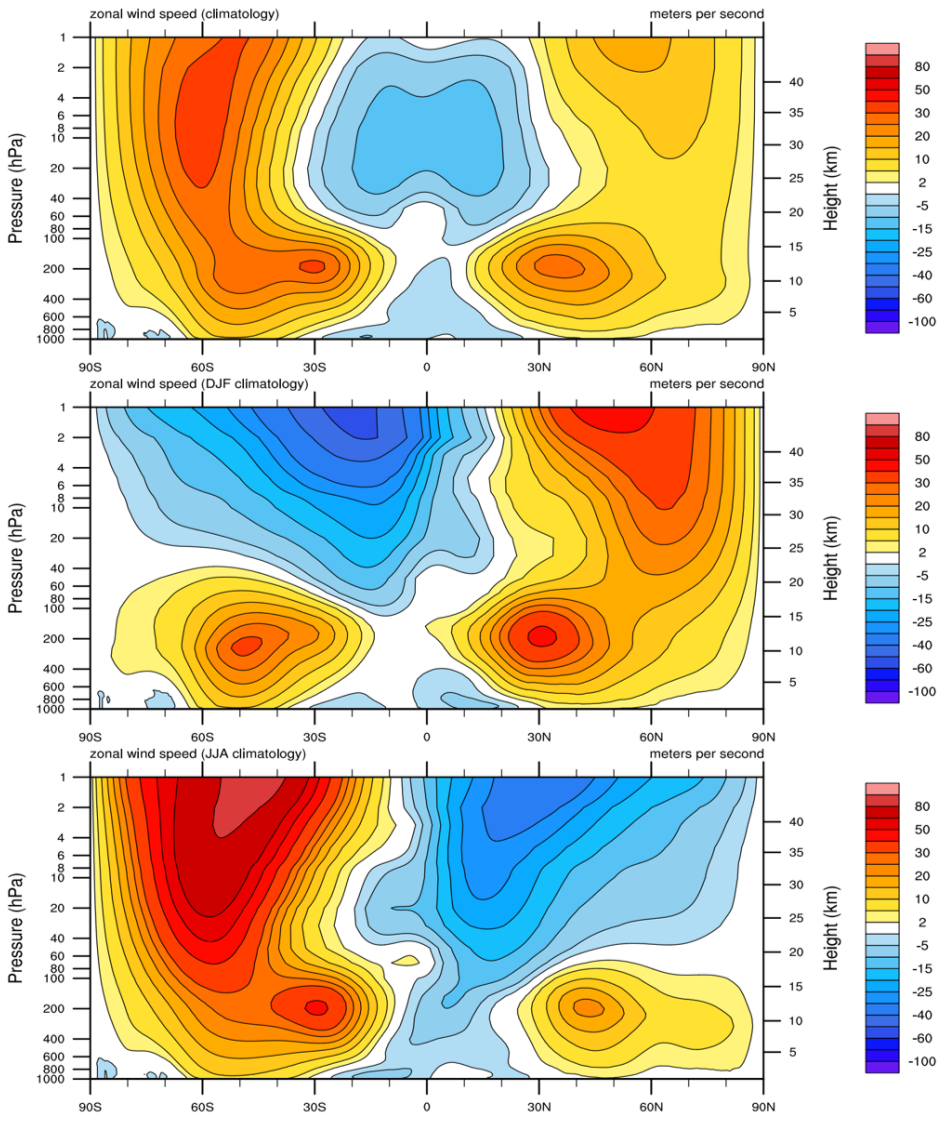

Figure 1.2: Climatological mean zonal wind speeds (ms^{-1}) from NCEP/NCAR reanalysis data, displayed as latitude-pressure cross-sections. The top panel shows the annual climatology, while the middle and bottom panels depict seasonal climatologies for December-January-February (DJF) and June-July-August (JJA), respectively. Positive (red-yellow) values indicate westerly winds, and negative (blue) values indicate easterly winds. Jet streams are clearly identifiable as regions of maximum westerly wind speeds located near the tropopause at approximately 200 hPa (approximately 10–15 km altitude). Figure taken from UC-Davis Climate Dynamics ATM 241 Course Materials (2025).

events such as droughts, floods, and heatwaves.

1.1 Focus

This thesis focuses on the EDJ within the North Atlantic sector and its impacts over Europe. An example of an event associated with a large deviation in the EDJ is the "Beast from the East" of February 2018, which brought widespread disruption to the UK due to plummeting temperatures and heavy snowfall. This event was characterised by the advection of cold air from Siberia, driven by a strong easterly flow associated with a high pressure system over Scandinavia. The resulting extreme weather conditions were linked to a large equatorward shift of the EDJ (Greening and Hodgson, 2019).

Hence, understanding and characterising different features (such as latitude and strength) of the EDJ is important for understanding what drives its variability. One of the most cited pieces of literature that covers this topic is by Woollings et al. (2010) who suggested that the EDJ displays preferred latitudinal positions or regime behaviour. The regimes are found using a method called the Jet Latitude Index (JLI), which calculates the latitude and the strength of the EDJ from a zonally averaged profile of low-level westerlies in the North Atlantic. The resulting distribution of daily winter latitudes is shown in Figure 1.3, which reveals three peaks representing preferred latitudinal positions of the EDJ, a northern (N), central (C) and southern (S) state, which is unique to the North Atlantic in the winter. The existence of regimes within the atmosphere is important, as it implies a state of persistence that has direct effects on weather patterns, extreme events, and predictability.

Many studies followed from Woollings et al. (2010), exploring the relationship of EDJ regimes with storm tracks (Novak et al., 2015), mid-latitude predictability (Frame et al., 2011; Hannachi et al., 2011), how each regime changes under different atmospheric drivers (Maycock et al., 2020; Oudar et al., 2020), its relationship to cluster on North Atlantic weather regimes (Madonna et al., 2017) and as a tool to assess the performance of climate models (Simpson et al., 2020). Rather than just exploring the latitude and

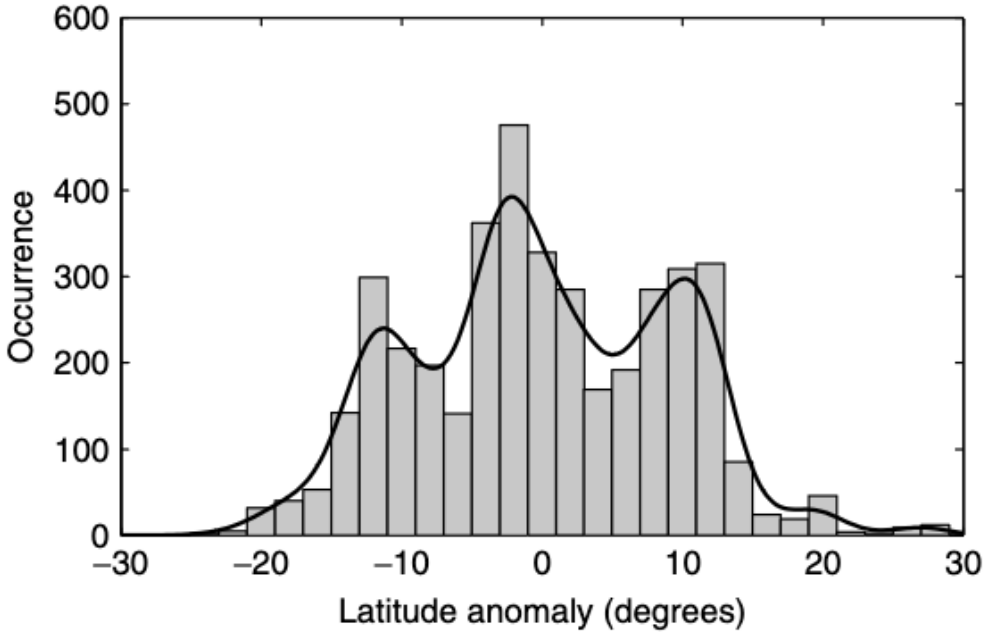

Figure 1.3: Eddy-Driven Jet regimes found by the Jet Latitude Index (JLI) of Woollings et al. (2010).

strength of the EDJ, further studies have explored other characteristics of the EDJ, such as its tilt (Barriopedro et al., 2022; Madonna et al., 2017; Messori and Caballero, 2015) and its waviness (Di Capua and Coumou, 2016).

However, some studies have questioned the interpretation of the JLI and its preferred states. The zonal averaging is specifically problematic in the North Atlantic because of the orography of Greenland. This was shown to heavily impact northly mode of the JLI as White et al. (2019) showed that it was not excursions of the EDJ, but instead mesoscale tip jets that occur off the coast of Greenland and cannot be separated within the zonal average. In addition to this, defining a single maximum in the zonal average is also problematic with profiles that are bimodal or uniform, where it becomes unclear where the maximum on these profiles is (Woollings and Blackburn, 2012).

Zonal averaging will also dampen the effects of localised phenomena, such as topography and land-sea contrasts, which can significantly influence the

position and strength of the EDJ (Brayshaw et al., 2009). This is especially true for the EDJ in the North Atlantic, which has a distinct tilt due to the generation of stationary wave forcing. Such localised effects are critical for understanding the full dynamics of the EDJ and its variability. Furthermore, the impact of blocking anticyclones or the presence of strong baroclinic zones can be obscured by zonal averaging. This limitation can result in the loss of important information on the EDJ response to various atmospheric conditions.

Hence, there is a need to consider alternative approaches to diagnosing the important features of the EDJ without zonal averaging. This new approach will then be compared to the literature using the JLI methodology to determine if there are substantial differences between the interpretations of the two.

1.2 Research Questions

This thesis attempts to answer the following questions:

1. Can a methodology be developed to diagnose the North Atlantic EDJ that accounts for its two-dimensional structure?
2. Does such a methodology suggest the presence of preferred states of the EDJ as is evident from the JLI?
3. What is the predictability of the EDJ on seasonal timescales in a state-of-the-art climate forecasting system?
4. How do atmospheric teleconnections impact the EDJ characteristics?

1.2.1 Structure of this thesis

The thesis is broken down as follows:

- Chapter 2 presents a review of the literature that provides the relevant background for the rest of the thesis.
- Chapter 3 describes the development of the new methodology for characterising EDJ in the North Atlantic. This chapter attempts to

answer questions 1-2 of the research questions.

- Chapter 4 explores the representation and predictability of the EDJ within a seasonal forecasting model.
- Chapter 5 examines relationships between the EDJ and surface climate variables.
- Chapter 6 explores both the seasonal and subseasonal drivers of variability in the North-Atlantic. Specifically, the El Niño Southern Oscillation, the Quasi-Biennial Oscillation, and the Madden-Julian Oscillation.

Chapter 2

Background

In this chapter, I will provide the necessary background and a review of the current literature to understand the later parts of this thesis. I will start with an overview of the general circulation, which will lead into the dynamics and mechanisms that give rise to the Eddy Driven Jet (EDJ). Following this will be an overview of our current understanding of the EDJ variability and teleconnections in the literature, with a focus on atmospheric regime behaviour associated with atmospheric drivers.

2.1 The General Circulation

The general circulation of the atmosphere is a complex system of large-scale motions that governs the distribution of weather patterns and climates throughout the world (Holton and Hakim, 2013). This circulation is driven by a combination of factors, including the unequal heating of Earth's surface, its rotation, and the interaction between air masses of different temperatures. The unequal heating of Earth's surface creates an energy imbalance between the equator and the poles. To try and correct this imbalance, the atmosphere responds by transporting heat from the tropics into the mid- and high latitude regions.

The atmospheric phenomena that contribute to this transport vary greatly on both temporal and spatial scales. To get an idea of this, Figure 2.1 shows the characteristic time and horizontal scales of various phenomena

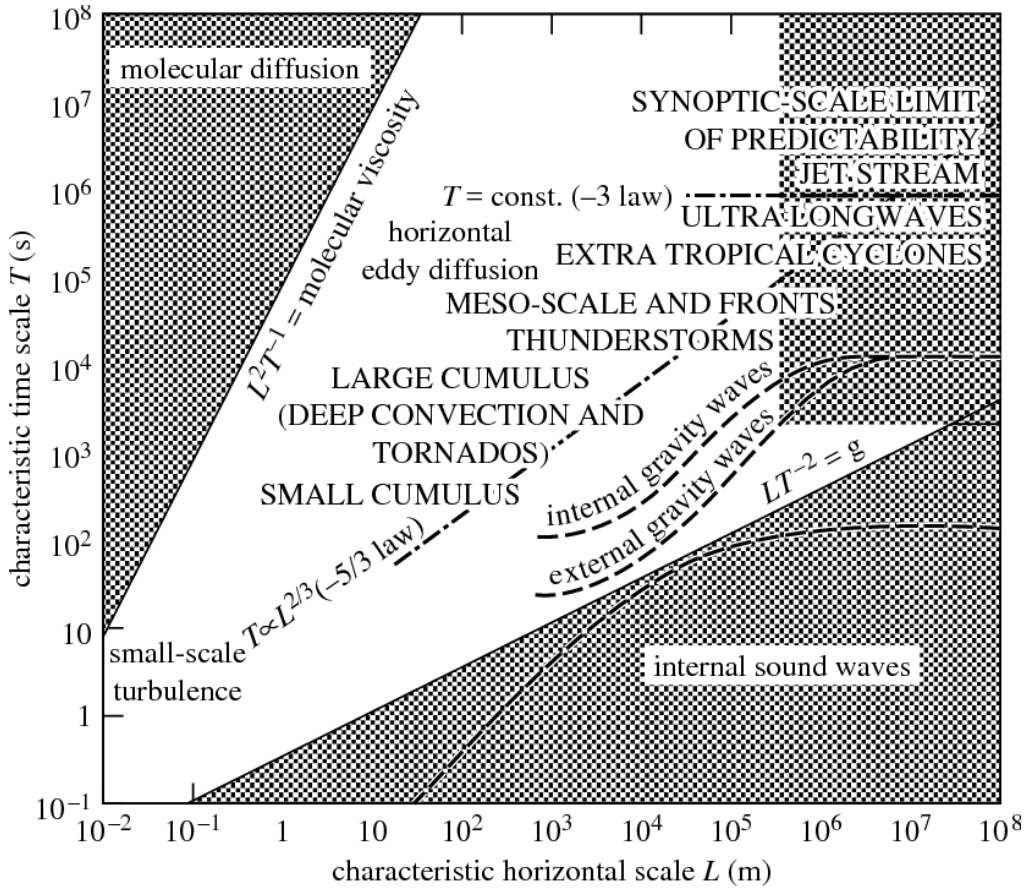

Figure 2.1: Time and spatial scales of different physical phenomena in the atmosphere Cullen and Brown, 2009.

related to the atmospheric circulation, ranging from small-scale turbulence all the way up to the jet streams, which have a characteristic length scales of 1000s of kilometres and temporal scales of weeks to months.

2.1.1 Jet Streams

Understanding the formation and dynamics of jet streams can be simplified by considering the concept of thermal wind balance. This involves a relationship between the geostrophic zonal wind (u_g) and temperature (T) described by the equation in log-pressure height coordinates (z) (Vallis, 2017)

$$f\frac{\partial u_g}{\partial z} = \frac{R}{H}\frac{\partial T}{\partial y}, \tag{2.1}$$

where f represents the Coriolis force, R stands for the gas constant of dry air, H is the depth of the troposphere (10^4km) and y corresponds to latitude. This equation is derived through a combination of geostrophic and hydrostatic balance and applies in the extratropics at low Rossby numbers.

If a surface of constant pressure tilts downward toward the north, it indicates a region of lower pressure. The pressure gradient force generates motion towards lower pressure, and the Coriolis effect deflects the flow to the right (in the Northern Hemisphere), resulting in a geostrophic wind blowing parallel to constant pressure surfaces with lower height to its left - causing a westerly wind. The role of temperature alters the thickness of the pressure layers as a result of the north-south temperature gradient between the pole and the equator. Hence, a constant pressure surface located farther aloft will slope progressively more strongly down towards the pole with height. This leads to an increase in both the pressure gradient and the strength of the geostrophic winds. This can be seen in Figure 2.2a, which shows zonally averaged zonal winds and temperature in the atmosphere, where the strongest westerly winds are found around the tropopause. This is the height of both the Subtropical Jet (STJ) and the EDJ in each hemisphere.

From a climatological perspective (Figure 2.2a), the winds of the Northern Hemisphere are typically weaker compared to those of the Southern Hemisphere, as seen in Figure 2.2b for the surface winds. This can be attributed to the fact that there is more land in the Northern Hemisphere, which weakens temperature gradients and subsequently diminishes wind strength due to increased stationary wave forcing. Based on equation 2.1.1, when the temperature gradient is stronger, the zonal winds are stronger. Hence, there is a seasonal cycle to the strength of the jet stream, with it weakest during the summer and strongest during the winter when the equator-to-pole temperature gradient is larger.

The STJ differs from the EDJ in that its main driving mechanism comes from angular momentum transport within the Hadley Cell and not from thermal wind balance. As air ascends near the equator and moves poleward

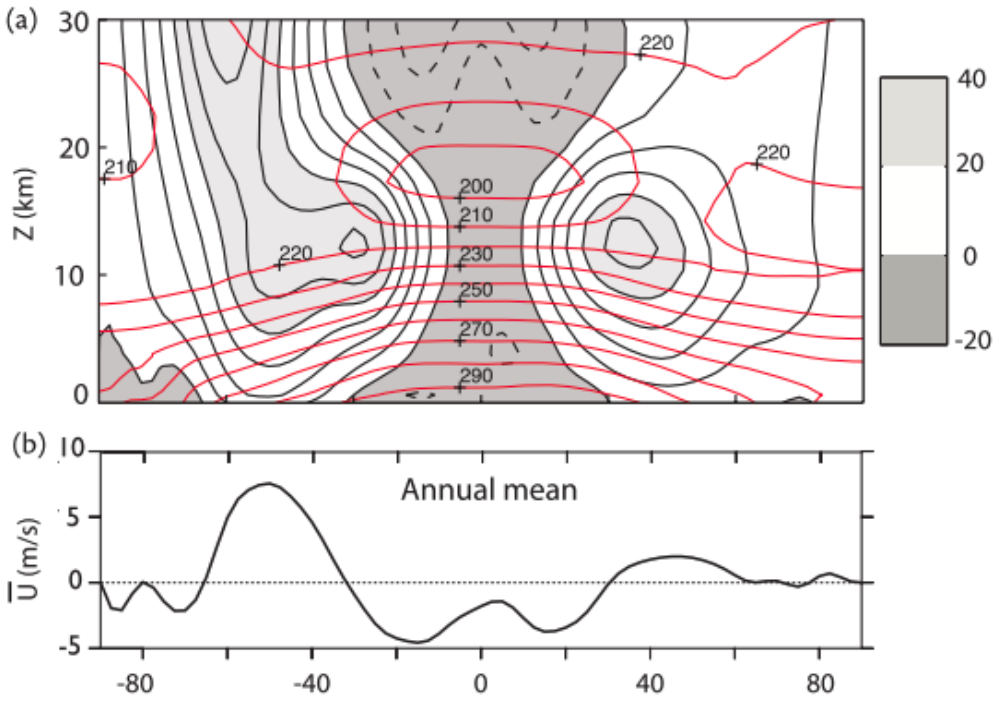

Figure 2.2: a) Annual mean zonally-averaged zonal wind (filled contours) and the zonally-averaged temperature (red contours). b) Annual mean zonally averaged zonal winds at the surface. Image taken from Figure 14.2 of Vallis, 2017.

in the upper branch of the Hadley Cell, it conserves angular momentum. Angular momentum (M) is defined as

$$M = (\Omega a \cos\theta + u)\, a \cos\theta, \tag{2.2}$$

where Ω is the angular velocity of the Earth, a is the radius, θ is the latitude and u is the zonal wind velocity. As air moves poleward in the upper branch of the Hadley cell, M is conserved, and since $\cos\theta$ decreases, u must increase. This results in a band of strong westerly winds near the poleward edge of the Hadley Cell, forming the STJ in the upper troposphere without the requirement of thermal wind balance.

There is a distinct spatial pattern in the distribution of easterly and westerly winds. Between 0-30°, easterlies prevail near the surface, while higher near the tropopause, there is a core of strong westerly winds on the poleward flank of the Hadley cell. This region is known as the tropics and the jet is known as the STJ. As we move towards higher latitudes entering the mid-latitudes between 30-60°, the westerlies extend to lower levels without the presence of easterlies. This area characterises the EDJ. Although Figure 2.2 may suggest only one jet stream, it is important to note that this represents a spatial and time average; therefore, they are not visibly distinct in this image but frequently are on individual days.

2.2 The Eddy-Driven Jet Stream

The formation and dynamics of the Eddy-Driven Jet (EDJ) are rooted in fundamental atmospheric processes, primarily involving the interaction of large-scale temperature gradients and rotational effects with atmospheric eddies. The EDJ is a key feature of the general circulation at mid-latitude and plays a key role in weather and climate patterns.

2.2.1 Eddies in the atmosphere

The development of an EDJ is intrinsically linked to the generation and evolution of eddies in the atmosphere. Eddies are disturbances in atmo-

spheric flow that range from small-scale turbulence in the boundary layer to large-scale extratropical cyclones and anticyclones. These structures facilitate the exchange of energy and momentum, which drives the variability and persistence of the EDJ. Eddy driven transport are generally defined as the deviation from the time and zonal averages. The northward heat transport by the atmosphere can be written as

$$\overline{vT} = \overline{v}\overline{T} + [\overline{v}][\overline{T}] + \overline{v'T'}, \tag{2.3}$$

where v is meridional wind, T is temperature, primes indicate a deviation from the time average, square brackets deviations from the zonal average and overbars indicate time averaging. Each term on the right-hand side is the contribution from the mean meridional circulation, stationary eddies, and transient eddies. Mid-latitude transient eddies are frequently visible on synoptic maps in the mid-latitudes and are one of the main drivers of local weather variability (Hartmann, 2016).

Transient midlatitude eddies are primarily generated through a type of hydrodynamic instability called a baroclinic instability. Baroclinic instability occurs in stratified fluids with a horizontal temperature gradient, such as the equator-to-pole temperature difference in Earth's atmosphere. This instability gives rise to eddies capable of extracting energy from the available potential energy of the background temperature gradient. These eddies play a crucial role in the poleward transport of heat and momentum that sustain the EDJ.

A classical framework for understanding baroclinic instability is the Eady model (Eady, 1949). The Eady model simplifies the atmosphere to a stratified rotating fluid with uniform vertical wind shear and rigid upper and lower boundaries. The model predicts the growth of perturbations with a characteristic westward tilt with height, as shown in Figure 2.3. This tilt is critical for the extraction of energy from the mean temperature gradient. As depicted in the figure, the streamlines exhibit a characteristic northeast-southwest tilt, which facilitates the northward transport of zonal momentum ($u'v' > 0$), while the westward phase shift of the temperature perturbations relative to the pressure perturbations leads to the northward

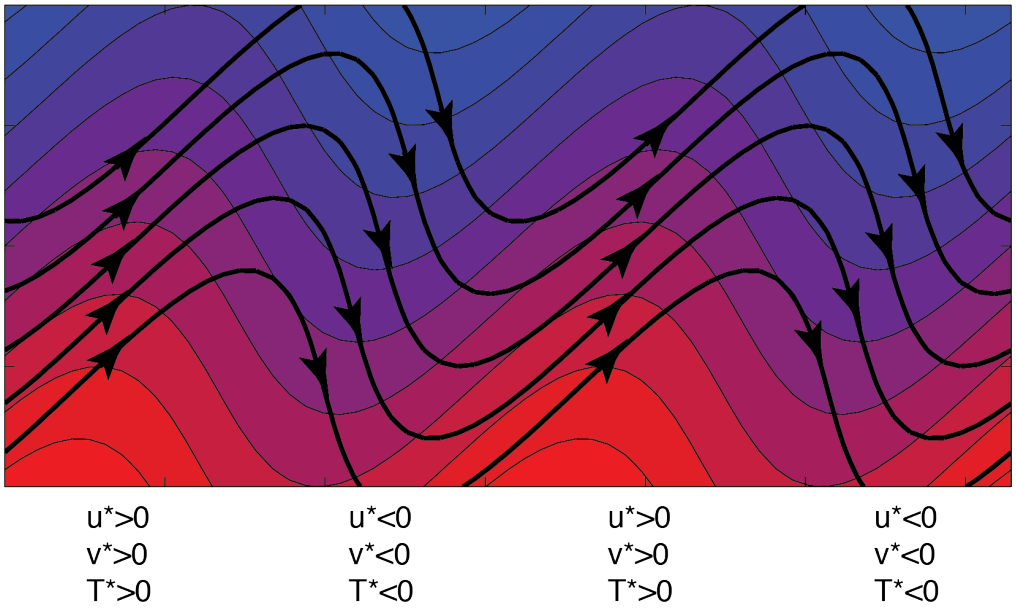

Figure 2.3: Schematic of the streamlines (black with arrows) and isotherms (coloured) associated with a large-scale atmospheric disturbance. Signs at the bottom are deviations of the zonal wind (u), meridional wind (v) and temperature (T) from there respective zonal average. Figure taken from Hartmann, 2016.

transport of heat ($v'T' > 0$).

The growth rate of the most unstable mode in the Eady model is expressed as:

$$\sigma = 0.31 \frac{f}{N} \frac{\partial u}{\partial z}, \tag{2.4}$$

where σ is the growth rate, f is the Coriolis parameter, N is the static stability, and $\frac{\partial \overline{u}}{\partial z}$ represents vertical wind shear. This equation demonstrates that the rate of eddy growth is proportional to the vertical wind shear and inversely proportional to the static stability. It also shows the link between eddies and the large-scale flow as a result of thermal wind balance

$$\sigma \propto -\frac{\partial T}{\partial y}, \tag{2.5}$$

hence the regions with strong meridional temperature gradients create higher vertical wind shear and an area that favours the growth of baroclinic eddies. An assumption within the Eady model is a constant vertical shear, which means that unstable eddies grow infinitely. Charney, 1947 improved upon this by including a damping of eddy growth to simulate a more realistic state, but the results are largely similar to the Eady model.

2.2.2 Wave-Mean Flow Interaction

The interaction between large-scale atmospheric motions and the zonally averaged circulation is crucial for understanding the variability and maintenance of key dynamical features, including the EDJ. In particular, eddies transport momentum and heat, redistributing angular momentum, and modifying the background flow. These eddies, substantially larger than the extratropical cyclones generated by barotropic instability, are known as Rossby waves, named after Carl-Gustaf Rossby (Rossby, 1939).

A way to understand the affect that eddies have on the mean flow is via the Eliassen-Palm (EP) flux vector (Holton and Hakim, 2013)

$$\mathbf{F} = (F_y, F_z) = \left(-\overline{u'v'}, \frac{f_0}{N}\overline{v'T'} \right), \tag{2.6}$$

where the meridional component (F_y) captures the eddy momentum flux and the vertical component (F_z) is proportional to the eddy heat flux. When $\mathbf{F}$ points upward, the heat flux term dominates, when $\mathbf{F}$ points meridionally, then the momentum flux dominates. As a diagnostic tool, $\mathbf{F}$ provides a direct measure of the contributions of both the heat and momentum fluxes in a system. To connect $\mathbf{F}$ to the evolution of heat and momentum in the atmosphere, consider the horizontal momentum and quasi-geostrophic thermodynamic equations,

$$\frac{\partial \overline{u}}{\partial t} - f_0\overline{v} = -\frac{\partial}{\partial y}\overline{u'v'} + \overline{r}, \tag{2.7}$$

$$\frac{\partial \overline{T}}{\partial t} + T_0\overline{w} = \frac{\partial}{\partial y}\overline{v'T'} + \overline{Q}, \tag{2.8}$$

$$f_0\frac{\partial \overline{u}}{\partial z} = -\frac{R}{H}\frac{\partial \overline{T}}{\partial y}. \tag{2.9}$$

The first equation describes how the acceleration of the zonal winds is influenced by the meridional circulation ($f_0\overline{v}$) and the divergence of the eddy momentum flux ($-\frac{\partial}{\partial y}\overline{u'v'}$) with the effects of friction ($\overline{r}$) included. The second equation describes the evolution of temperature in response to vertical motion ($T_0\overline{w}$), the horizontal divergence of eddy heat flux ($\frac{\partial}{\partial y}\overline{v'T'}$), and diabatic heating ($\overline{Q}$). The last equation is the thermal wind balance equation, which couples the two equations together. In steady state ($\frac{\partial}{\partial t} = 0$), each of the equations describes the balance between different dynamics and forces. For the zonal momentum equation, the distribution of momentum through the divergence of the eddy-momentum flux drives a meridional circulation. Then in the thermodynamic equation, heat transported by eddies acts to reduce the meridional temperature gradient, and vertical motion restores the temperature gradient through adiabatic cooling or heating. This in fact describes the circulation of Hadley and Ferrel cells, introduced at the beginning of the chapter, where the Hadley cell is driven predominantly through

the effects of diabatic heating and the Ferrel cell through the divergence of eddy-momentum fluxes.

The problem with these equations is that they treat the mean meridional circulation independently of the eddies. This leads to cancellations between the mean and eddy terms, which suggests that the two are related in some way. To address this, Andrews and McIntyre (1976) defined the transformed Eulerian mean equations (TEM). They introduced the residual circulation that accounts for the cancellation between the convergence of the eddy heat flux and adiabatic cooling. The meridional and vertical residual circulation are defined as

$$\overline{v}^* = \overline{v} - \frac{R}{H}\frac{\partial}{\partial z}\frac{\overline{v'T'}}{N^2} \tag{2.10}$$

$$\overline{w}^* = \overline{w} + \frac{R}{H}\frac{\partial}{\partial y}\frac{\overline{v'T'}}{N^2}. \tag{2.11}$$

The residual circulation captures part of the mean vertical velocity with a contribution to the adiabatic temperature change that is not cancelled out by the eddy heat flux divergence. Substituting the residual circulation equations into Eqn. 2.7 gives the TEM equations,

$$\frac{\partial \overline{u}}{\partial t} - f_0\overline{v}^* - \overline{r} = -\frac{\partial}{\partial y}(\overline{u'v'}) + \frac{\partial}{\partial z}(\frac{f_0}{N}\overline{v'T'}) = \nabla \cdot \mathbf{F} \tag{2.12}$$

$$\frac{\partial \overline{T}}{\partial t} + T_0\overline{w}^* = \overline{Q} \tag{2.13}$$

where now the zonal momentum equation contains all the eddy terms and the thermodynamic equation does not. In fact, the eddy terms are summarised as simply the divergence of the EP vector ($\nabla \cdot \mathbf{F}$). To visualise this process, Figure 2.4 shows the simulated evolution of a baroclinic lifecycle, where arrows are the EP vector and contours are the divergence of the EP vector.

At the start, the baroclinic growth is dominated by vertical eddy heat

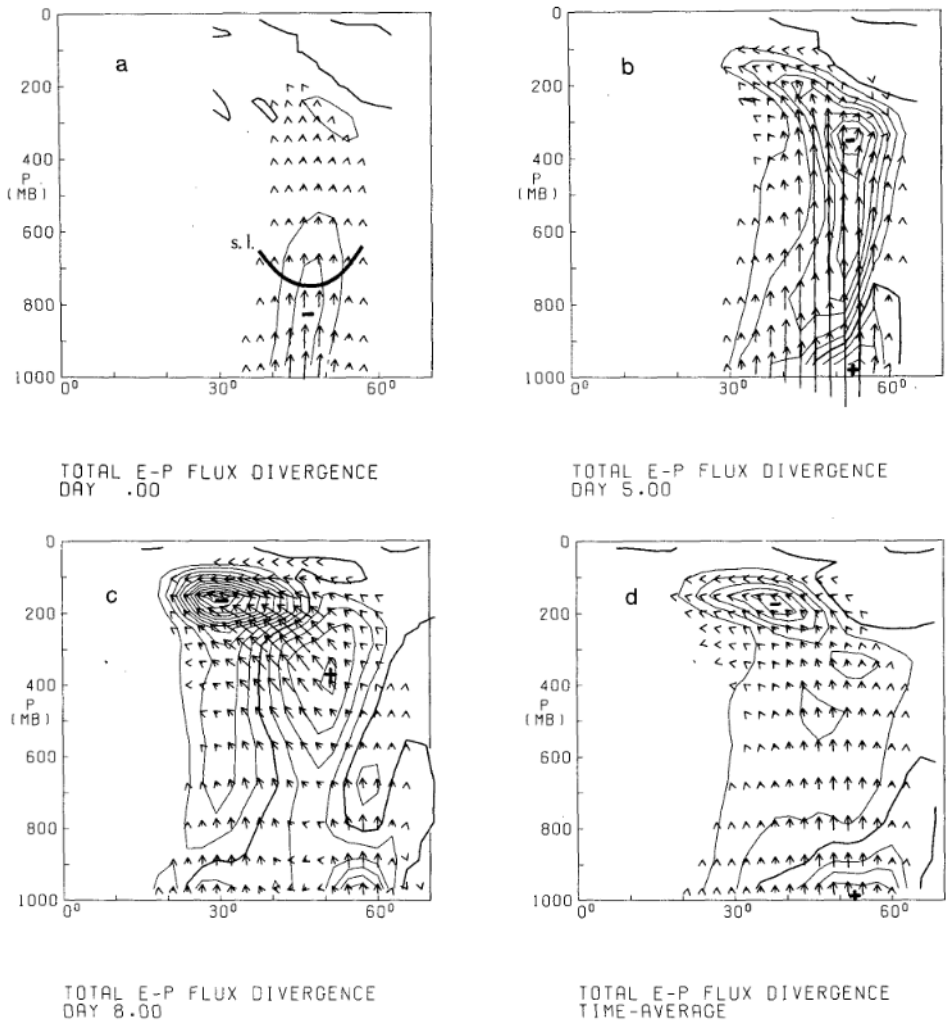

Figure 2.4: Eliassen-Palm vector (arrows) and divergence (contours) of a baroclinic lifecycle (a - c) and the time average (d) from Edmon et al., 1980. Height on the y-axis in mb and latitude in the x-axis.

fluxes and hence weakening of the flow near the surface. As growth continues, the vectors begin to turn meridionally as the disturbance reaches the upper troposphere, decelerating the flow ($\nabla \cdot \mathbf{F} < 0$) but accelerates the flow ($\nabla \cdot \mathbf{F} > 0$) near the surface. Toward the end of the lifecycle (Figure 2.4c), the accumulated eddy momentum flux convergence leads to a broad acceleration of the zonal wind throughout the mid-troposphere, giving rise to the vertically coherent structure of the EDJ. This highlights two fundamental roles of eddy forcing (1) deepening the jet structure by vertically redistributing momentum, and (2) providing a net acceleration of the mean zonal flow in the midlatitudes. The time-averaged state (Figure 2.4d) clearly shows this effect, with strengthened surface westerlies and a general weakening of the winds aloft near the subtropics due to the divergence of eddy momentum fluxes.

The connection between the transport of heat and momentum can be further simplified by considering the Quasi-Geostrophic Potential Vorticity (QGPV) equation,

$$\frac{Dq}{Dt} = X, \tag{2.14}$$

where $q = \zeta + \beta y + \frac{\partial}{\partial z}\left(\frac{f_0}{N^2}T\right)$ where ζ is the relative vorticity, f_0 is a constant Coriolis force at a fixed latitude, X is a form of dissipation and $\frac{D}{Dt}$ is the material derivative (Vallis, 2017). This equation is derived under the quasi-geostrophic assumption, which is where pressure gradients just balance the Coriolis force neglecting the effects of vertical advection and friction.

To link the TEM equations to the QGPV equations, we focus on the role of the EP flux in the meridional transport of potential vorticity (PV). To understand this link, we have to understand the evolution of the zonal mean PV, which is obtained from Eqn. 2.14

$$\frac{\partial \overline{q}}{\partial t} + \frac{\partial}{\partial y}\overline{v'q'} = \overline{X}. \tag{2.15}$$

This shows that the time evolution of zonal mean PV ($\overline{q}$) depends on the

meridional transport of the eddy PV fluxes ($\overline{v'q'}$) and any external sources or sinks ($\overline{X}$). In the TEM framework, the divergence of the EP flux ($\nabla \cdot \mathbf{F}$) is directly related to the eddy-induced forcing of the mean flow. Using some clever algebra (Vallis, 2017), it can be shown that

$$\nabla \cdot \mathbf{F} = \overline{v'q'} \tag{2.16}$$

and the TEM zonal momentum equation can be written as

$$\frac{\partial \overline{u}}{\partial t} - f_0 \overline{v}^* = \overline{v'q'} + \overline{r} \tag{2.17}$$

This relationship implies that the EP flux divergence quantifies the meridional transport of PV by eddies, linking the eddy fluxes of heat and momentum to changes in the mean flow. The divergence of EP flux drives changes in zonal mean circulation acting as a source or sink of PV, while the residual circulation ($\overline{v}^*$ and $\overline{w}^*$) adjusts to maintain the balance of thermal wind and the overall distribution of PV. Thus, the TEM framework and the EP flux provide a unified way to diagnose the impact of eddies on the large-scale mean flow through PV dynamics.

2.2.3 Rossby Wave Propagation

The previous section discussed the link between baroclinic eddies and momentum fluxes on a zonally averaged flow. Here, I explore sources of Rossby waves arising in a longitudinally varying flow, such as Earth's atmosphere, where orography and land-sea contrasts serve as wave sources. First, I outline how the conservation of barotropic vorticity leads to the generation of Rossby waves.

Rossby waves are generated primarily due to the latitudinal variation of the Coriolis parameter, known as the β-effect. This variation creates gradients in planetary vorticity that are crucial for transporting energy and momentum within mid-latitude regions, and significantly affecting large-scale atmospheric dynamics and zonally averaged flow. Considering Eqn. 2.14, we focus on a barotropic fluid without topography ($X = 0$), where

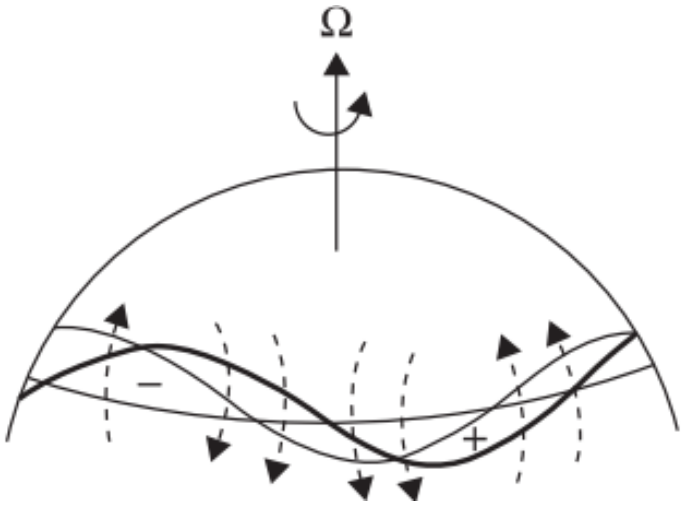

Figure 2.5: Perturbation vorticity field and induced velocity field (dashed arrows) for a meridionally displaced chain of fluid parcels. The heavy wavy line shows original perturbation position; the light line shows westward displacement of the pattern due to advection by the induced velocity. Figure taken from Holton and Hakim, 2013.

QGPV simplifies to $q = \zeta + f$, with $f = f_0 + \beta y$ and $\beta = \frac{\partial f}{\partial y}$.

The Rossby wave generation mechanism can be illustrated using a fluid ring encircling the Earth at a velocity u. Upon poleward displacement, the ring enters a region of higher planetary vorticity, requiring a reduction in zonal velocity to conserve angular momentum, thus inducing negative relative vorticity (ζ). Conversely, equatorward displacement requires increased zonal velocity and positive relative vorticity. These perturbations create an induced velocity field, visualised in Figure 2.5. Fundamentally, the formation of Rossby waves requires a gradient in PV (q) (Holton and Hakim, 2013).

Rossby wave propagation and momentum redistribution can be understood through their dispersion relation (Holton and Hakim, 2013)

$$\omega = \overline{u}k - \frac{\beta k}{k^2 + l^2}, \tag{2.18}$$

where ω is the wave frequency, and k and l represent zonal and meridional wave numbers, respectively. The phase speed ($c_p = \omega/k$) is always westward relative to the mean flow, since $\omega/k - \overline{u} = -\frac{\beta}{k^2+l^2} < 0$. However, the

group velocity travels in the opposite direction, with meridional and zonal components:

$$c_{gx} = \frac{\partial \omega}{\partial k} = \overline{u} - \beta \frac{l^2 - k^2}{(k^2 + l^2)^2} \tag{2.19}$$

$$c_{gy} = \frac{\partial \omega}{\partial l} = 2\beta \frac{kl}{(k^2 + l^2)^2}. \tag{2.20}$$

For a strong zonal flow toward the east ($\overline{u} >> \beta \frac{l^2-k^2}{(k^2+l^2)^2}$), the energy propagates downstream following the flow. The meridional component shows a tendency for Rossby waves to tilt depending on wave orientation. This distinction explains the downstream development and eastward propagation of mid-latitude weather systems. Rossby waves redistribute momentum away from their source region, causing downstream convergence (Vallis, 2017), which accelerates zonal wind and contributes to EDJ formation. The meridional momentum flux associated with quasi-linear Rossby waves is given by

$$\overline{u'v'} = -\frac{1}{2} Ckl, \tag{2.21}$$

where primes indicate deviations from the time mean and C defines a constant for wave amplitude. The sign of kl indicates the direction of the momentum flux: north of the source ($kl > 0$) results in the southward momentum flux, convergence, and strengthening of the EDJ; southward ($kl < 0$) results in divergence and weakening of the zonal flow.

As Rossby wave amplitudes increase, wave breaking occurs irreversibly distorting PV contours. The threshold for wave breaking is when the phase speed of the wave matches the speed of the zonal mean flow (Charney and Drazin, 1961). There are two primary types of wave breaking: 1) anticyclonic wave breaking (AWB) typically occurs poleward of the jet, associated with equatorward deflection of high PV air, resulting in negative PV anomalies poleward of the jet and strengthening of the EDJ; 2) Cyclonic wave breaking (CWB) typically occurs equatorward of the jet, involving poleward displacement of low PV air, causing momentum divergence and

weakening or equatorward shifting of the jet. Rossby wave-breaking events facilitate atmospheric blocking, significantly influencing regional climate variability. They redistribute momentum, transferring wave energy back to the mean flow and altering jet stream structure and position.

Strong mid-latitude jets with pronounced PV gradients act as waveguides, confining Rossby wave energy along jet cores, with wave amplitudes decreasing toward weaker jet flanks. Hoskins and Karoly, 1981 demonstrated that stationary Rossby waves from sources such as tropical convection and diabatic heating or orography, propagate along curved paths through the westerlies, explaining teleconnections such as El Niño Southern Oscillation impacts on the North Atlantic.

2.3 Regimes in the Atmosphere

2.3.1 Regimes in Simplified Models

One of the first and most well-known models of the atmosphere that demonstrates regimes was developed by Edward Lorenz (Lorenz, 1963). A model that describes convection in the atmosphere, with specific initial conditions, can produce cyclical patterns, such as the famous butterfly attractor, as shown in Figure 2.6. The trajectories of the Lorenz equations oscillate between two fixed points in phase space, illustrating the chaotic yet structured nature of the system. This concept highlights how regimes can be understood as recurring stable states that a system tends to revisit over time. Furthermore, systems can exhibit multiple regimes, as seen in the Lorenz model, where the butterfly attractor represents a two-regime system, with each regime centred around one of the fixed points.

Considering a model with increased complexity, Charney and DeVore (1979) and Charney and Straus (1980) use quasigeostrophic equations to model large-scale planetary motions in the atmosphere to determine how orography, thermal forcing, or both affect propagating planetary waves and atmospheric blocking. Charney and DeVore (1979) demonstrated that a barotropic atmosphere subjected to external forcing can exhibit multiple stable regimes, with implications for persistent features such as atmospheric

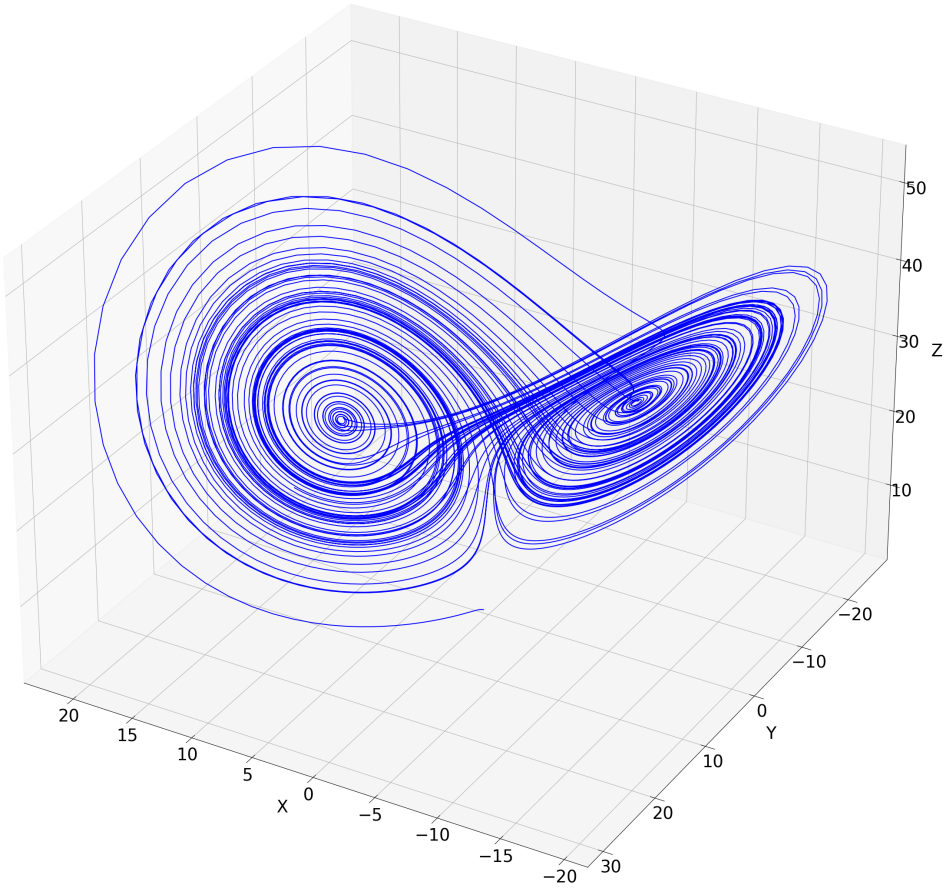

Figure 2.6: The Lorenz butterfly attractor, illustrating the trajectories oscillating between two fixed points in phase space.

blocking. Their study showed that blocking can be interpreted as its own regime, emphasising the role of nonlinear interactions between zonal flows and topography. Building on this foundation, Charney and Straus (1980) employed a more complex two-layer baroclinic model to explore the additional impact of vertical structure on atmospheric dynamics. Their findings revealed that baroclinic processes and orographic forcing could lead to switching between different regimes, explaining the variability of atmospheric blocking and the generation of propagating planetary waves.

Building upon this concept, Crommelin (2003) and Crommelin et al. (2004) extended the analysis by exploring how the atmosphere transitions between these equilibrium states. Crommelin (2003) applied deterministic dynamical systems theory to identify regime transitions as heteroclinic and homoclinic connections between equilibria (examples of these transitions are visualised in Figure 2.7), emphasising that these transitions are governed by structured dynamical pathways rather than purely stochastic processes. In addition, Crommelin et al. (2004) employed a similar barotropic model to Charney and DeVore (1979) to highlight the role of instabilities, including fold-Hopf bifurcations, in driving transitions between flow regimes. This work advances the understanding of atmospheric variability by providing additional evidence for the existence of multiple regimes in the atmosphere, as shown in Charney and DeVore (1979) and Charney and Straus (1980), but also details the dynamics that govern the evolution and persistence of blocking events.

Tung and Rosenthal (1985) used the same model as Charney and DeVore (1979) but did not truncate the equation, retaining the nonlinear terms, and found that the multiple regime structure is lost. They go on to show that the parameter regime used by Charney and DeVore (1979) which obtained multiple regimes is not physically realistic, with zonal jets reaching unrealistic speeds. Tung and Rosenthal (1987) further address the truncated baroclinic models used by Charney and Straus (1980), and similarly, with a nonlinear baroclinic equation, the multiple-regime behaviour is not observed. In this case, they do show that a single weather regime does exist, corresponding to a blocking regime with behaviour similar to the sixth equation of the truncated model of Charney and Straus (1980), but

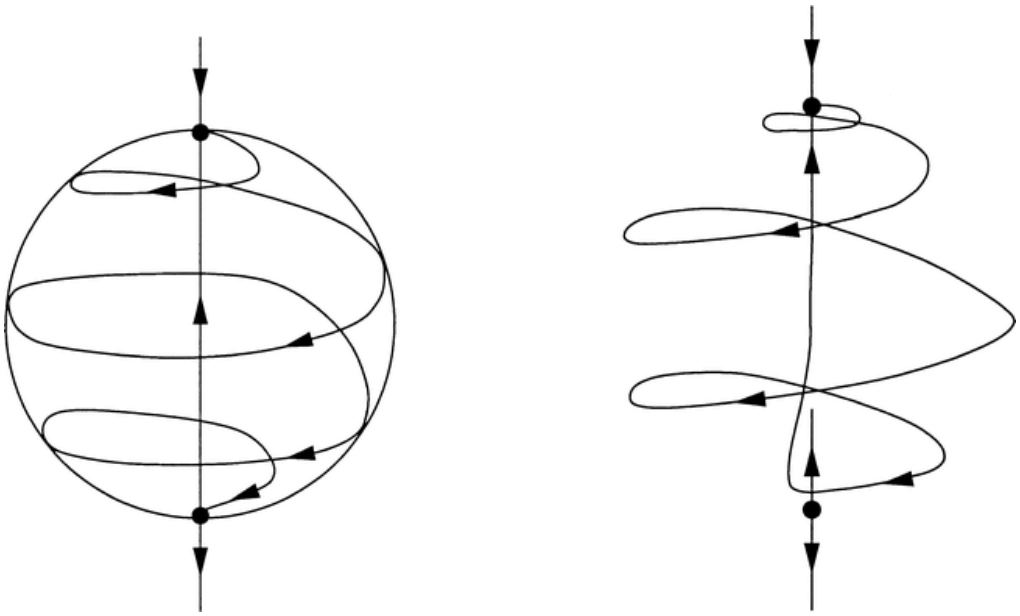

Figure 2.7: Examples of a heteroclinic (left) and a homoclinic orbit (right) taken from Crommelin (2003). Black dots indicate the fixed points, arrows indicate the direction that the trajectory is moving in the phase space. Trajectories in a heteroclinic orbit will connect to the two fixed points and a homoclinic orbit will only connect to one fixed point.

this was achieved using an unrealistic parameter range in the model. They are careful to stress that multiple regimes could be possible with physically sound choices of parameters, but determining this is difficult.

Together, these studies highlight a role for regimes in understanding atmospheric dynamics, offering insight into the mechanisms behind the persistence and variability of large-scale circulation features, albeit using simplified models of the atmosphere.

2.3.2 Regimes in Observations

Weather Regimes

The previous section presented evidence of atmospheric regimes, derived from simplified models of the atmosphere. The next question to address is whether such regimes, or any form of regime-like behaviour, can also be identified in the observed atmosphere. The observed atmosphere is characterised by complex, high-dimensional non-linear dynamics, which cannot

be fully described by a simple set of equations. Therefore, researchers typically rely on empirical methods, such as pattern matching and clustering techniques, to group similar days and identify recurring states. These approaches can help uncover potential regimes in observational data. Weather regimes are defined as recurrent and quasi-stationary states of large-scale atmospheric circulation that significantly influence weather patterns over extended periods (Vautard, 1990).

One of the primary methods for defining weather regimes involves the use of clustering techniques, typically being applied in the mid-latitudes to either the geopotential height or mean sea level pressure fields. This approach allows enables the identification of distinct patterns in the atmospheric circulation that recur over time. There exist multiple types of clustering, but a common approach for atmospheric research is k-means clustering. This partitions data into k clusters by minimising the within-cluster sum of squares (SS)

$$SS = \sum_{i=1}^{K} \sum_{x \in C_i} ||x - \mu_i||^2, \tag{2.22}$$

where C_i is the set of points in the cluster i, x is a data point, and μ_i is the centroid of the cluster i. The algorithm begins by randomly initialising k cluster centroids. Each data point is then assigned to the nearest centroid on the basis of a chosen distance metric, typically the Euclidean distance. After a data point is assigned, the centroids are updated by computing the mean position of the points in each cluster. These steps are repeated until the centroids stabilise or a convergence criterion is met. The result is k clusters where the data points in each cluster are more similar to each other than to those in other clusters. During winter, many studies of the North Atlantic system apply this with $k = 4$ a priori, producing a four-regime structure (Falkena et al., 2020; Madonna et al., 2017; van der Wiel et al., 2019).

Two of the most prominent large-scale modes of variability in the North Atlantic are the North Atlantic Oscillation (NAO) and the East Atlantic (EA) pattern (Wallace and Gutzler, 1981). The NAO is characterised by

a north–south dipole in sea level pressure between Iceland and the Azores Islands, influencing the strength and position of the westerly jet stream and storm tracks across the North Atlantic into Europe. In its positive phase (NAO+) the NAO is associated with a strengthened jet and enhanced zonal flow, often bringing wet and mild conditions to northern Europe, while its negative phase (NAO-) corresponds to a weakened jet and a more meridional flow pattern, often leading to colder and drier conditions in the same region (Dunstone et al., 2016; Mellado-Cano et al., 2019).

The EA pattern is structurally similar to the NAO but is shifted south-eastward. It represents a secondary mode of variability and modulates the weather in western and southern Europe (Thornton et al., 2023). Although less dominant than the NAO, the EA pattern can strongly influence regional temperature and precipitation anomalies, often acting in combination with the NAO to shape European winter weather.

Figure 2.8 shows the four regimes, two resemble the positive and negative phases of the NAO (Figures 2.8a and b) and the remaining patterns represent large-scale blocking patterns in the central Atlantic and over Scandinavia.

The NAO+ regime is characterised by a strong gradient in the geopotential height between the Azores high and the Icelandic low, leading to enhanced westerly winds and increased precipitation in Northern Europe and drier conditions in southern Europe (Charlton-Perez et al., 2018; Peings and Magnúsdóttir, 2014). The opposite phase is NAO-, which has a weakened gradient, resulting in westerly winds and the opposite conditions over northern and southern Europe (Peings and Magnúsdóttir, 2014). Scandinavian blocking has a distinct high-pressure system in Scandinavia, which disrupts the flow, leading to prolonged periods of cold and dry conditions (Madonna et al., 2017). Lastly, the Atlantic Ridge regime is associated with a large high pressure system in the central Atlantic Ocean, which can affect the frequency and intensity of weather systems entering Europe (Madonna et al., 2017). The Atlantic Ridge regime shows a strong similarity to the East Atlantic Pattern (EA), which will be used interchangeably.

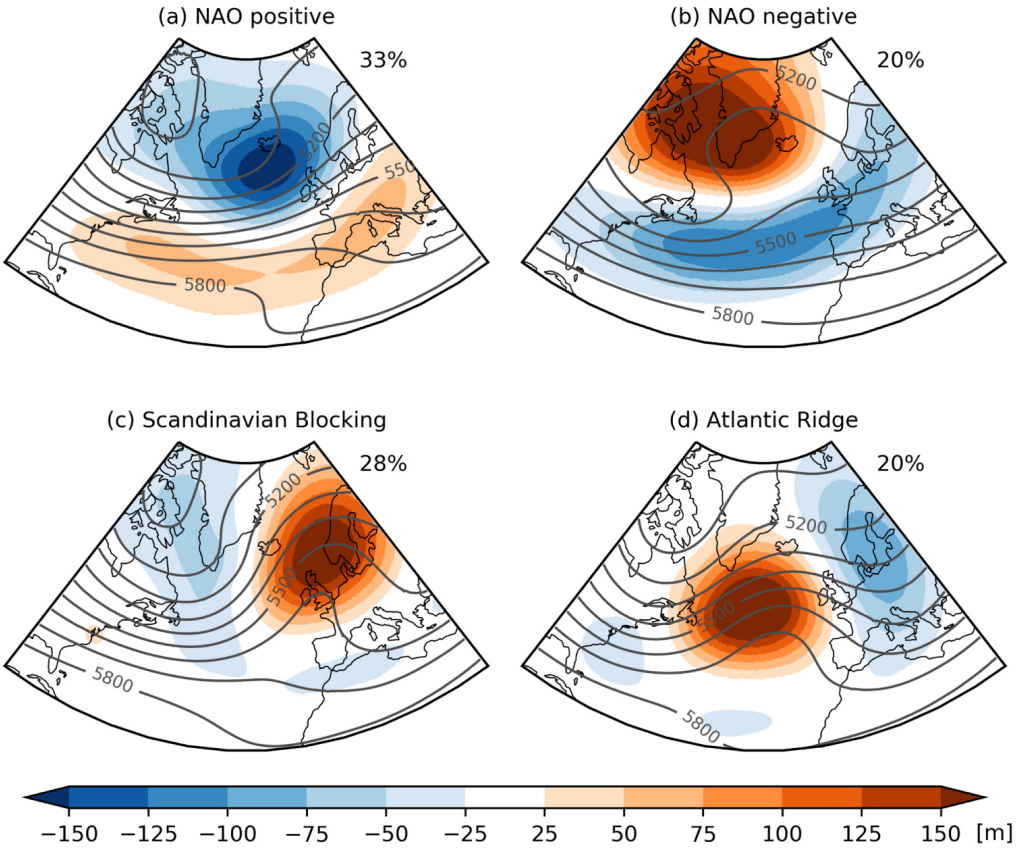

Figure 2.8: Four regimes of the atmospheric circulation over the North-Atlantic. a) NAO positive, b) NAO negative, c) Scandinavian Blocking and d) Atlantic Ridge. Coloured contours are the 500hPa geopotential height anomaly (m), contours show the 500hPa geopotential height (m). Figure taken from van der Wiel et al. (2019).

Jet Regimes

Moving away from statistical techniques such as clustering and Empirical Orthogonal Function (EOF) analysis, other methods directly analyse the flow in the mid-latitudes. For the EDJ, Woollings et al. (2010) developed a daily measure of the latitude and speed of the EDJ, called the Jet Latitude Index (JLI). This method applies a zonal sector average to the 850hPa zonal wind and defines the latitude and the speed as the location of the maximum. Applying this approach to all winter days results in a trimodal distribution of the latitude of the EDJ in the North Atlantic region, shown in Figure 1.3, suggesting three preferred regimes (southern, central and northern).

Further work examined the relationship between the three EDJ regimes and the characteristics of Rossby wave breaking and atmospheric blocking (Franzke et al., 2011). Describing the linear daily variability in the JLI requires combinations of the NAO and the EA pattern (Woollings et al., 2010). This is because individually the two patterns only capture one main aspect of the EDJ variability (Fyfe and Lorenz, 2005). The NAO is mainly associated with latitude changes in the EDJ and the EA with pulsing or the strength. This trimodal pattern is unique to the North Atlantic, with other ocean basins displaying either a unimodal or a bimodal distribution. Different combinations of NAO and EA are shown in Figure 2.9, where the solid contours are geopotential height anomalies and the filled contours are low-level zonal winds. This shows how different combinations of phases of the NAO and EA can lead to different impacts in Europe as a result of differences in the EDJ.

The three-regime structure of the JLI is explored further in Hannachi et al. (2011), where it is shown that the preferred transitions between each of the regimes are south to central, north to south, and central to north, which is in order of increasing probability. The north-to-south and central-to-north transitions are further shown to be linked to cyclonic and anticyclonic wave breaking events, linking to previous studies of wave breaking to the positive and negative phases of NAO (Strong and Magnusdottir, 2008; Woollings et al., 2008).

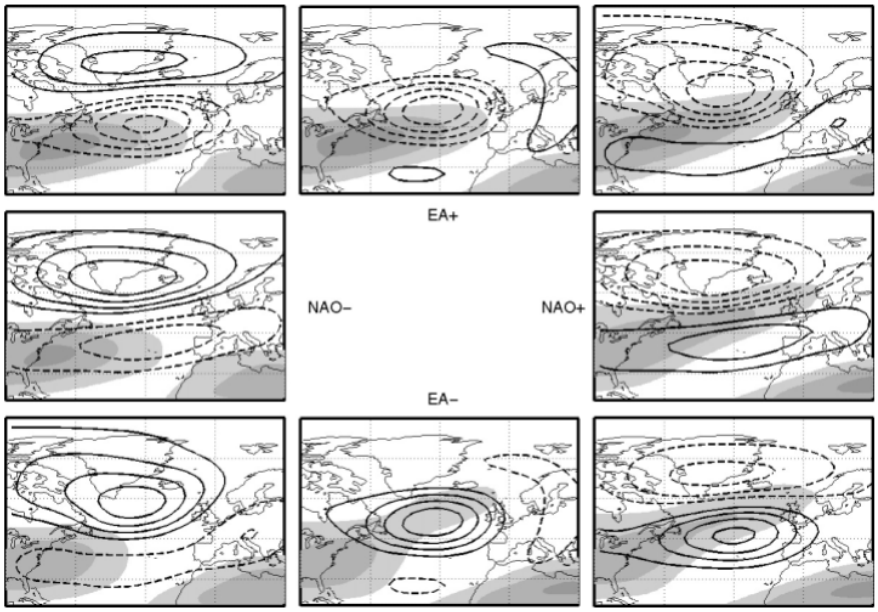

Figure 2.9: Summary of the circulation at different locations in NAO/EA space. The horizontal axis of the grid of plots is the NAO and the vertical axis is the EA. Figure taken from Woollings et al., 2010.

The EDJ in the North Atlantic also displays other defining features in addition to its latitude and strength; there is a distinctive northeast-southwest tilt to the EDJ that is lost in the zonal average. Other methods employ this extra detail in characterising the EDJ (Barriopedro et al., 2022; Messori and Caballero, 2015), and find connections to wave breaking and differences in surface impacts over Europe when tilt is included.

EDJ regimes and Weather Regimes

With two sets of regime structure defined over the North Atlantic region, a new question emerges of how the two are related to each other? Studies have looked at this in different ways. Madonna et al. (2017) applied k-means clustering to the first six EOFs of low-pass-filtered 850hPa zonal winds and looked at differences between the choice of three, four of five clusters. They find that choosing four clusters, matching the number of weather regimes, results in the three latitudinal regimes of the JLI and a fourth they call a mixed cluster, due to the pattern displaying regions of strong north and south winds. The case for five clusters results in a new

tilted regime, characteristic of the EDJ in the North Atlantic during winter. Interestingly, for three clusters only the northern and central latitude regimes of the JLI are recovered, and the mixed regime is found instead.

The link between the two regime frameworks is further investigated in Dorrington and Strommen (2020), where it is argued that the speed of the EDJ is the source of problems in the identification of the regimes. Hence, they remove variability associated with the EDJ speed from the 500hPa geopotential height field and apply k-means clustering with three and five clusters, which show similarities with the results of Madonna et al. (2017). The choice of three or five clusters is justified through the use of the Bayesian Information Criteria (BIC), whose minima determine the optimal choice of clusters for the given data and a stationarity metric as a measure of persistence. The results they show for the five clusters show many similarities to the five clusters of Madonna et al. (2017), where the mixed regime is called the split jet regime instead.

2.3.3 Correct number of regimes?

With k-means clustering, there is a question on what is the correct choice for the number of regimes. This was addressed in Dorrington and Strommen (2020), who find that the best representation was five regimes, based on the combination of two different metrics. However, other studies use the fact that the three regimes of the JLI as reason enough to say that clustering with three regimes is optimal (Frame et al., 2011).

This is not an easy question to answer, as discussed by Christiansen (2007), who tested two different clustering algorithms with idealised and observed datasets. It is shown that for the surrogate data, one can to obtain "regimes" from the data when the data themselves are unimodal and do not display any inherent regime structure. Furthermore, when testing the observed geopotential height data, it is found that there are significant sensitivities to the number of regimes depending on the period and the choice of algorithm. This, of course, calls into question the legitimacy of the four weather regime structures discussed previously. There are also potential problems with the impact of preprocessing the data prior to clustering.

As stated above, many studies apply clustering on EOFs of the 500hPa geopotential height to focus on low-frequency variability. However, doing this leads to increased persistence and therefore changes in the occurrence rates of the regimes, as shown by Falkena et al. (2020). They actually suggest a constraint to the persistence in the clustering and to use unfiltered data, which in turn results in the optimal number of regimes now being six, with opposing phases for the AR and BL regimes.

However, in addition to the sensitivities of the methodology, the other influence on regimes comes from the features of the region they are defined over. For example, in the definition of the JLI, the zonal averaging step masks the characteristic tilt of the North Atlantic EDJ. This is shown to be problematic by White et al. (2019), who showed in a set of numerical experiments that Greenland tip jets populate the northern regime of the JLI and are not associated with the EDJ. This calls into question the regime structure of the JLI and whether it is sensible to define a northern EDJ. The influence of Greenland on the definition of the JLI in Figure 2.10, which shows the occurrences of JLI events at each longitude split by the JLI regimes, is taken from Parfitt and Kwon (2020).

Here, it is clear the number of events that occur on the tip of Greenland occurring in the northern regime, while the southern and central regimes show coherent event occurrences forming bands of zonal winds associated with the EDJ. The methods used to define the EDJ also vary, with some including a latitudinal weighting of the wind field before calculating the latitude, some including the vertical structure and calculating jet cores, and more complex methods that calculate horizontal shear on PV surfaces (Keel et al., 2024). All of these methods show differences in how to define a distinct latitude for the EDJ, but nearly all of them do not show trimodality in the position of the EDJ. The question is then whether it is sensible to define these as regimes or if the regime structure exists at all.

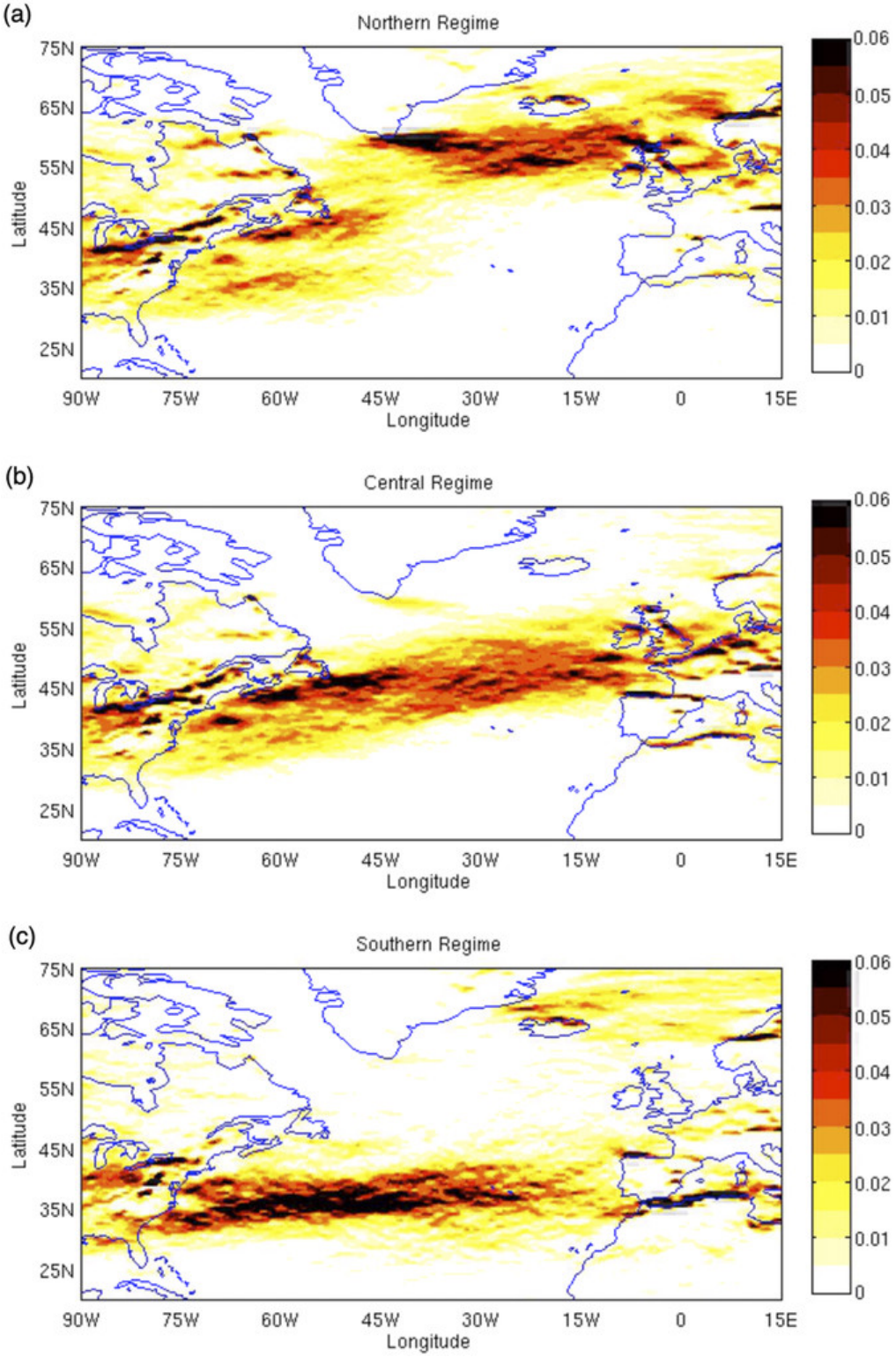

Figure 2.10: The distribution in the winter 1979–2009 of daily eddy-driven jet latitudes, calculated from a daily zonal wind at 850 hPa at each longitude, in each JLI regime. The shaded value at any point represents the relative frequency with which the eddy-driven jet is found at that latitude, for that particular longitude in the (a) northern, (b) central, and (c) southern eddy-driven jet regime. Figure taken from Parfitt and Kwon (2020).

2.4 Remote Drivers of North Atlantic Variability

Changes in the NAO and EA have been shown to be the result of different types of Rossby wave breaking (Woollings et al., 2008). As was shown in Woollings et al. (2010), different combinations of NAO and EA lead to different latitude and strength of the EDJ. The phenomena that generate these waves are called teleconnections because of the non-local sources of Rossby waves that influence weather and climate in different regions. This thesis will address three such teleconnections in the atmosphere: the El Niño Southern Oscillation (ENSO), the Quasi-Biennial Oscillation (QBO), and the Madden-Julian Oscillation (MJO). Each of these has stronger impacts on variability at different time scales, with ENSO and QBO being seasonal drivers, and the MJO a subseasonal driver.

El Niño Southern Oscillation

ENSO is the dominant mode of interannual tropical variability in the climate that influences global climate through remote teleconnections. It is associated with see-saw pattern of sea surface temperature anomalies in the equatorial Pacific, with warm anomalies defined as the El Niño phase and La Niña the cold phase. Tropical convection associated with ENSO creates Rossby wave trains that can propagate through the troposphere via the Carribean Sea to the North Atlantic, or they can travel vertically and enter the stratosphere (Hardiman et al., 2019). The tropospheric pathway is associated with both North America and Europe, but the stratospheric pathway is predominantly associated with extreme events in the North Atlantic and Europe (Butler et al., 2014).

The stratospheric link to the North Atlantic is through changes in the stratospheric polar vortex that can occur because of the phase of ENSO. The polar vortex is a band of strong westerly winds in the stratosphere, whose strength has a downward influence on surface weather in the North-Atlantic. This is shown in Baldwin et al. (2001), where a stronger polar vortex is typically associated with a stronger jet stream and a positive NAO and a weaker polar vortex leading to a negative NAO and a weaker

jet stream.

With regard to the jet regimes, Maycock et al. (2020) show that changes in the stratosphere directly affect the JLI. Using model experiments and observations of sudden stratospheric warmings (a weakening of the stratospheric polar vortex), it is shown that there is an increased occurrence of the southern regime of the JLI and a decrease in the north regime. This follows the response of an increased occurrence of NAO- events, where there is an equatorward shift in the EDJ. Changes in the occurrence of these patterns and/or their duration will therefore lead to extended durations of particular types of weather in the Euro-Atlantic region. One source of variability comes from the stratosphere after a sudden stratospheric warming event, where Ayarzagüena et al. (2018) showed that the occurrence of the NAO- regime significantly increased the leading changes in precipitation patterns in southern Europe. Similarly, Charlton-Perez et al. (2018) found that NAO- is the most sensitive to the stratospheric state, occurring on 33% days following weak vortex conditions but only on 5% days after strong vortex conditions. An opposite and slightly weaker sensitivity is found for the NAO+ and AR regimes. For NAO regimes, stratospheric conditions change both the probability of remaining in each regime and the probability of transitioning to that regime from others.

There are also distinct timings in when the ENSO signal impacts the North-Atlantic. Ayarzagüena et al., 2018 showed for El Niño years during the early winter (November-December, typically) the North Atlantic circulation is characterised by a positive NAO pattern, which switches to a negative NAO pattern in the late winter (January-February). For La Niña years, the response was largely opposite to El Niño years, where an EA pattern dominated in the early winter and a positive NAO in the late winter.

O'Reilly et al., 2024 showed that the early winter response is stronger than in late winter, with El Niño suppressing northern jet occurrences and La Niña enhancing them. This matches what is seen in Ayarzagüena et al., 2018, with the NAO. In addition to this O'Reilly et al., 2024 shows that in early winter, the impact of ENSO is mediated by the North Pacific storm track, where a stronger Pacific storm track leads to more frequent equatorward jet shifts in the North Atlantic. In late winter, ENSO mainly

influences the north Atlantic through the breaking of cyclonic waves and the propagation of downstream energy from the North Pacific.

Quasi-Biennial Oscillation

The Quasi-Biennial Oscillation (QBO) is the main mode of interannual variability in the equatorial stratosphere (Pahlavan et al., 2021). It consists of an alternating easterly and westerly wind anomalies with a period of around 28 months. These wind anomalies form in the upper stratosphere (5-10hPa) and propagate downward towards the lower stratosphere before dissipating (Baldwin et al., 2001).

The QBO is driven by a combination of vertically propagating waves from the tropics, which deposit their momentum in the stratosphere creating the alternating direction of the zonal winds. Figure 2.11 shows the descending winds that produce the characteristic time-height pattern in the zonal winds.

Although the QBO is confined to the equatorial stratosphere, it has influence on the dynamics in the extratropics and in the North Atlantic. This is due to the way QBO modulates the winter stratospheric polar vortex, which leads to changes in the signals on the surface in the North Atlantic region. This mechanism is known as the Holton–Tan effect (Holton and Tan, 1980), which describes the observed relationship between the phase of the Quasi-Biennial Oscillation (QBO) in the tropical stratosphere and the strength of the stratospheric polar vortex in the Northern Hemisphere. In particular, during the easterly phase of the QBO (QBOe), planetary waves can propagate more effectively into the stratosphere and decelerate the polar vortex, making it more disturbed and weaker. In contrast, during the westerly phase (QBOw), the stratospheric wind structure tends to inhibit wave propagation, favouring a stronger and more stable polar vortex. This stratosphere–troposphere coupling can modulate surface weather patterns, particularly in the extratropics.

The QBOe phase favours upward propagation of waves into the stratosphere (Baldwin et al., 2001), leading to a weakening of the polar vortex due to an increase in breaking planetary scale Rossby waves. The QBOw phase

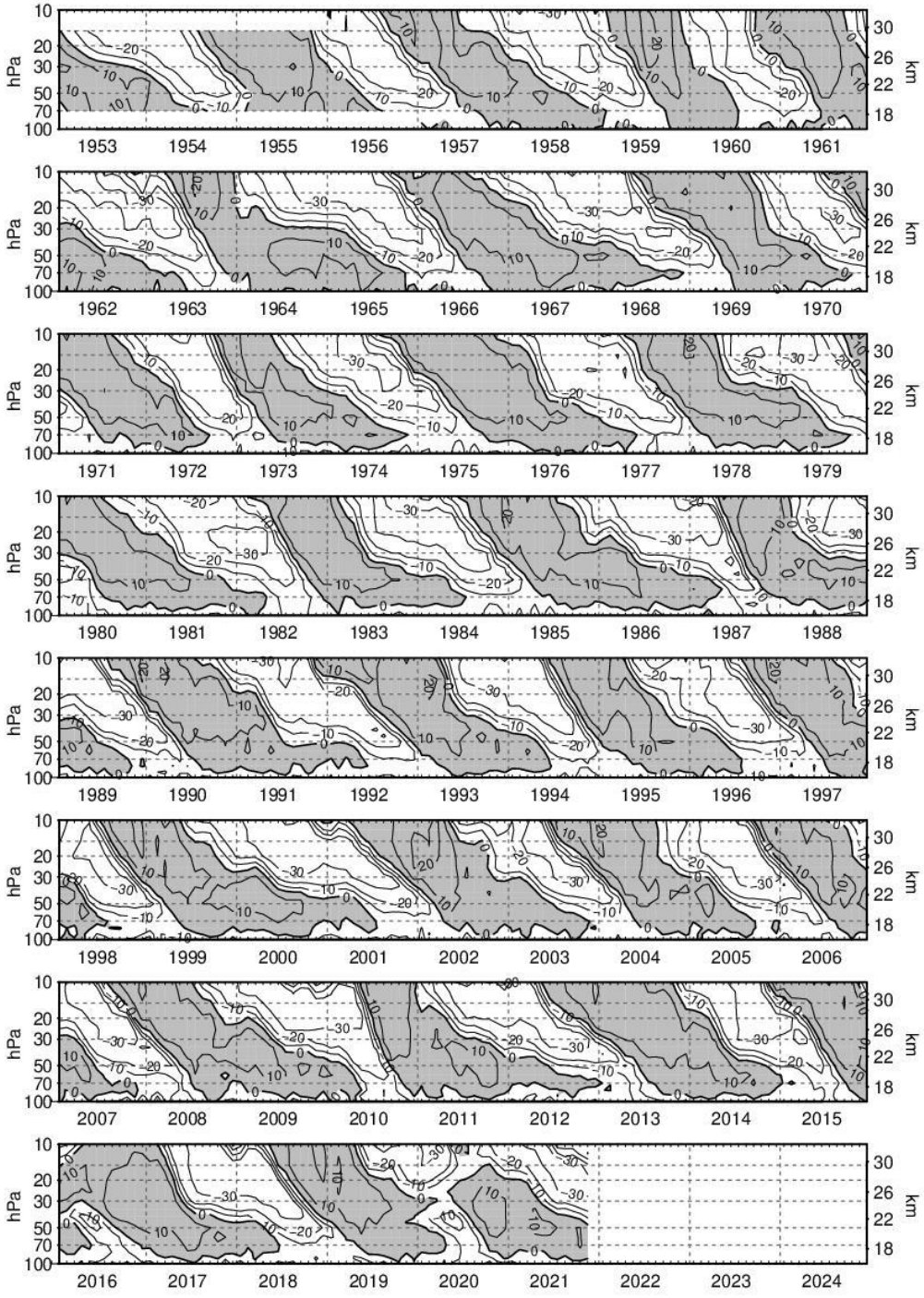

Figure 2.11: Time-height section of monthly mean zonal winds (m/s) measured at different equatorial stations. Shaded regions mark the westerlies. Figure taken from Kerzenmacher (2025).

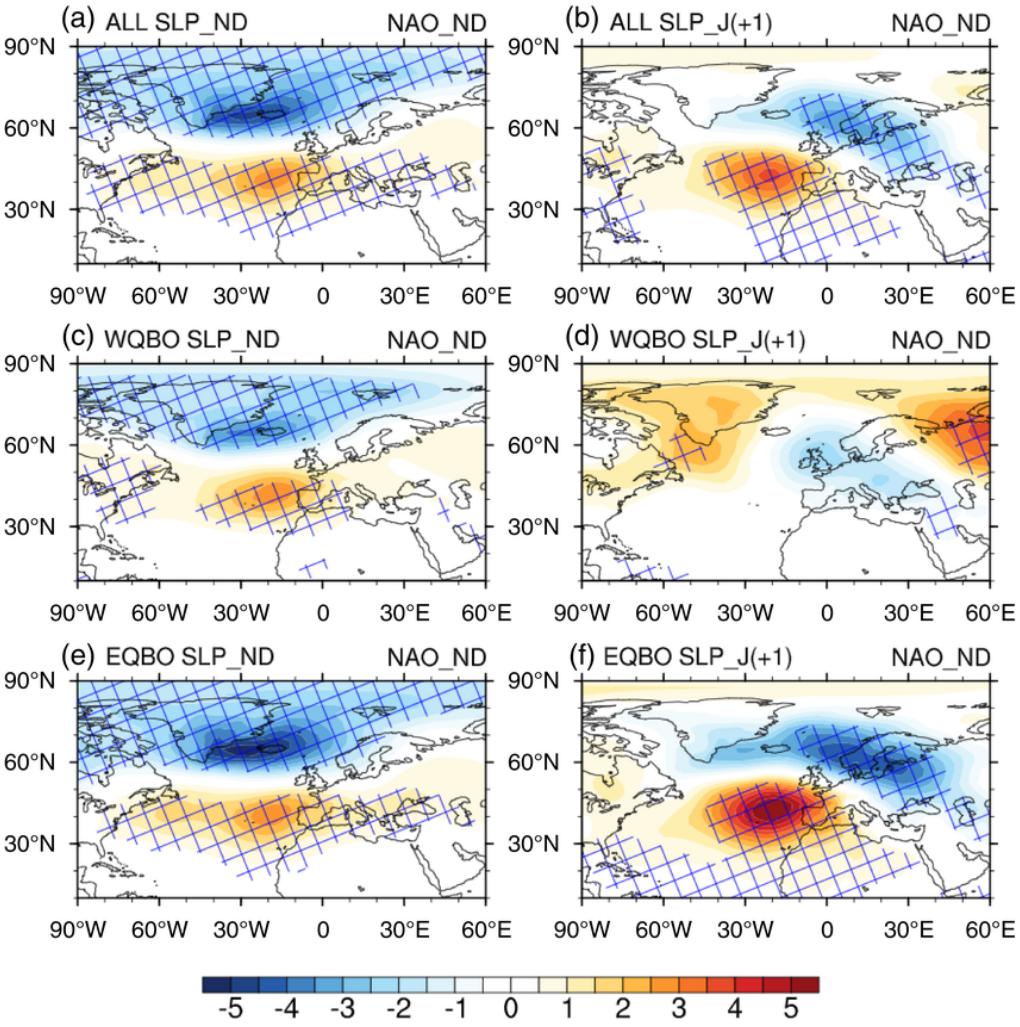

Figure 2.12: Regression patterns of sea-level pressure anomalies (shading, unit: hPa) against the normalized early winter NAO index in the simultaneous early winter (a) and the subsequent January (b) for all neutral ENSO years. (c, d) and (e, f) Same as (a, b) but for the QBOe winters and the QBOw winters, respectively. Blue hatched regions indicate anomalies significant at the 90% confidence level. Figure taken from Cai et al., 2022.

is the opposite, unfavourable conditions for waves to enter the stratosphere allowing the polar vortex to maintain its strength (Holton and Tan, 1980; O'Sullivan and Salby, 1990). Hence at the surface, during the QBOe phase induces NAO- conditions a weakened EDJ and increased blocking over the North Atlantic. Conversely, for the QBOw phase favours NAO+ conditions a strengthened EDJ and a lower chance of blocking (Gray et al., 2018) during the winter. It has also been shown that QBOe and QBOw winters also display different interannual variability. For the QBOe phase, during the early winter (November-December) an NAO- anomaly is more likely to persist through into the late winter (January-February). In the QBOw phase, NAO+ is likely to change in midwinter (Cai et al., 2022). This suggests that the QBOe phase increases the persistence of NAO- and blocking during winter. This is seen in Figure 2.12, which shows the strongest signal in sea level pressure at the start of January, following a negative NAO- during the QBOe phase in the early winter.

The work of García-Burgos et al. (2023), showed that there is a projected change in the EDJ in the early winter, with a poleward movement of the EDJ which then causes an equatorward shift moving into the late winter. In late winter, the equatorward shift was predominantly driven by changes in the polar vortex. Hence, given the work of Cai et al. (2022) showing intraseasonal variability in the North Atlantic circulation under each QBO phase, it raises the question of how much of the variability in García-Burgos et al. (2023) is driven by each QBO phase.

Madden Julian Oscillation

The Madden-Julian oscillation is a 30-90-day cycle of convection anomalies that propagates eastward from the east of Africa, over the Maritime Continent, and decays in the Pacific. It is one of the main drivers of subseasonal variability around the world, and over recent years studies have focused on how it influences variability in the North Atlantic. It is often defined by using the combined fields of outgoing long-wave radiation (OLR) and the lower and upper tropospheric zonal winds and broken down into eight phases corresponding to the location of maxima in its convective activity (Wheeler and Hendon, 2004). An example is shown in Figure 2.13 with

filled contours showing OLR anomalies and arrows depicting low-level wind anomalies.

The strong convective anomaly that is generated by the MJO generates Rossby waves that can propagate into the North Atlantic and hence influence regional variability. Using the four North Atlantic weather regime patterns, Cassou (2008) showed that there is a statistical link between the phase of the MJO and the occurrence of each weather regime. They showed that during phases 3 and 4 of the MJO there was a statistically significant increase in the occurrence of the NAO+ regime, and during phases 6 and 7 there was an increase in the NAO- regime, both occurring around 2 weeks after the onset of the MJO phase. The AR and BL regime did not show changes of the same magnitude during the MJO lifecycle. This connection has also been shown to be linked to extreme weather events in Europe. Knight et al. (2020) show through a set of relaxation experiments and hindcast datasets that an extreme MJO event during phase 6 of the lifecycle led to an extreme negative NAO event that caused large snowfall and disruption to the UK in February 2018 (Greening and Hodgson, 2019).

Few studies have investigated how the EDJ changes in response to the MJO phase. While it is known that the NAO is related to latitudinal changes in the EDJ, it is not clear if it would impact other features relating to the EDJ, such as its tilt or its strength. Yuan et al. (2011) explore the response of upper-level jet streams to precipitation anomalies in the Indian Ocean and the western Pacific which are correlated with the MJO. By defining shifts in the jet through the first principal component, they find that equatorward (poleward) movement of the jet leads (lags) anomalies over the Indian Ocean, and the opposite is found for events over the western Pacific. This relates to the results of Cassou (2008), with the same phases of the MJO corresponding to the same anomalies and expected behaviour of the jets during the respective phases of NAO. This shows that there is intraseasonal variability of the jet stream associated with the MJO. However, the definition of the jets by principal components and in the upper troposphere means that it is difficult to disentangle the variability associated with the subtropical and eddy-driven jets individually. Hence, it is not clear what effect the MJO has on the EDJ.

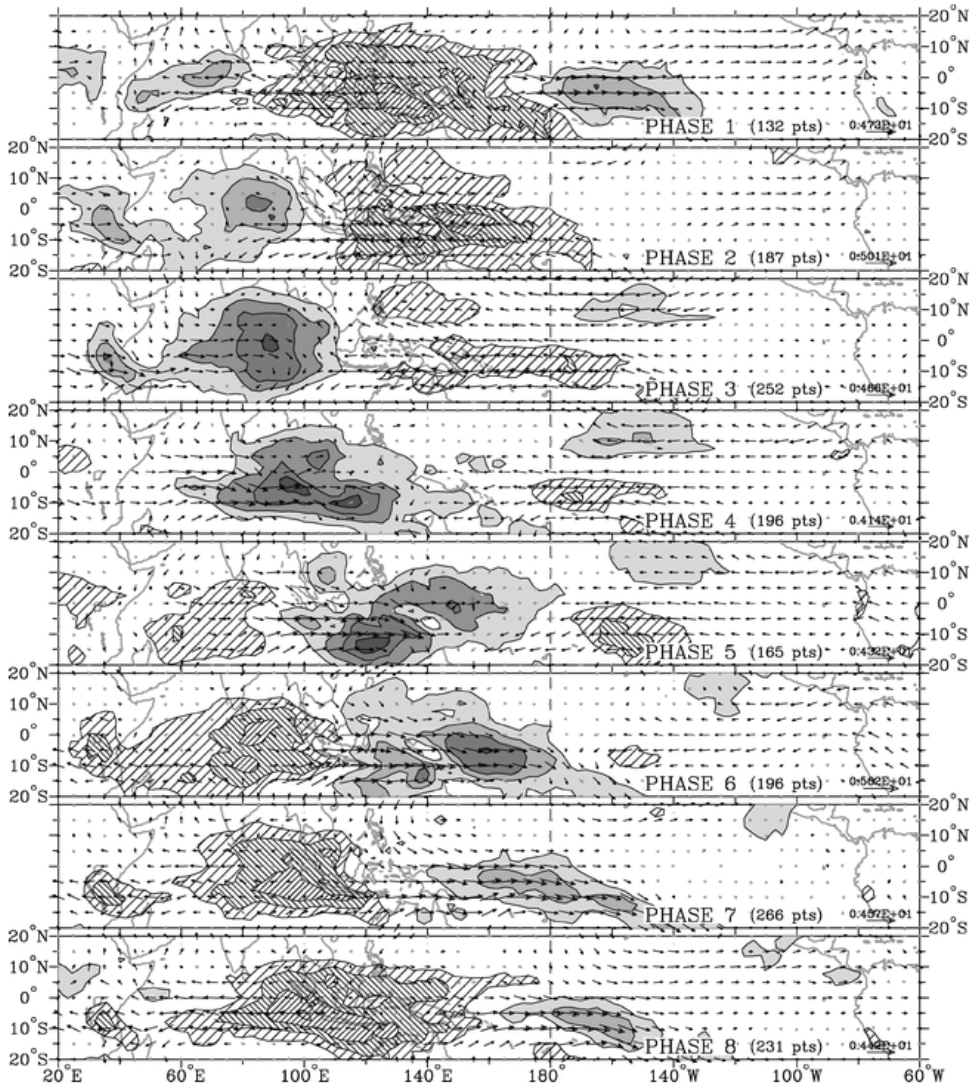

Figure 2.13: Composite anomalies of the OLR (filled contours) and 850hPa wind (arrows) for Northern Hemisphere winter of the 8 phases of the Madden-Julian Oscillation. Figure take from Wheeler and Hendon, 2004.

2.5 Predictability of the EDJ

Predicting the weather is important for providing early warnings and for understanding the changes in our weather and climate due to global warming. An important feature of the climate system related to predictability is its temporal characteristics, such as its persistence. For example, a major source of seasonal predictability is the stratospheric polar vortex, which can influence the future state of the sign of the NAO if modelled accurately. Each of the teleconnections discussed previously has been shown to contribute to seasonal forecast skill in the North Atlantic, if a seasonal forecast can accurately represent the teleconnection.

The persistence and predictability of the EDJ are essential to understand its long-term behaviour and its relationship with the NAO and EA patterns. Franzke et al. (2011) analysed the persistence properties of the variability of the North Atlantic climate, suggesting that the slow decay of the autocorrelation function with increasing lag indicates the potential extended-range predictability of the eddy-driven jet during winter. This is shown to be true for some seasonal forecasting models by Parker et al. (2019), who show that on seasonal timescales some models have the ability to predict the latitude of the EDJ during winter, but they cannot predict the strength of the EDJ. Looking at longer timescales, decadal forecasts show predictability in the speed of the EDJ but not in the latitude (Marcheggiani et al., 2023).

One of the main problems that has been shown to occur in both seasonal forecasting and climate models when representing future states of the atmosphere is the signal-to-noise paradox (Scaife and Smith, 2018; Strommen and Palmer, 2018). In Scaife and Smith, 2018, they show that the skill of the seasonal forecasting model GloSea5 (MacLachlan et al., 2014) has a better skill (correlation between the ensemble mean and observations) to predict the observed NAO rather than the modelled NAO. They go on to show that it is particularly prevalent in the North Atlantic.

Trying to diagnose the reason behind this problem is difficult, and many physical and computational reasons have been suggested as sources of the paradox (Weisheimer et al., 2024). Strommen and Palmer (2018) model the NAO as a bimodal regime system of the EDJ latitude and show that

the signal-to-noise paradox is the result of an underestimation of the persistence of the regimes. In the following work, Strommen (2019) attribute a large amount of seasonal predictability to NAO from the persistence and interannual variations in the trimodal regime structure of EDJ from Woollings et al. (2010).

A potential source of the lack of persistence is the too weak eddy-feedbacks in models. Hardiman et al. (2022) found across 17 seasonal forecasting systems that positive feedback on EDJ from synoptic scale eddies was systematically too weak in all models. However, it was later shown in Saffin et al. (2024), that while eddy feedbacks are important for persistence, it is not sufficient to explain fully why the persistence is too low across the models.

2.6 Summary

This chapter provided the necessary background for the thesis by outlining the physical mechanisms that form and drive variability in the EDJ. We began with the fundamental balance between meridional temperature gradients and thermal wind balance and showed how baroclinic and barotropic instabilities generate atmospheric eddies that transport heat and momentum up to the tropopause, where their convergence (diagnosed by the Eliassen-Palm flux in its TEM form) forms and sustains the EDJ. Following this, I turned to the concept of atmospheric regimes, first in idealised models and then in observations. I explored the idea of regimes in the atmosphere and how the early studies of Charney and DeVore (1979), highlighted zonal and blocked regimes of the large-scale atmospheric flow. However, follow-up work showed that in Tung and Rosenthal (1985) and Tung and Rosenthal (1987) under more realistic conditions these regimes were not found.

In observations, researchers have used both clustering of low-frequency geopotential heights and direct jet diagnostics to uncover recurring circulation states (Vautard, 1990,Madonna et al., 2017). k-means applied to the winter geopotential height of 500 hPa (or mean sea level pressure) consistently yield four Euro-Atlantic weather regimes, NAO+, NAO-, Scan-

dinavian blocking and the Atlantic Ridge, each associated with distinct surface impacts on temperature and precipitation.

For regimes in the EDJ, Woollings et al. (2010) introduced the daily Jet Latitude Index (JLI), which identifies the 850 hPa eddy-driven jet core and shows a trimodal distribution: southern, central and northern latitude peaks - on winter days. These preferred positions have since been tied to cyclonic versus anticyclonic Rossby wave breaking, to the combined NAO/EA phase space, and to transitions whose probabilities reflect underlying dynamical pathways. Madonna et al. (2017), tries to link how the regime structure of the JLI relates to the Euro-Atlantic regimes and suggests the introduction of two more jet regimes that capture the tilting and blocked states of the EDJ. However, I also discussed that the zonal-average, latitude-only view can be misleading. In particular, White et al. (2019) demonstrated that many of the northern-regime events in the JLI are actually orographically forced Greenland tip jets, not true mid-latitude eddy-driven jets. This finding calls into question the physical reality of the northern mode in the JLI and underscores the need for metrics that separate local, terrain-driven jets from the large-scale EDJ. Further, the use of the k-means clustering also presents complications in particular the choice of the number of clusters is not easy, as highlighted in Christiansen (2007) the preferred choice are highly sensitive to the time period, preprocessing and the domain.

Next, I reviewed the remote drivers that modulate the EDJ regimes. ENSO forces Rossby-wave trains via both a tropospheric Caribbean pathway and a stratospheric Polar Vortex pathway, producing early-winter NAO+ and poleward-shifted jets in El Niño and late-winter reversals toward NAO- and equatorward shift in the EDJ (Ayarzagüena et al., 2018; Maycock et al., 2020; O'Reilly et al., 2024). The QBO modulates stratospheric wave filtering (Holton and Tan, 1980), with the easterly phase weakening the vortex and favouring NAO- and southward-shifted jets, and the westerly phase doing the opposite (Baldwin et al., 2001; Cai et al., 2022). The 30–90 day convective activity of the MJO excite downstream wave trains that produce NAO+ and poleward-jets two weeks after phases 3–4 and NAO- and equatorward-jets after phases 6–7 (Cassou, 2008; Yuan et al.,

2011). Many of these studies discuss changes in the EDJ from the point of view of the JLI, which restricts it to latitude and strength and leaves out other features of the EDJ such as tilt (Barriopedro et al., 2022).

Finally, I discussed predictability and model limitations. The EDJ shows slow autocorrelation decay, suggesting subseasonal to seasonal skill, while state-of-the-art seasonal systems predict jet latitude of the JLI moderately well but are not as good at predicting the jet strength, while decadal forecasts show the opposite. A pervasive signal-to-noise paradox in models (Eade et al., 2014; Scaife and Smith, 2018) points to under-represented teleconnections, transient-eddy feedbacks, air–sea coupling errors and coarse resolution (Weisheimer et al., 2024). In particular, no work has directly attributed which flawed wave–mean-flow processes or which regime definitions most aggravate forecast errors.

Altogether, this thesis aims to address the following gaps in the literature:

- Characterise other features of the EDJ (such as the tilt) with an approach that does not rely upon zonal averaging
- Investigate relationships between the more features of the EDJ and how different remote drivers (ENSO, QBO and the MJO) impact them.
- Explore the potential predictability of the various components of the EDJ and how a seasonal forecasting model represents the EDJ.

Chapter 3

Characterising the North Atlantic eddy-driven jet using two dimensional moment analysis

Parts of this chapter are published in the journal Weather and Climate Dynamics Perez et al. (2024)

3.1 Introduction

European weather and climate are largely driven by changes in the Eddy-Driven Jet stream (EDJ). The ability to characterise EDJ on different time scales has been the subject of many different studies Parker et al. (2019), Simpson et al. (2019), and Woollings et al. (2010, 2018), where a variety of techniques of varying complexity have been developed to define different characteristics of the EDJ. These methodologies range in complexity, but can be largely separated into two categories representing their use of the upper or lower troposphere.

Approaches that use the upper-troposphere typically use a three-dimensional (height, latitude, longitude) wind field, identifying local wind maxima using a selected threshold Koch et al. (2006), Limbach et al. (2012), and Manney

et al. (2014). There are other approaches that use horizontal wind shear defined on the surface of 2PVU Spensberger et al. (2017), which define jet axes that are able to characterise the EDJ and the STJ separately based on select criteria Spensberger et al. (2023).

Lower-tropospheric metrics are much more widely used, where zonal averaging plays a pivotal role in defining the EDJ latitude and strength. Their popularity stems from the connection to the zonal momentum budget, but also from the fact that many of the methods are relatively simple and easy to implement. The most popular approach is the Jet Latitude Index (JLI) defined in Woollings et al. (2010), where the maximum of the zonally averaged lower tropospheric winds is used to define the latitude of the EDJ and the maximum value is used to define the strength. When applying this approach to the North Atlantic during winter (December-February), Woollings et al. (2010) shows that there are three distinct peaks in the distribution of the JLI, where each peak defines a northern (N), central (C), and southern regime (S). This result motivates the existence of regime behaviour in the EDJ, which has led to multiple studies investigating the relationship of each regime to other atmospheric phenomena such as storm tracks Novak et al. (2015), sudden stratospheric warmings Maycock et al. (2020), weather regimes Madonna et al. (2017), and also the predictability of the EDJ within each regime Frame et al. (2011).

However, there are some issues with the JLI and its interpretation. The first problem that has been shown with the regimes of the JLI is with the N regime. In a set of experiments, White et al. (2019) shows that the N regime occurs predominantly when Greenland tip jets occur. The other problem is with the zonal averaging step, where the definition of the maximum in the profile becomes problematic if the profile is bimodal or if the averaged profile is very wide Woollings and Blackburn (2012). Other studies have tried to tackle these issues by calculating the maximum zonal wind at each meridian and using each point to define the latitude or by applying a latitude weighting to the JLI to prevent selecting a maximum associated with winds that are smaller in area Ceppi et al. (2014). These approaches still have problems specifically with zonal winds that are separated but of equal strength, where defining a single maximum in the one-dimensional

or zonally averaged field is not clear and extra criteria are needed, and the weighting will select the latitude between the two peaks due to the nature of the calculation.

By introducing a zonal average to the calculation, you also remove a unique feature of the EDJ, that is, its tilt. The tilt of the EDJ is a less explored metric, but has been measured using either the low-level wind speed Messori and Caballero (2015) or the zonal wind Barriopedro et al. (2022), but using the maximum at each meridian. The Jet Angle Index (JAI) defined in Messori and Caballero (2015) introduces additional criteria to filter out meridians with a split jet to get a better measure of the tilt of the jet.

The clear issue in these approaches is the use of a one-dimensional profile to characterise the EDJ, whether that is obtained through zonal-averaging or by defining a measure at each meridian. Hence, the goal of this chapter is to introduce a new approach to characterising the EDJ in the North Atlantic that does not require zonal averaging and is capable of defining all the metrics of interest when studying the EDJ; the latitude, strength, and tilt. This approach defines what I call an Eddy-Driven Jet Object (EDJO). With this new method, I will compare the equivalent measures to the JLI and try to answer the following questions.

- Are the three regimes of the JLI realised when no zonal averaging is used ?
- Can anything be learned about the regime transitions of the JLI with a two-dimensional approach ?
- How do the measures of the new approach relate to other modes of variability in the North-Atlantic.

The chapter is broken down as follows: In Section 2, the dataset and the variables that will be used throughout this chapter, along with the definitions of the JLI and the JAI. Section 3 outlines in detail the new approach for characterising EDJs with EDJOs. Section 4 explores the temporal variability of the JLI and the EDJOs; Section 5 looks at the winter statistics of the JLI, JAI, and the EDJOs, where I highlight the sources of the differences in each measure, and Section 6 looks at how the EDJOs are related

to the two leading modes of variability in the North Atlantic, that is, the North Atlantic Oscillation (NAO) and the East Atlantic pattern (EA). The chapter ends with Section 7 which contains a discussion and a conclusion.

3.2 Data and methods

For this chapter, I will use 850hPa zonal winds (U_{850}), to capture winds that are largely associated with the EDJ. The data for this chapter will come from the ERA5 reanalysis (Hersbach et al., 2020) and I am interested in December - February (DJF) between 1979 and 2020. The examples used to describe the algorithm are defined in the same North Atlantic domain as in Woollings et al. (2010), which is 15-75°N and 0-60°W. Each of the wind fields are processed using a 10 day low-pass Lanczos filter (Duchon, 1979) with a 61-day window to remove synoptic scale variability associated with individual weather systems.

3.2.1 Definition of the JLI and the JAI

The methods with which I am going to compare are the Jet Latitude Index (JLI) of Woollings et al., 2010 and the Jet Angle Index of Messori and Caballero (2015). The JLI is one of the most widely used methods for defining the latitude and speed of the EDJ, and the JAI is not as widely used, but its methodology is similar to those used to measure the tilt.

The JLI is the maximum of the zonally averaged zonal winds at 850hPa, where I calculate the maximum from a 3rd degree fitted polynomial. From this, you are also able to define an EDJ speed, which I will call JLI_{vel} The JAI is calculated using the wind speed at 850 hPa, where the maximum is found at each meridian across the basin. If a meridian has a secondary maximum within 4ms^{-1} of the largest maximum and is further than 5° latitude away, then it is ignored. This is to remove any split jets from the calculation. A linear regression across the points is applied to give a line of best fit, which is used to calculate an angle between -180° and 180° that

is calculated using the following definition,

$$\text{JAI} = \text{atan2}(\Phi_1 - \Phi_0, \Lambda_1 - \Lambda_0) = \begin{cases} \arctan(\frac{\Phi_1 - \Phi_0}{\Lambda_1 - \Lambda_0}) & \text{if } \Lambda_1 - \Lambda_0 > 0, \\ 90^\circ - \arctan(\frac{\Lambda_1 - \Lambda_0}{\Phi_1 - \Phi_0}) & \text{if } \Phi_1 - \Phi_0 > 0, \\ -90^\circ - \arctan(\frac{\Lambda_1 - \Lambda_0}{\Phi_1 - \Phi_0}) & \text{if } \Phi_1 - \Phi_0 < 0, \\ \arctan(\frac{\Phi_1 - \Phi_0}{\Lambda_1 - \Lambda_0}) \pm 180^\circ & \text{if } \Lambda_1 - \Lambda_0 < 0, \\ \text{undefined} & \text{if } \Lambda_1 - \Lambda_0 = 0 \\ \text{and } \Phi_1 - \Phi_0 = 0, & \end{cases} \tag{3.1}$$

where (Φ_0, Λ_0) and (Φ_1, Λ_1) are the start and end points of the best fit line. Before the calculation of the JLI and JAI, the same low-pass filtering is applied to the wind fields to remove short-scale variability.

3.3 Eddy-Driven Jet Objects

3.3.1 EDJO identification

The identification of an Eddy-Driven Jet Object (EDJO) is outlined by the flow chart shown in Figure 3.1. In detail, each step is as follows:

1. **Locate seed points** - Seed points are identified as local maxima in the U_{850} field, denoted $U_{\max}$. To focus on eddy-driven westerly jets, I define a minimum zonal wind threshold for seed points, U^*_{850}, which is set to $8\,\text{ms}^{-1}$ for this study. This value has been used in other studies to isolate the winter eddy-driven jet (Woollings et al., 2010). Note that multiple seed points may be identified in an image. If $U_{\max} < U^*_{850}$, then no EDJO is found for that day and the rest of the steps are skipped.

2. **Flooding** - Starting from the seed point with the largest wind maximum, all neighbouring grid points where $U_{850} \geq U^*_{850}$ are recursively tagged, and a contour enveloping these points is defined as the EDJO (see contour in Figure 3.1). The neighbouring points include those that are above, below, left, right, and diagonally adjacent to the seed point.

3. **Length check** - A key feature of EDJs is that they are large-scale zonal jets. To remove small-scale local wind features, I apply two length checks to the EDJO identified in Step 2. First, I require the geodesic length of an EDJO, L, to satisfy $L \geq L^*$. To calculate L, a line is extrapolated through the centre of mass of the object and along the major axis, with the distance between the two points that intersect the edge of the EDJO being used. The definitions of centre-of-mass and major axis are given in the next section. The precise value of L^* is somewhat arbitrary, but I choose it to be the geodesic length of a purely zonal jet at the highest latitude in our domain (75°N) which is 1661km; note that this is larger than the Rossby radius of deformation in the mid-latitudes of around 1000km.

   Second, I require that the EDJO extends over a minimum longitudinal extent, so that the longitude range spanned by the EDJO must satisfy $L_\lambda \geq L^*_\lambda = 20°$. If either of these length checks are not met, then the EDJO is rejected.

4. **Remaining Maxima** - To avoid duplicating EDJOs (e.g., if more than 1 maximum lies within a single EDJO), the associated grid points from the previous EDJO are removed from the U_{850} field. If there are any other remaining seed points, then the algorithm returns to step 2 and repeats. This is an advantage over previous methods as it enables the characteristics of split jets to be retained. Once there are no remaining U_{850} maxima, the algorithm moves to the next time step.

3.3.2 Moments

Moments are common in statistics for defining properties of a distribution, such as the mean or the variance. The definition used here is

$$M_{pq} = \int\int_{\Omega} \lambda^p \phi^q U_{850}(\lambda, \phi)\, r^2 \sin\phi \, d\lambda d\phi, \tag{3.2}$$

where Ω is the EDJO, λ and ϕ are the longitude and latitude, respectively, and $r^2 \sin\phi d\lambda d\phi$ is the area element on a sphere where r is the radius of the Earth. This formulation is similar to that applied to the potential vorticity

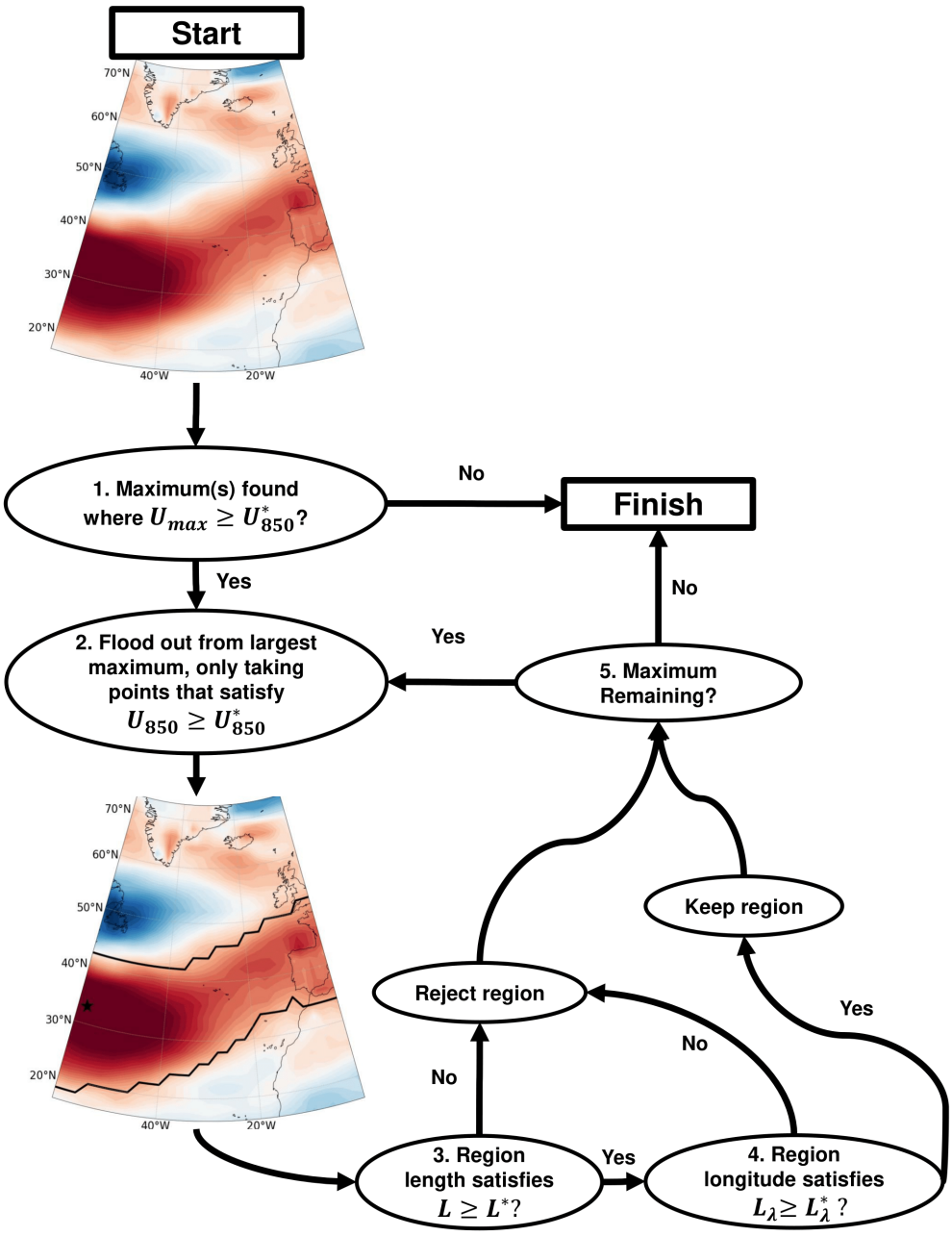

Figure 3.1: Algorithm for identification of Eddy-Driven Jet Objects (EDJOs). In the map, the black star is the seed point and the black contour is the EDJO found from the seed point.

distribution for studying the stratospheric polar vortex (D. N. W. Waugh, 1997). A key difference is that I have chosen to include the strength of the zonal wind as a weighting in the calculation. The inclusion of the weighting factor U_{850} in equation (1) means that our moment calculations (of position and tilt) will reflect regions of stronger zonal wind within the EDJO, which is important in the context of surface impacts. The lack of weighting results in purely geometric moments, as used in some previous studies (D. N. W. Waugh, 1997; D. W. Waugh and Randel, 1999).

The weighting factor also allows us to calculate quantities that are analogues of those used to quantify planar objects in mechanics (mass, centre of mass, major and minor axes), where the weighting factor is simply the surface density (i.e., mass per unit area). Hence, the mass of an EDJO is defined to be $U_{\text{mass}} = M_{00}$, with units of $\text{m}^3\,\text{s}^{-1}$. The average jet strength, U_{mean}, with units of $\text{m}\,\text{s}^{-1}$, is then

$$U_{\text{mean}} = \frac{U_{\text{mass}}}{\int\int_{\Omega} r^2 \sin\phi d\lambda d\phi}, \tag{3.3}$$

which is analogous to the average surface density in planar mechanics. The jet position can be described by the analogue of the centre of mass, which arises as a longitude $\overline{\lambda}$ and latitude $\overline{\phi}$ defined by

$$\overline{\lambda} = \frac{M_{10}}{M_{00}}, \quad \overline{\phi} = \frac{M_{01}}{M_{00}}. \tag{3.4}$$

The jet orientation is described by the major axis, which requires analysis of the analogue of the inertia matrix I, here defined by

$$\mathsf{I} = \begin{pmatrix} \tilde{M}_{02} & -\tilde{M}_{11} \\ -\tilde{M}_{11} & \tilde{M}_{20} \end{pmatrix}, \quad \text{where} \quad \tilde{M}_{pq} = \int\int_{\Omega} (\lambda - \overline{\lambda})^p (\phi - \overline{\phi})^q U_{850}(\lambda, \phi)\, r^2 \sin\phi d\lambda d\phi. \tag{3.5}$$

The major axis of the EDJO is the direction of the eigenvector associated with the smaller eigenvalue of I. I define the jet tilt, α, as the angle between the major axis and the latitude line $\phi = \overline{\phi}$, with positive values indicating a SW-NE tilt and vice versa. For EDJOs with $\tilde{M}_{20} > \tilde{M}_{02}$, i.e., those elongated longitudinally rather than latitudinally, as should be guaranteed by the length checks in step 3 of the algorithm there is a simple expression

for α:

$$\alpha = \frac{1}{2} \arctan \left(\frac{2\tilde{M}_{11}}{\tilde{M}_{20} - \tilde{M}_{02}} \right), \tag{3.6}$$

as also used in Matthewman et al., 2009.

3.3.3 Example cases

To motivate each of the methods, Figure 3.2 shows two days in which the EDJO, JLI, and JAI have been applied. Figures 3.2a and c show U_{850} from which the moment analysis and the JLI is calculated, and b) and d) show WS_{850} which is used for the calculation of the JAI. For the first day (Figures 3.2a and b), $\overline{\phi}$ and the JLI agree well with the position of the EDJ. However, there is some disagreement between the JAI and α, which show opposite signs. Compared with the U_{850} and WS_{850} fields on this day, the magenta points below Iceland in Figure 3.2b lie within the easterly winds of the U_{850} field. Hence, those points lead to the positive JAI on this day, but this is due to the use of points that do not define the EDJ, leading to an incorrect value of the tilt. Only using U_{850}, the notion of direction is preserved and, hence, only westerly winds are used to calculate the tilt, and α gives an accurate measure of the tilt for this day. In addition to this, there is a sparse sampling of meridians due to the criteria of removing meridians where split jet occurs.

For the second day (Figures 3.2c and d), the opposite is shown, where there is good agreement between α and the JAI but not with $\overline{\phi}$ and the JLI. This is attributed to the tilted EDJ structure that can be seen in the westerlies in Figure 3.2. From the stronger equatorward westerlies, the JLI picks out the equatorward position, but due to the extension of the winds up and over the UK $\overline{\phi}$ gives a centralised latitude that better encapsulates the overall structure of the EDJ on this day. These examples highlight some of the issues when it comes to interpreting the results from the JLI and the JAI, and where moment-based analysis overcomes these pitfalls.

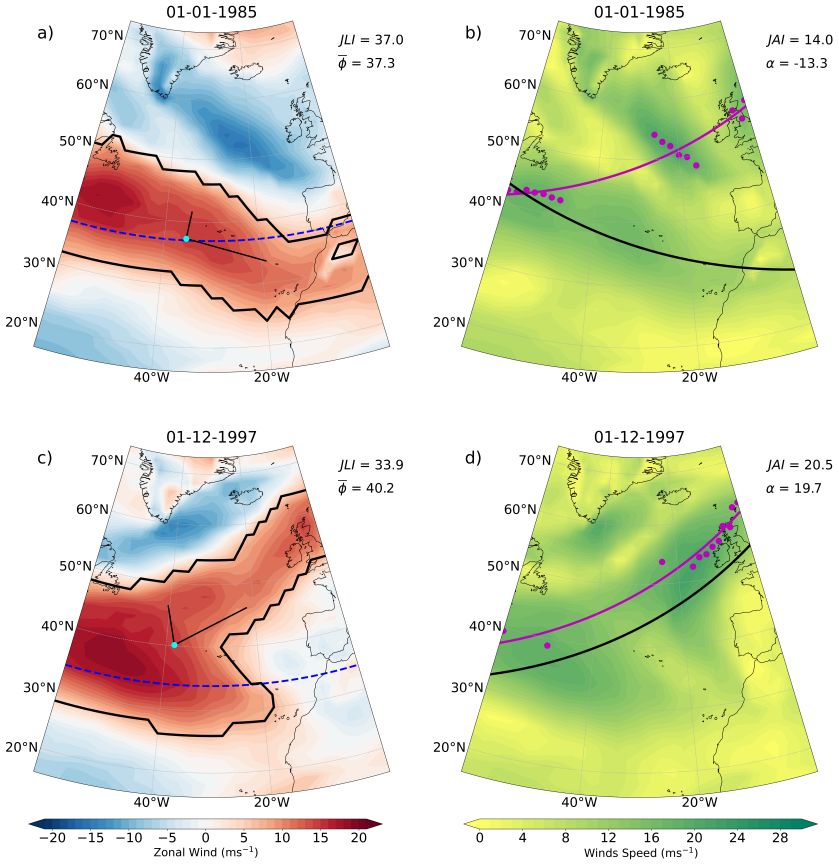

Figure 3.2: U_{850} (a,c) and WS_{850} (b,d) for two different days (rows). The dashed blue line denotes the JLI. The light blue dot is the position of $(\overline{\lambda}, \overline{\phi})$ the centre of mass. In b) and d), the magenta circles are the maxima at each meridian, and the magenta line is the result of a linear regression fitted to those maxima following Messori and Caballero (2015). The JAI in b) and d) is calculated from the end points of the magenta line, and the solid black line is the tilt given by α, which comes from the horizontal black line emanating from the centre of mass in a) and c). The values of the indices for the respective methods are given at the top right of each panel.

3.4 Temporal variability

3.4.1 Winter 2016/17

I will now consider the temporal variability of the EDJ diagnostics, where I highlight the cases that cause differences between the EDJO metrics and the JLI and JAI. Starting with Figure 3.3, this shows the evolution of $\overline{\phi}$ and the JLI during the winter of 2016/17. Days with a single EDJO are marked with black crosses, two EDJOs are marked with pink triangles, and the JLI in blue. The evolution of the EDJ by the EDJOs gives a different view from that of the JLI. From $\overline{\phi}$ you can see periods of single and two EDJOs, indicating periods of split jets over the course of a single winter. Due to defining a single maxima with the JLI, this is not captured and during the periods of two EDJOs the JLI is found to be predominantly poleward.

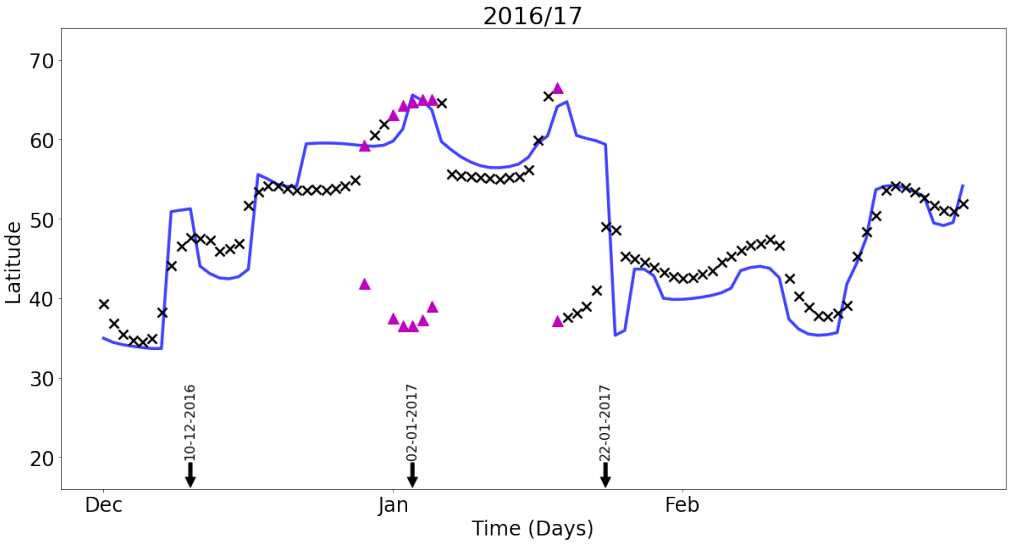

Figure 3.3: Time series of $\overline{\phi}$ (black crosses) and the JLI (solid blue line) for the boreal winter 2016/17. Pink triangles represent days with EDJOs. The black arrows indicate starting dates for the consecutive days shown in Figure 3.4.

During a single winter, the JLI has been shown to display large jumps in latitude Madonna et al., 2017; Woollings et al., 2010 and this has been interpreted as a regime change with changes to preferred latitudes Franzke et al., 2011; Hannachi et al., 2011; Novak et al., 2015. This can be seen

during the course of this winter for the JLI, but the same changes are not seen in $\overline{\phi}$. To explore this further, the day before and after the large shift in the JLI that I am interested in is marked by the arrows and the dates in Figure 3.3 are shown in Figure 3.4. The first pair of days is shown in Figures 3.4a and b, where the JLI moves equatorward by 8° but $\overline{\phi}$ remains unchanged. This is an example of a broad jet whose overall structure persists and is captured by the EDJO, and hence $\overline{\phi}$ also captures this persistence. Due to zonal averaging, the JLI does see this and hence changes in response to small fluctuations in the zonal wind field within the structure. The next pair of days highlights a feature of EDJO identification that is the ability to capture split jets, represented as two EDJOs shown in Figures 3.4c and d. The JLI misses out on identifying these days because it only identifies a single maxima on a given day. The last pair of days in Figures 3.4c and d shows an example of an extremely tilted jet captured by the EDJOs. The JLI during this period shows a large shift of 25°. Initially, the JLI defines a northerly EDJ close to the tip of Greenland, but a slight strengthening of the westerlies over the west of Africa causes it to suddenly switch from one day to the next. However, as seen from the EDJO the tilted structure remains relatively unchanged over the transition in the JLI, which is reflected both in $\overline{\phi}$ and α.

3.4.2 Winter 1998/99

The next time series is shown in Figure 3.5, which shows the evolution of $\overline{\phi}$ and the JLI over the winter of 1998/99. There are similarities in the evolution of each metric, as shown in Figure 3.3, where there are sharp changes from one day to the next in the JLI that are not seen in $\overline{\phi}$. During this winter there are some days in February where no EDJO has been defined (marked by the red ticks in Figure 3.6), around these days you can see some sharp transitions in the JLI likely due to the much weaker or smaller regions of westerlies during this time.

Following a similar approach to Figure 3.3, I have selected days around large changes in the JLI marked by the arrows with the dates in Figure 3.5, which are shown in Figure 3.6. Figures 3.6a and b show another case of a broad jet but with two strong regions of very strong westerly winds. During

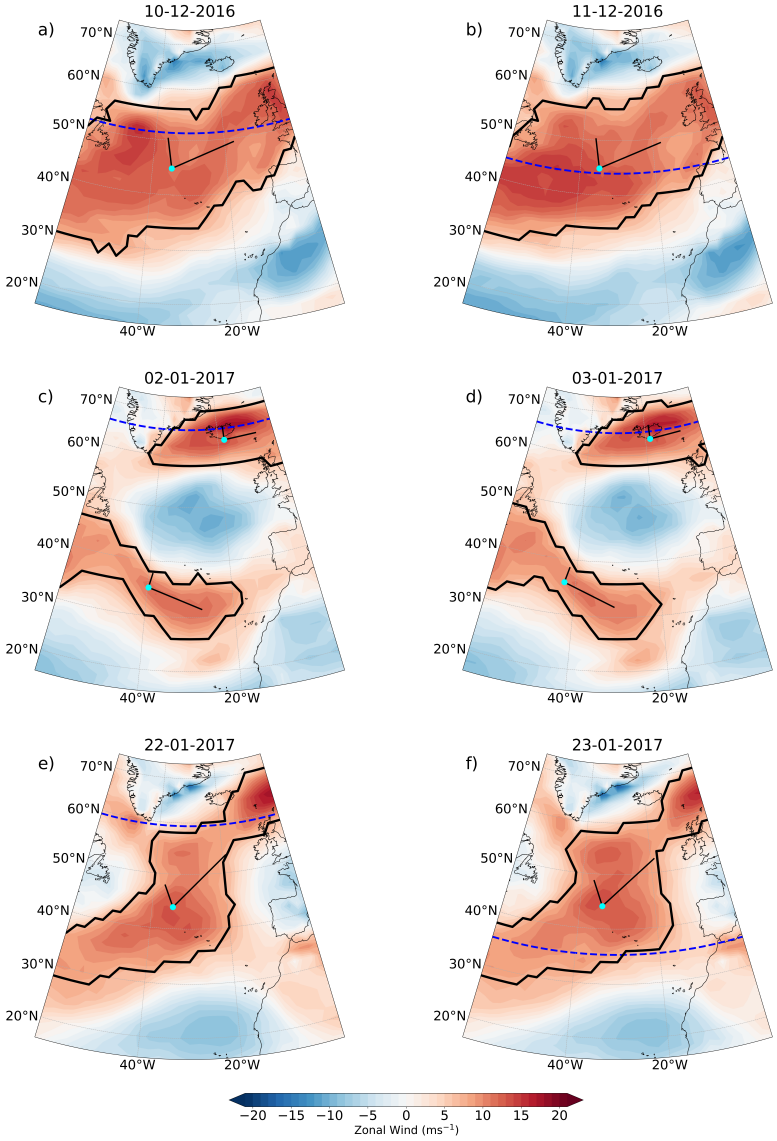

Figure 3.4: Example days taken from the arrows shown in Figure 3.3 of the U_{850} field. The dashed blue lines denote the value of the JLI on each day. Solid black contours denote the EDJO. The light blue dots represent the centre of mass $(\overline{\lambda}, \overline{\phi})$ of the EDJO, with the longer black line denoting the major axis and the smaller the minor axis.

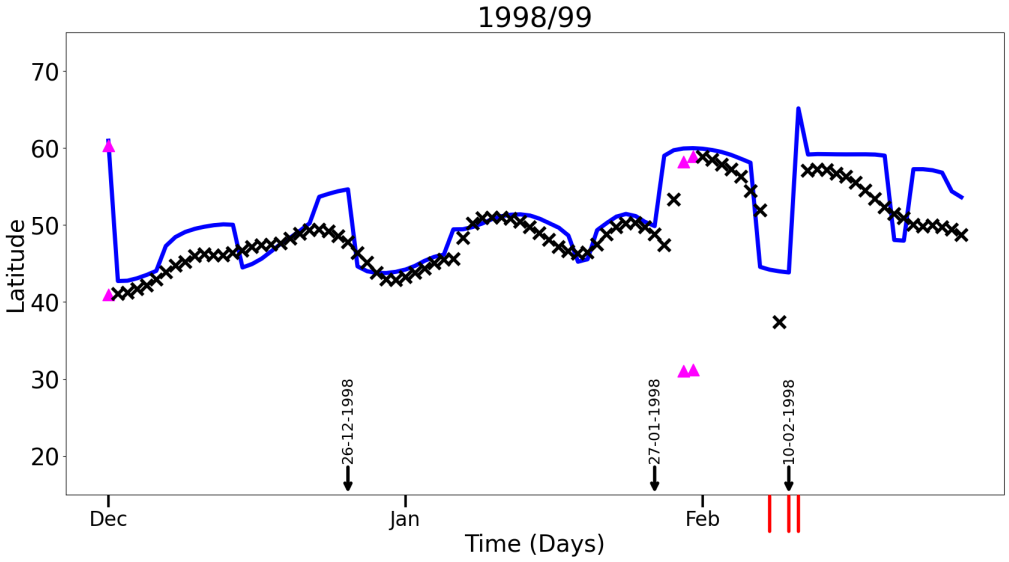

Figure 3.5: Same as Figure 3.4 but for the boreal winter of 1998/99 and red ticks mark the days where no EDJO is defined.

this period, the JLI again shifts equatorward by 10° due to weakening in the region south of Greenland. However, it can be seen that the overall structure of the EDJ is unchanged during this time, which is reflected by the EDJO contour and by $\overline{\phi}$. This again highlights the issue of defining a single maxima, but now for the case of a broad jet, where it is unclear or difficult to select the "correct" peak to use as your position. The next example in Figures 3.6c and d shows another case of a tilted EDJ, which is captured in the value of α. Here, the JLI shifts poleward 9° under local changes in the westerlies when again the structure is unchanged. The final example (Figures 3.4e and f) is where the identification algorithm does not define an EDJO over the two days. It can be seen why, as the westerlies over this period are very weak and any regions of the westerlies that meet the 8ms^{-1} threshold are too small to pass the length checks. However, the JLI will always define a position no matter the size or strength of the westerlies and again a poleward shift of 20° can be seen just due to a slight strengthening of the westerlies over Iceland.

The two winters shown here highlight the cases where the JLI incorrectly characterises the EDJ: 1) broad jets, 2) highly tilted jets, 3) split jets, and 4) no well-defined jets. On these types of days, the JLI tends to shift

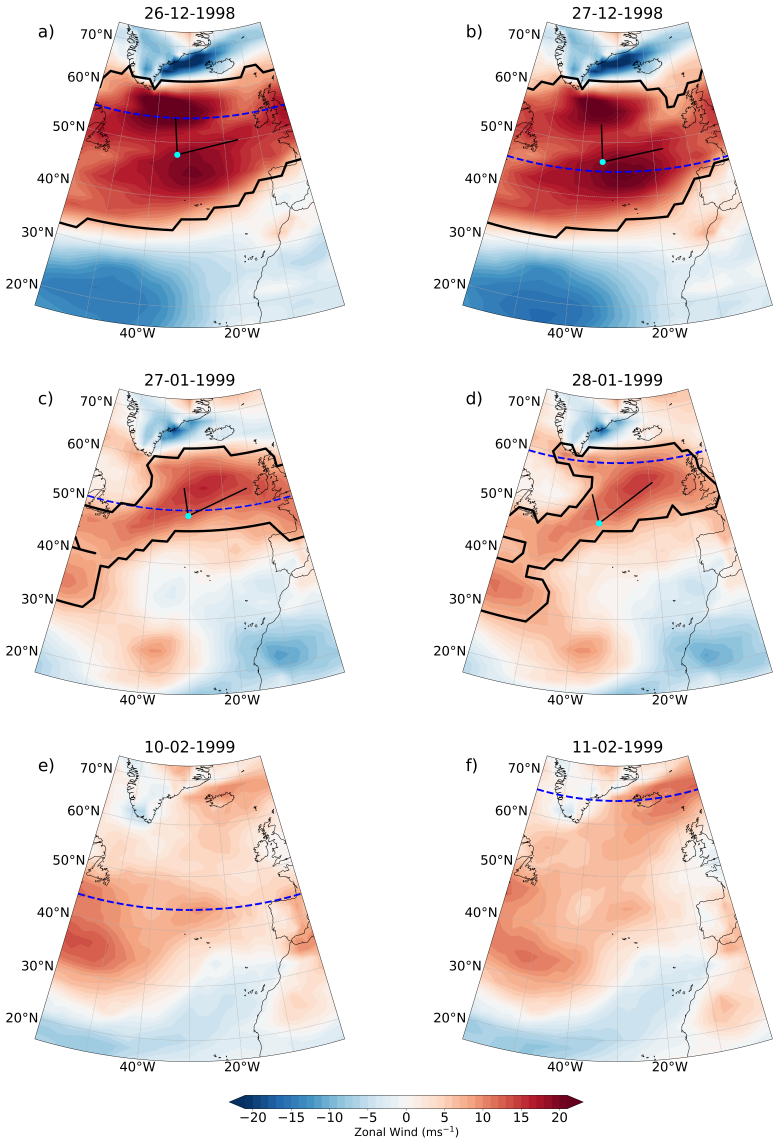

Figure 3.6: Same as Figure 3.4, but days are taken from the arrows in Figure 3.5.

poleward or equatorward by large amounts, under little to no change in the overall westerly wind field on those days, whereas $\overline{\phi}$ tends to capture this persistence in the EDJ during these events. To further evidence this, I define a large shift in either the JLI or $\overline{\phi}$ when either of the metrics shifts by 10° in latitude either equatorward or poleward. For $\overline{\phi}$, this is only calculated for days when a single EDJO is defined to prevent switching between the largest EDJOs U_{mass} on consecutive two EDJO days. Figure 3.7 shows the number of occurrences of large shifts in each winter, with the JLI in blue and $\overline{\phi}$ in red. This shows that the JLI is prone to frequent large shifts in each winter, with a mean occurrence that is seven times greater than that of $\overline{\phi}$. Hence, the cases shown in Figures 3.4 and 3.6 are representative of other years.

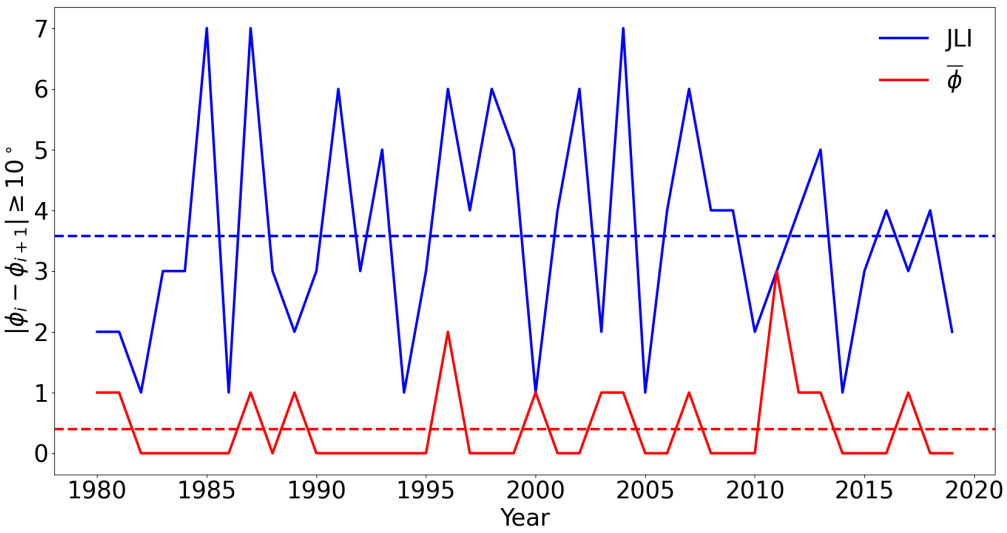

Figure 3.7: Frequency per winter of large shifts ($\geq 10°$) in the EDJ latitude between consecutive days. The blue line shows the shifts for the JLI and the red for $\overline{\phi}$ for each winter in 1979-2020. The horizontal dashed lines show the average frequency in the colour of the respective measure of the EDJ latitude. The calculation of large shifts for $\overline{\phi}$ is only done on days where a single EDJO is defined.

3.4.3 Persistence

Evidence from Figures 3.3 and 3.6 has shown that the JLI exhibits higher variability than $\overline{\phi}$. To further study this, the autocorrelation (ACF) has been calculated for all metrics in all winters, and the result is shown in

Figure 3.8. Figure 3.8a shows the ACF for the JLI and $\overline{\phi}$, where $\overline{\phi}$ has a systematically higher correlation for lags of up to ten days, resulting from sudden and large changes in the JLI that would reduce its persistence. Looking at α and the JAI (Figure 3.8 b), they show similar persistence, with α having slightly higher persistence up to a delay of four days, where the JAI starts to show a higher correlation. In Figure 3.8c, the ACF of different measures of EDJ strength is shown. Surprisingly, JLI_{vel} has higher persistence than U_{mean} and U_{max}. Given that U_{mean} is the average of the points within an EDJO, you might expect it to have higher persistence, but this is not the case based on the data shown here. For U_{max}, this can be attributed to the potential switch between different maxima when searching the two-dimensional field each day, giving a lower persistence, but not dissimilar from that of U_{mean}. The measure of EDJ strength that shows the highest persistence is U_{mass}, which has a significantly higher ACF than each other method on all lags. This suggests that the size of the EDJ is a longer-lasting feature than just its strength.

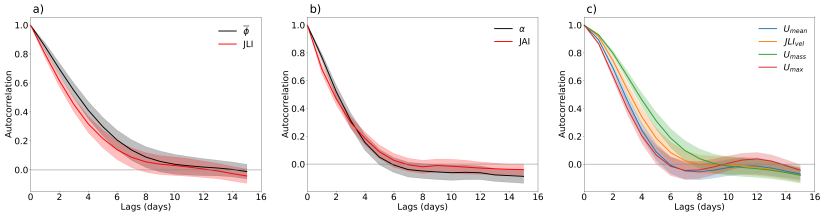

Figure 3.8: Lagged autocorrelation functions for a) $\overline{\phi}$ (black) and the JLI (red); b) α (black) and the JAI (red) and c) U_{mean}, U_{max}, U_{mass} and JLI_{vel}. Solid lines represent the mean and shading two standard errors from the mean.

3.5 Winter statistics

3.5.1 Daily Distributions

The JLI is widely used and studied due to the trimodal distribution that is obtained when applied to the winter periods, which has been used as evidence of regime behaviour of the EDJ. The distributions of the JLI, $\overline{\phi}$, the JAI and α are shown in Figure 3.9. For the EDJO metrics, days with two EDJOs are accounted for by selecting the day the largest U_{mass}.

Very minor differences are found in the distributions when including the information from all EDJOs or not. For $\overline{\phi}$ and the JLI (Figures 3.9a and b), both distributions show a similar range of values but very different shape and structure. For $\overline{\phi}$, it has a unimodal distribution, with a mean of 45.7° and a standard deviation of 6.7°. For the JLI there is clear multi-modality with peaks at the latitudes of 37°, 45° and 57° defining the southern (S), central (C) and northern modes (N) that has been used in the literature. The lack of multi-modality in $\overline{\phi}$ is an important result as it shows that the trimodal regime structure of the JLI appears to manifest as a result of zonal averaging. To try and identify where the largest differences are occurring, I have calculated $\overline{\phi}-$JLI for the S, C and N regimes of the JLI, shown in Figure 3.9c. For the S regime (JLI $< 40°$) $\overline{\phi}$ tends to be slightly poleward of the JLI with a median difference of 0.74° and standard deviation of 3.7°. Similarly for the C regime ($40° \leq$ JLI $\leq 52°$) the JLI tends to slightly more poleward with a median value of -1.0° and standard deviation of 2.28°. The largest differences occur during the N regime (JLI $> 52°$), where the median value is 5.2∘ and standard deviation of 7.2°.

Looking now at JAI and α (Figures 3.9d and e), both measures capture the tilting of the EDJ of the North Atlantic during winter, with a mean of 7.9° for α and 11.7° for the JAI. The JAI has a higher standard deviation than α with a value of 15.7°, while α has a value of 10.7°. Figure 3.9f shows the distribution of $\alpha -$ JAI divided by days when the JAI characterises a positively and negatively tilted EDJ. The median difference for days when the JAI is positive is $-3.6°$ and 10.9° when the JAI is negative, telling us that the JAI tends to produce larger tilt values on days when the JAI finds a positively tilted EDJ but α is larger on days when the JAI finds a negatively tilted jet. However, there is a large spread in each of the composites with a standard deviation of 13.4° in $\alpha -$ JAI for days when the JAI is positive and 13.7° for days when the JAI is negative, indicating that days with large disagreements are still found for either case. These differences are likely due to the examples shown earlier, where the use of WS_{850} gives no indication of direction, leading to spurious values of tilt when U_{850} gives a direct indication.

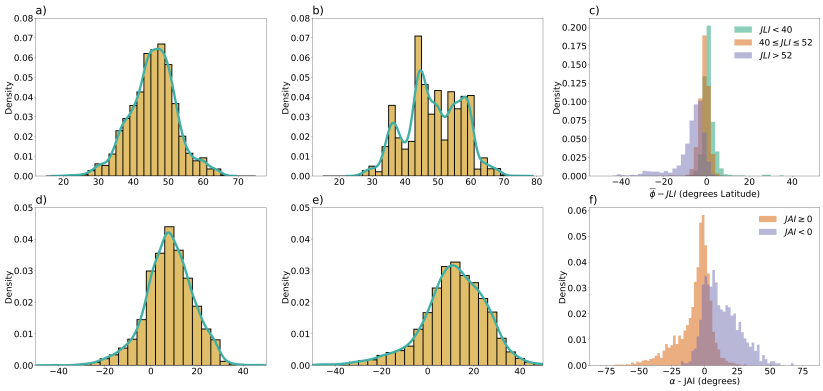

Figure 3.9: Distributions of the daily winter a) $\overline{\phi}$, b) JLI, c) $\overline{\phi}$ - JLI, d) α, e) JAI and f) α - JAI. In c) the histograms are coloured according the JLI regimes defined in the figure label, and in f) $\alpha - JAI$ is coloured according to the sign of the JAI.

3.5.2 Source of differences in the JLI and $\overline{\phi}$

Given the proportion of days in each regime of the regimes (S 12.1% of days, C 48.5% if days and N 37. 4% of days), it means that there is a substantial number of days where the two methods disagree. To try and unravel what might be causing the differences, Figure 3.10 shows a scatter plot of $\overline{\phi}-$JLI plotted against U_{mean} and coloured by α. Each panel shows the scatter plot for each regime in the JLI with the S regime in Figure 3.10a, the C regime in Figure 3.10b, and the N regime in Figure 3.10c. This shows that the sources of the differences during the N regime of the JLI these days are when the EDJ is highly tilted when $\alpha \geq 20°$. This can also be seen in the S and C regimes with days of higher tilt producing a larger difference too. The C regime shows when the two methods tend to agree with each other, which is during days when the EDJ is zonal with values of α close to zero and the strong with large values of U_{mean}. From the example in the Figure 3.4c and d and the evidence shown in Figure 3.10, the tilt of the EDJ appears to be the source of many of the differences between $\overline{\phi}$ and the JLI in the N regime. To confirm this, Figure 3.11 shows composite averages of U_{850} for different positive intervals of α with values of $\overline{\phi}$ and the JLI for those composites plotted as dashed lines. What this shows is that as you increase α the difference in $\overline{\phi}$ and the JLI also increases, with

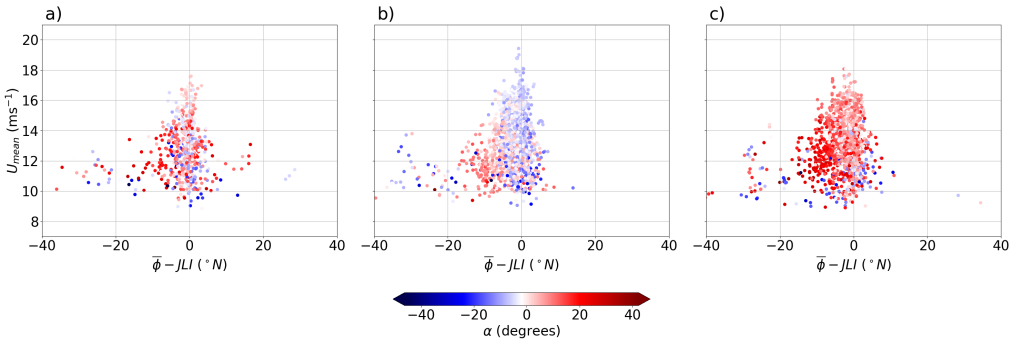

Figure 3.10: Distributions of $\overline{\phi}$ - JLI for each of the regimes of the JLI, with a) S, b) C and c) N. Each point is coloured by the value of α.

the JLI progressively identifying values more north than $\overline{\phi}$ on average. For the most extreme composites, when $\alpha > 20°$ (Figures 3.11c and d), there are two maxima located over Iceland and off the east coast of the United States, which resemble the example shown in Figure 3.4c where the jet is split, suggesting also an influence from these days in causing the differences.

In general, this has highlighted that the differences between the JLI and $\overline{\phi}$ are caused by the tilting of the EDJ, which leads the JLI to define more EDJ in the N regime.

3.5.3 Relationship between moments metrics

I will now discuss the relationships between the new moments metrics and the different picture that they present. Firstly, Figure 3.12 shows the spatial distribution of the centres of mass $(\overline{\lambda}, \overline{\phi})$, for all EDJOs (Figure 3.12a) and for the EDJOs the largest U_{mass} (Figure 3.12b). Looking at Figure 3.12a, the kernel density estimate (KDE) finds a trimodal structure, with a high density peak in the centre of the North Atlantic and two peaks of lower density north-east of the centre over Iceland and south-west of the centre. These weaker peaks coincide with days of two EDJOs (represented as the blue points), indicating that they are the main regions for the split jet occurrence. These types of days are rare only occurring on 4. 8% of days in the data, with single EDJO days the highest at 93.5% and zero EDJO days the lowest at 1.7%. However, when only considering the EDJO of the largest U_{mass}, the peak over Iceland collapses and the distribution becomes

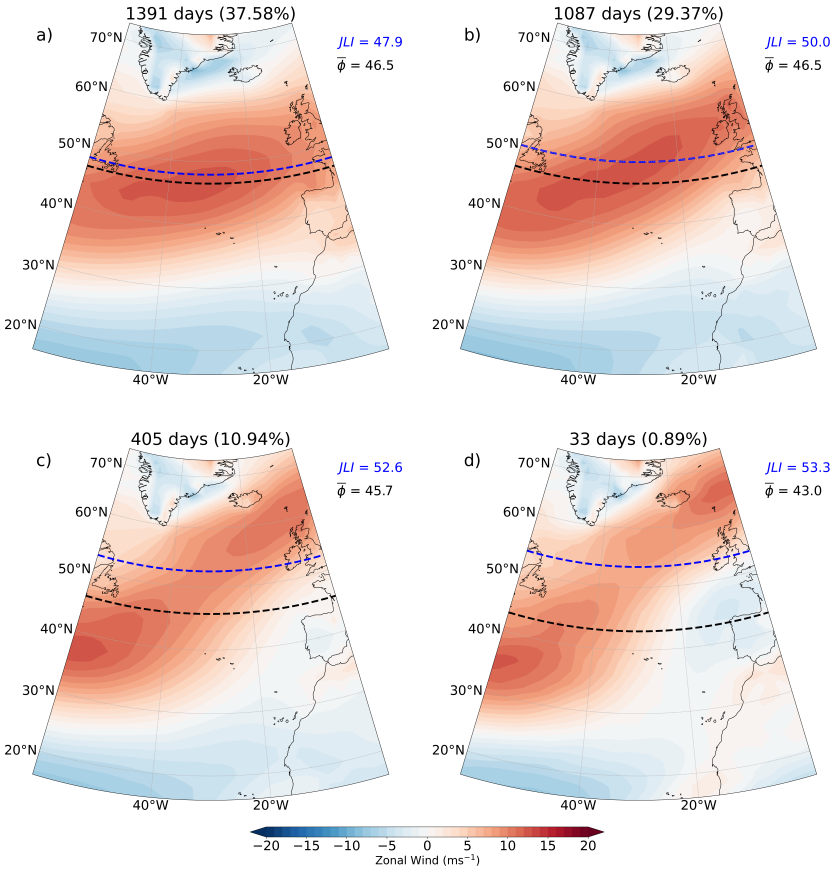

Figure 3.11: Composites of U_{850} for intervals of α where a) $0 \leq \alpha \leq 10$, b) $10 \leq \alpha < 20$, c) $20 \leq \alpha < 30$ and d) $\alpha \geq 30$. Horizontal dashed represent the mean value of $\overline{\phi}$ (black) and the JLI (blue) for each composite with there respective values given in the top right of each panel.

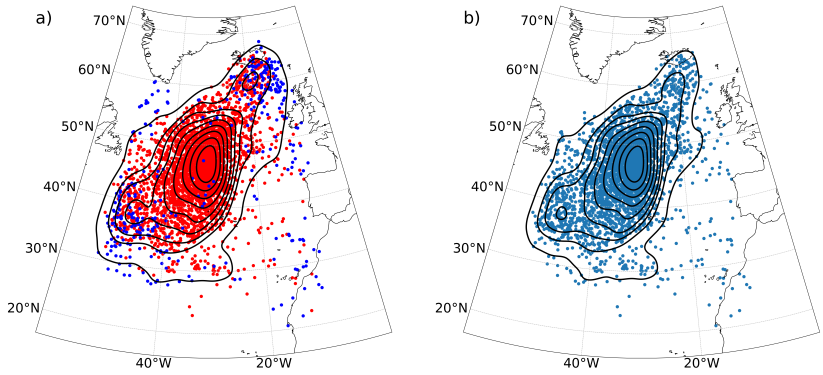

Figure 3.12: Distributions of the EDJO centre-of-mass $(\overline{\lambda}, \overline{\phi})$ for a) all EDJOs and b) the EDJO with the largest U_{mass}. The colours in a) indicate whether a given day is labelled with one (red) or two (blue) EDJOs. The black contours show the two-dimensional kernel density estimate of the distribution.

more bimodal with the central and south-west peak being retained.

It is interesting to again consider how this distribution relates to the regimes defined by the JLI and if it can reveal further differences between the two approaches. Figure 3.13 shows the separation of the centres of mass into S (Figure 3.13 a), C (Figure 3.13 b), and N (Figure 3.13 c), which are defined in the same way as in the previous sections. This reveals that, for the S and C regimes, the centres of mass largely lie within the defined bounds of the JLI. This is something I would expect given the agreement between the measures of $\overline{\phi}$ and the JLI in those regimes in the previous sections. As expected, this relationship breaks down with many centres of mass lying below the cut-off point of the N regime. The N regime also has the highest number of days with two EDJOs defined with 2.8% of days, whereas S and C have 1.4% and 0.6%, respectively. The structure of the centre-of-mass distribution in the N regime looks to tilt across the basin, unlike the S and C distributions which look to be more zonal. This is validated when looking at the average of α in each of the regimes, the N regime having the highest value of 9.9° and the S and C with values of 0.7° and 1.4°, respectively.

In the last part of this section, I show how different characteristics of the

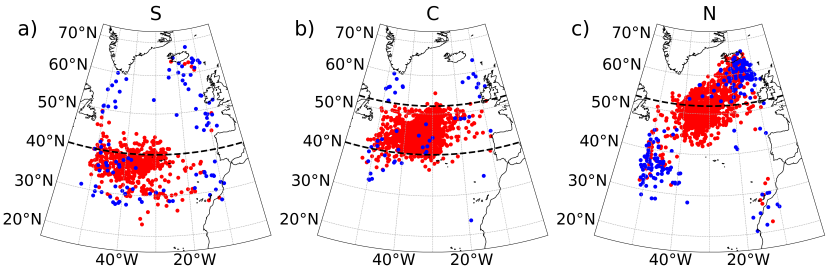

Figure 3.13: Distributions of the EDJO centres of mass, partitioned into the S a), C b) and N c) regimes of the JLI. The colours of the points represent the days defined by one (red) or two (blue) EDJOs. The dashed horizontal lines define the cut-offs of the regimes of the JLI.

EDJ measured by the EDJOs are related to each other. Figure 3.14 shows scatter plots of $\overline{\phi}$ against α (Figure 3.14a), $\overline{\phi}$ against U_{mean} (Figure 3.14b) and α against U_{mean} (Figure 3.14c). From Figures 3.14a and b, there is a weakly linear pattern between $\overline{\phi}$ with α or U_{mean}. Performing a linear regression on these data, this further confirms this with a correlation coefficient (ρ) of 0.2 and 0.1 for $\overline{\phi}$ against α and $\overline{\phi}$ against U_{mean}. Looking across the distributions, where moving from lower values of α and U_{mean} to higher values, there is decreasing variability in $\overline{\phi}$ with values of $\overline{\phi}$ close to their mean at higher values. In Figure 3.14c, There is again a little to no linear relationship with $\rho = -0.05$, but there is a nonlinear relationship between α and U_{mean}, where the lower values of U_{mean} show a higher variability in α, but as U_{mean} increases, the variability decreases and α tends towards zero. This shows that the stronger an EDJ the more zonal it tends to be and the weaker it tends to display positive tilt, but there is also a chance for negative tilts to occur.

Another measure of the strength that can be used is U_{mass}, which was defined in the moments section. This is essentially an area weighted speed; hence it will capture the size and the strength of the EDJO. Figure 3.15, shows the scatter plots of $\overline{\phi}$ against U_{mass} (Figure 3.15a), U_{mass} against α (Figure 3.15b) and U_{mass} against U_{mean} (Figure 3.15c). Here we can see that there are some differences between the relationships compared to U_{mean}. For

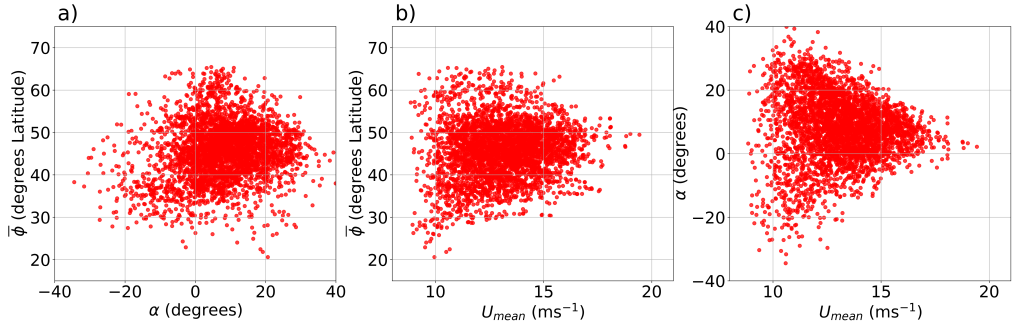

Figure 3.14: Scatter plots of $\overline{\phi}$ vs α a), $\overline{\phi}$ vs U_{mean} b) and α vs U_{mean} c).

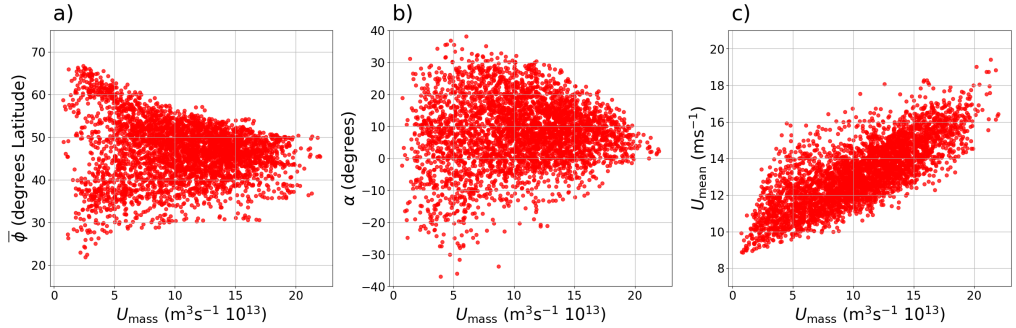

Figure 3.15: Scatter plots of $\overline{\phi}$ vs U_{mass} a), α vs U_{mass} and U_{mean} vs U_{mass}

example, in Figure 3.15a, lower values of U_{mass} have higher variability in $\overline{\phi}$ but, interestingly, you find a small number of points near the centre of $\overline{\phi}$. The latitudes in $\overline{\phi}$ are in agreement with the latitudes of days with two EDJOs, which can be seen in Figures 3.4c and d. There is a negative correlation between U_{mass} and $\overline{\phi}$ with $\rho = -0.12$ where smaller EDJOs are found at more poleward latitudes, so as the EDJ is more equatorward you tend to find a larger and stronger EDJ. This will be influenced by the area weighting in the calculation of U_{mass}, but there is still a range of around $10 - 12°$ in the largest U_{mass}. This also shows that the larger U_{mass} sits around the mean of $\overline{\phi}$ and the variability is much lower, which is not as clear in Figure 3.14b, when using U_{mean}. A similar pattern is found between U_{mass} and α where the largest EDJOs are more zonal and smaller have greater variability in α. Lastly, Figure 3.15c shows that there is a linear relationship with $\rho = 0.77$ between U_{mean} and U_{mass} but there is a spread in U_{mean} in U_{mass}. So, you may find that U_{mean} can give large values but for smaller EDJOs.

In this section, I have shown that the trimodal distribution of the JLI is an artefact of zonal averaging. This is first highlighted by the unimodal distribution of $\overline{\phi}$ (Figure 3.9b) and the distribution of $\overline{\phi}$ − JLI (Figure 3.9c), showing that on average the most differences occur in the N regime of the JLI. To define what causes this relationship, Figures 3.10 and 3.11 showed that the JLI has a tendency to define the EDJ in the N state when the EDJ is tilted. This is also seen in the spatial distribution of the centres of mass (Figure 3.12 where the JLI N regime (Figure 3.13c) is a source of EDJs with large tilt days and split jet days.

3.6 Relationship of EDJOs and Large-Scale patterns of North Atlantic variability

Having explored how the different metrics relate to each other and their differences, I will now look at how they are related to the two leading modes of variability in the North Atlantic. Those being the North Atlantic Oscillation (NAO) and the East Atlantic Pattern (EA). To define NAO and EA, I use station-based indices (Baker et al., 2018; McKenna and Maycock, 2021) using a field of standardised and deseasonalised mean sea level pressure (MSLP). For the NAO, I take the difference between an area-averaged box over the Azores (36° N, 5.3°) W and Iceland (65° N 22.8°W). Then for the EA I use the anomaly in the MSLP at the point closest to 52° N, 27.5°W. Figure 3.16 shows the spatial pattern of the averaged MSLP anomalies (DJF mean removed) of the NAO (Figures 3.16a and b) and the EA (Figures 3.16c and d), where each phase is defined as the positive (+) or negative (-) values of the respective index.

To understand how the EDJ metrics are related to NAO and EA, I performed grid point linear regressions of the EDJ metrics on the MSLP field. Figure 3.17 shows the regression results for $\overline{\phi}$ (Figure 3.17a), U_{mean} (Figure 3.17b), α (Figure 3.17c), $\overline{\lambda}$ (Figure 3.17d) and U_{mass} (Figure 3.17e). Similarly, Figure 3.17 shows the same, but for the JLI (Figure 3.18a), JLI_{vel} (Figure 3.18b), and the JAI (Figure 3.18c).

For the position of the EDJ, $\overline{\phi}$ and the JLI produce a spatial correlation

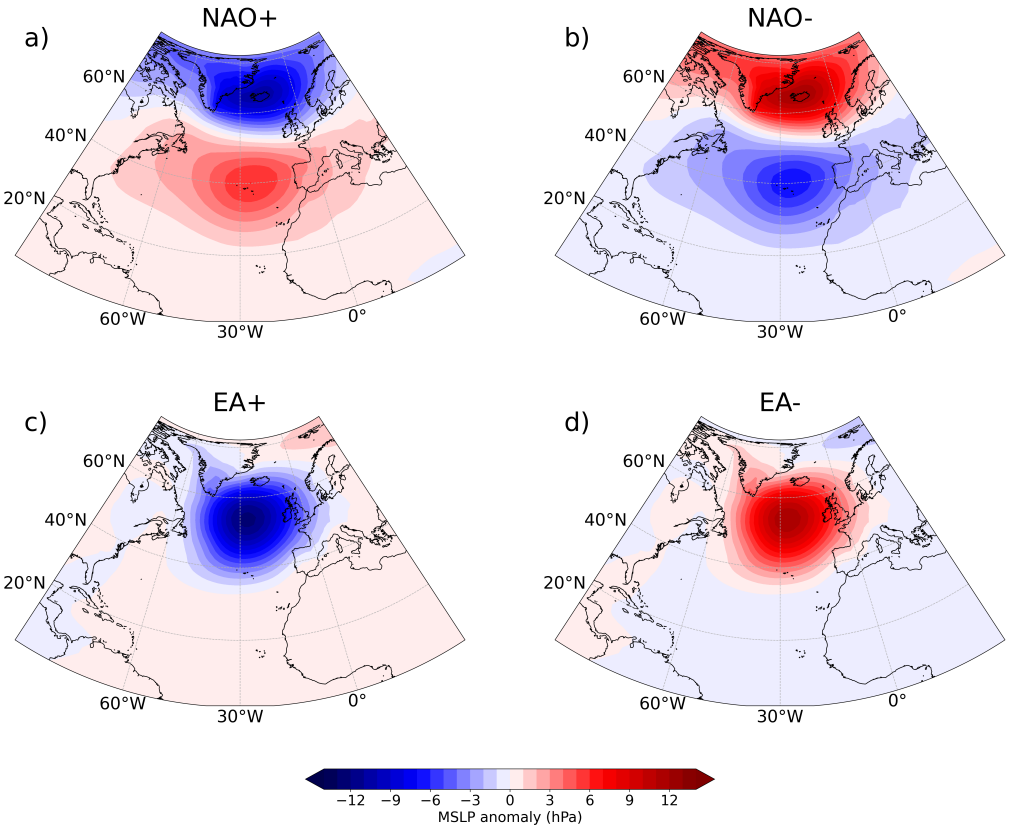

Figure 3.16: Mean Sea Level Pressure (MSLP) anomaly composites (in hPa) for different phases of the North Atlantic Oscillation (NAO) and East Atlantic pattern (EA). Panels (a) and (b) represent positive (NAO+) and negative (NAO-) phases of the NAO, while panels (c) and (d) represent positive (EA+) and negative (EA-) phases of the EA.

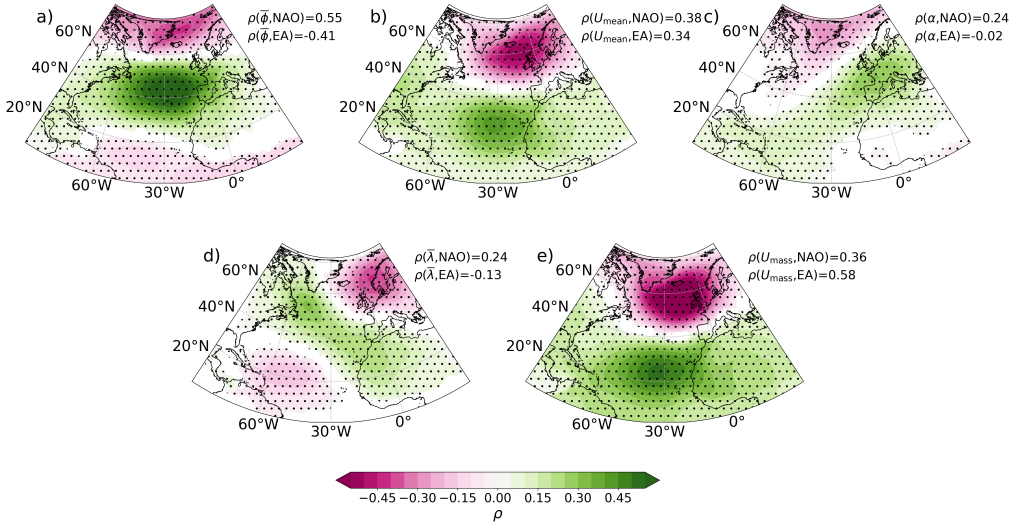

Figure 3.17: Gridpoint correlations (ρ) of linear regressions of $\overline{\phi}$ a), U_{mean} b), α c), $\overline{\lambda}$ d), U_{mass} e) against the MSLP for the winter (December-February). Stippling denotes statistically significant correlations at the 95% confidence level. The top right of each denotes the correlation that each metric has with the NAO and EA.

pattern that is in good agreement with the MSLP anomaly of the NAO (Figures 3.16a and b). Hence, NAO+ coincides with the poleward shift of the EDJ and NAO- an equatorward shift. This is better captured in $\overline{\phi}$ than in the JLI, with a higher correlation in $\overline{\phi}$ ($\rho = 0.55$) with the NAO than in the JLI ($\rho = 0.47$). The EA has the opposite effect on position than the NAO, as evidenced by the negative correlation with both $\overline{\phi}$ and the JLI, although there is a slightly stronger negative correlation between the EA and the JLI ($\rho = -0.44$) than with $\overline{\phi}$ ($\rho = -0.41$).

The EDJ strength can be measured by U_{mean}, JLI_{vel} or U_{mass} and each of them has indistinguishable maps of spatial correlations, which are all similar to the EA pattern. For U_{mean} and JLI_{vel}, each show moderate correlations with NAO and EA, with JLI_{vel} having a stronger correlation with both NAO and EA than U_{mean} ($\rho(\text{JLI}_{\text{vel}},\text{NAO}) = 0.42$,$\rho(\text{JLI}_{\text{vel}},\text{EA}) = 0.38$ vs. $\rho(U_{\text{mean}},\text{NAO}) = 0.38$ $\rho(U_{\text{mean}},\text{EA}) = 0.34$). This suggests that both NAO and EA have a similar influence on the strength of the EDJ, with the strongest EDJs occurring during the positive phases of the two, because of changes in the pressure gradient between the subtropical high and the polar low. However, looking at U_{mass}, the correlation with the

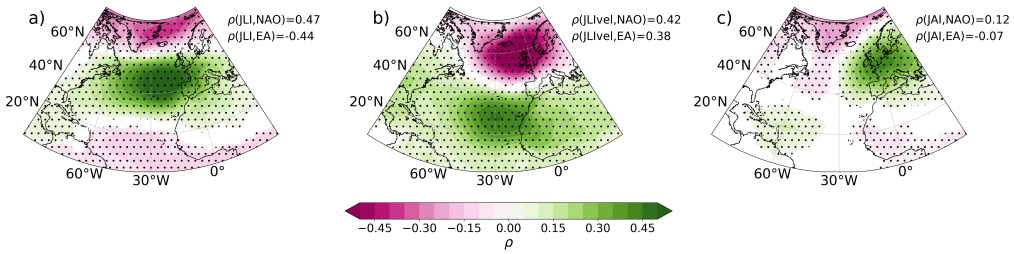

Figure 3.18: Same as Figure 3.18, but for the JLI a), JLI_{vel} b) and JAI c).

NAO is similar to that of U_{mean}, but slightly lower than that of JLI_{vel} ($\rho(U_{\text{mass}}$,NAO) = 0.36), but much higher than both for EA ($\rho(U_{\text{mass}}, EA)$ = 0.58). This indicates that the EA has considerable influence not only on the strength but also on the size of the EDJ, which is closely related to the pulsing variability of the EDJ.

Now, looking at the tilt of the EDJ, the JAI and α differ in their spatial correlations, both showing weaker relationships with the NAO and EA than the latitude and the strength. For the JAI, the correlations with the NAO and EA are weak (ρ(JAI,NAO)=0.12 and ρ(JAI,EA) = -0.07), but for α there is a slightly stronger relationship with the NAO but a negligible relationship with the EA ($\rho(\alpha$,NAO)=0.26 and $\rho(\alpha$,EA)=-0.02). Hence, α tells us that during the NAO+ phases the EDJ tends to tilt and flow over Europe. Lastly, the centre of mass in longitude, $\overline{\lambda}$, which shows a weakly positive correlation with the NAO ($\rho(\overline{\lambda}$,NAO) =0.24) and negative one with the EA ($\rho(\overline{\lambda}$,EA)=-0.13). This means that the EDJ will shift eastward with NAO+ and westward with NAO-, which is reversed for each phase of the EA.

3.6.1 NAO/EA phase space

Looking at the relationships discussed in the previous section in more detail is to consider the NAO/EA phase space, where the joint relationship can be understood. Figure 3.19 shows the NAO/EA phase space for all days coloured by different EDJ metrics. Looking at $\overline{\phi}$ and the JLI (Figures 3.19a and b), each measure captures the result of Woollings et al. (2010), where the EDJ latitude increases, moving clockwise around the phase space shown by the mean. The largest discontinuity in latitude occurs in the

NAO-/EA- part of the phase space for the JLI and $\overline{\phi}$, which is attributed to the high occurrence and split jets leading to two EDJOs, such as the one seen in Figure 3.4b. From the standard deviation in each quadrant, $\overline{\phi}$ is consistently lower than the JLI, with the highest variability occurring in the NAO+/EA- quadrant for both the JLI and $\overline{\phi}$. There is also a higher variance explained (R^2) for $\overline{\phi}$ than the JLI for all quadrants, each of which indicates that $\overline{\phi}$ is a smoother varying measure.

For tilt, the JAI (Figures 3.19c) has higher variability for all quadrants than α (Figure 3.19 b), by the standard deviation value. Moving through the phase with α, during NAO- there is a tendency for a negative jet tilt and during a tendency for a positive tilt which agrees with the results from the previous section. The JAI shows a similar pattern, but much weaker, due to the higher variability within each of the quadrants. The R^2 is higher in α than the JAI but only for the quadrants associated with NAO+. The quadrants associated with the NAO- have a marginally higher R^2 for the JAI, but are very low for α. There is little relationship with the EA for both α and the JAI.

Lastly, the EDJ strength shows a similar pattern for $\mathrm{U_{mean}}$ (Figure 3.19)e), $\mathrm{JLI_{vel}}$ (Figure 3.19f) and U_{mass} (Figure 3.19g). For all measures, the weakest EDJs are found in the NAO-/EA- quadrant, and the strongest in the NAO+/EA+ quadrant. The R^2 for U_{mean} than $\mathrm{JLI_{vel}}$ is quite similar throughout all quadrants, with both having the lowest R^2 for the NAO+/EA- quadrant. For U_{mass}, R^2 is higher than both U_{mean} and $\mathrm{JLI_{vel}}$ for all quadrants, with the highest R^2 in the NAO-/EA- quadrant. The added information of size with the strength of the EDJO being the difference for this larger R^2.

All of this evidences that the EDJO metrics provide a better measure of variability in the EDJ compared to the others, with $\overline{\phi}$ being the best measure of the EDJ latitude, α for tilt and U_{mass} for strength. The NAO and the EA have a strong influence on the EDJ, with the NAO having a stronger influence on the latitude and tilt, and the EA having a stronger influence on the strength and size.

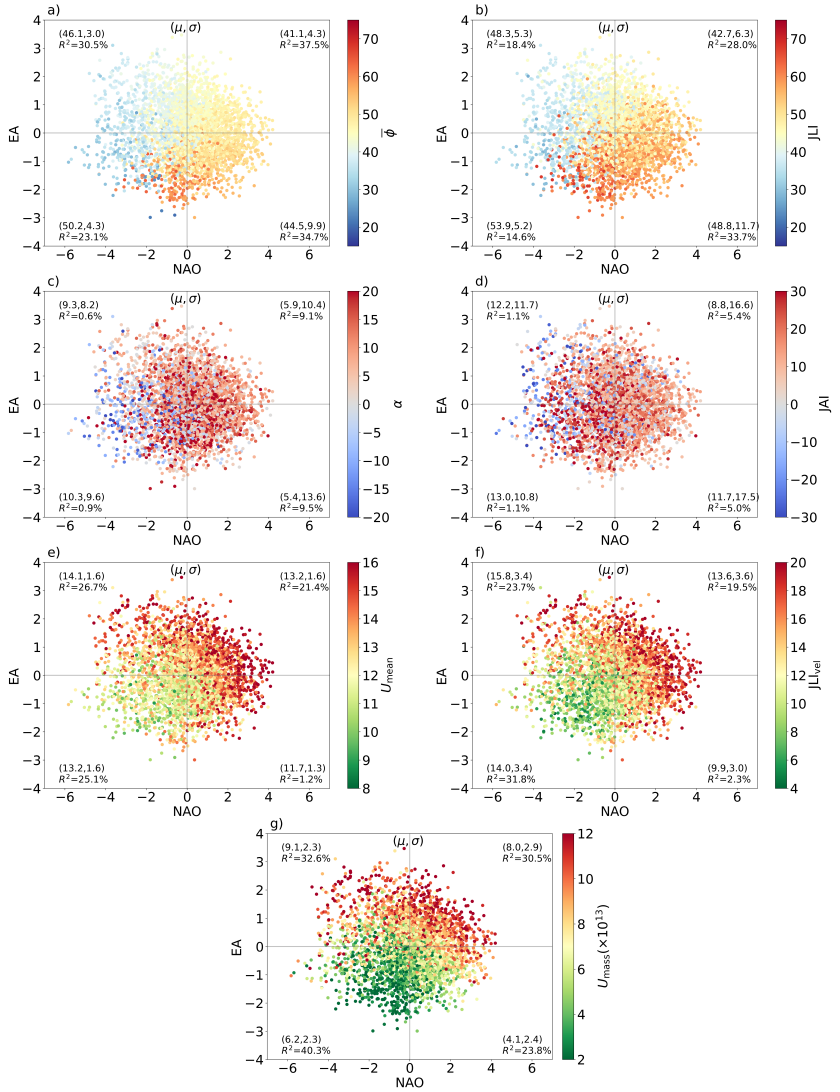

Figure 3.19: Scatter plots of the EA vs NAO for all winter days coloured by $\overline{\phi}$ a), JLI b), α c), JAI d) $\mathrm{JLI}_{\mathrm{vel}}$ e), U_{mean} f) and U_{mass} g) for EDJOs of the largest mass. Note that e) and f) have different scales, and U_{mean} is bounded below by $U^*_{850} = 8\mathrm{ms}^{-1}$. The values of mean μ and standard deviation σ are given for each quadrant in brackets, and the variance explained R^2.

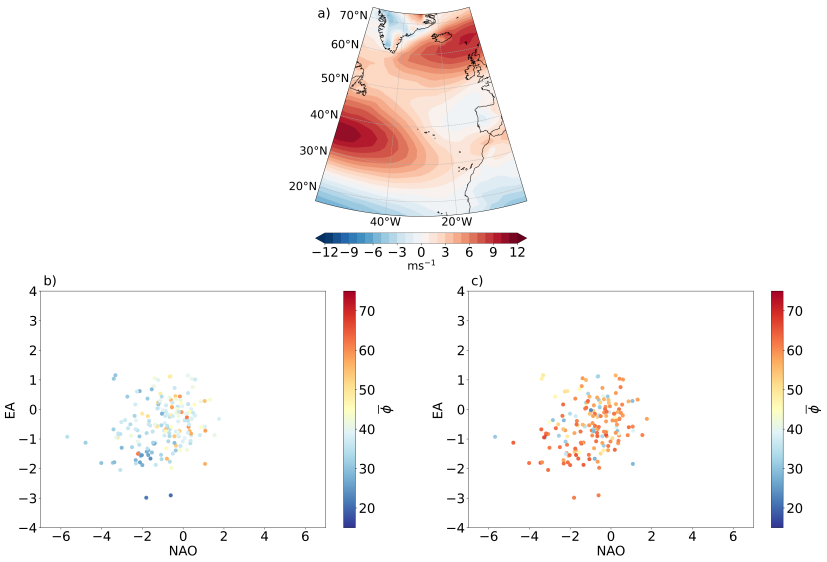

Figure 3.20: (a) Composite U^*_{850} field for winter days with two EDJOs. This represents 4.9% of DJF days. (b,c) Scatterplots of all winter daily EA vs NAO indices coloured by $\overline{\phi}$ for days with two EDJOs. Panel (b) shows the EDJO with the largest U_{mass}, and (c) shows the EDJO with the smaller U_{mass}.

3.6.2 Multiple Object Days

In Figure 3.19, a lot of variability was observed in the NAO-/EA- quadrant of the phase space. Here, I show that this quadrant is largely associated with days of two EDJOs. Figure 3.20a shows the composite U_{850} for days with two EDJOs. Here we can see strong westerlies over the east coast of the USA and a region of weak easterlies near Iceland, with a region of weak easterlies near the Bay of Biscay and to the west of Portugal. This pattern resembles the circulation during Atlantic blocking. Consequently, there is also a link between the occurrence of two EDJO days and the NAO/EA with most days coinciding with NAO-/EA-. The NAO/EA phase space for days with two EDJOs with the EDJO with the largest U_{mass} (Figure 3.20b) and the smaller (Figure 3.20c). In general, on two EDJO days, the EDJO with the largest U_{mass} is found at the lower latitudes south of 40^circN and the smaller EDJO is found north of 50∘N.

3.7 Conclusions and Discussion

In this chapter, I developed and evaluated an algorithm to identify and analyse Eddy-Driven Jet Objects (EDJOs), comparing it with traditional zonal-averaged metrics such as the Jet Latitude Index (JLI) and Jet Angle Index (JAI). The analysis demonstrated that the EDJO-based method, which uses a spatial approach to capture jet features, overcomes several limitations associated with zonal averaging. These include the ability to capture complex jet structures such as split jets, tilted jets, and broad jets, which are often overlooked or mischaracterised by the JLI. Key findings include the following.

1. The EDJO identification method more robustly characterises the jet structure on days where the jet is broad, highly tilted, split or not well defined, as compared to the JLI.

2. The time variability of $\overline{\phi}$ shows fewer large amplitude 'jumps' between consecutive days as compared to JLI. Examination of cases suggests that these jumps in JLI can be spurious resulting from selecting one of several competing maximums and do not reflect meaningful changes in the jet structure. The autocorrelation function of $\overline{\phi}$ shows greater persistence than JLI between days 2-9.

3. The statistics of $\overline{\phi}$ over all winter days do not show a trimodal distribution as seen for the JLI. The distribution has a mean of 45.7° and a skewness of -0.07. The daily differences between $\overline{\phi}$ and the JLI tend to be greater for larger jets and highly tilted jets. When compositing low-level zonal wind for the same range of values, the two measures pick out similar patterns of large-scale circulation.

4. There is a smoother variation of $\overline{\phi}$ and U_{mean} in the NAO/EA phase space. Both $\overline{\phi}$ and U_{mean} also have a higher variance explained by the NAO and EA indices than the JLI and JLI_{vel}.

5. The distribution of jet tilt α is more Gaussian with a mean of 7.9°. Around 20% of the days show a negative tilt.

In conclusion, the EDJO algorithm presents a significant improvement in capturing the dynamics of the North Atlantic EDJ, particularly in terms of

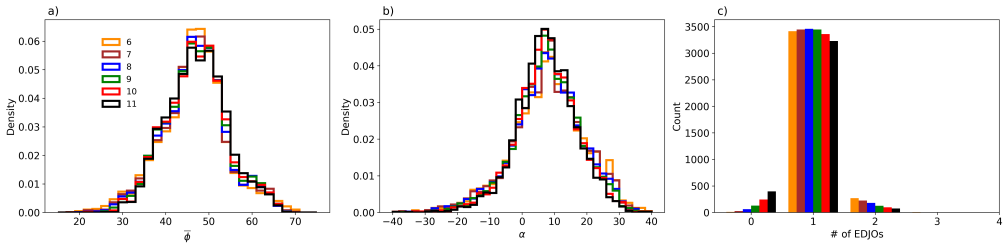

Figure 3.21: Distributions of $\overline{\phi}$ a), α b) and c) the frequency of days with different numbers of EDJOs for a range of U^*_{850} values from $6\,\mathrm{ms}^{-1}$ to $11\,\mathrm{ms}^{-1}$, with colours following the legend in panel (a).

persistence, strength, and structure. Its ability to capture more complex jet configurations, especially in relation to large-scale climate modes, makes it a valuable tool for future research into jet stream variability and its impacts.

Appendix: Robustness of EDJO identification

3.7.1 Choice of U^*_{850}, L^* and L^*_λ

The results in this chapter used $U^*_{850} = 8\,\mathrm{ms}^{-1}$. Here, I compare the results with a range U^*_{850} values. Figure 3.21 shows the distributions of $\overline{\phi}$, α and the number of EDJOs per day for U^*_{850} varying between 6 and $11\,\mathrm{ms}^{-1}$. Both $\overline{\phi}$ and α are largely insensitive to the choice of U^*_{850} (Figures 3.21a and b). There are changes in the median value of U_{mean} (not shown), but this would be expected since U^*_{850} sets the minimum U_{mean}. Finally, the distribution of the number of EDJOs per day shows little differences for U^*_{850} between 6-9 ms^{-1}. Higher values of U^*_{850} lead to a decrease in days with one EDJO and an increase in days with zero, potentially because they no longer meet the length criteria. From these results, we conclude that the EDJO algorithm is largely insensitive to sensible variations in U^*_{850}.

3.7.2 Sensitivity to inclusion of L^* and L^*_λ

The effect of including the L^* and L^*_λ criteria in the algorithm is shown in Figure 3.22, where the distributions of $\overline{\phi}$, EDJO area and number of

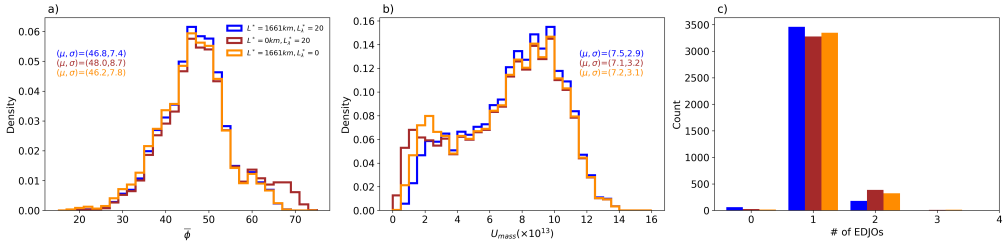

Figure 3.22: Distributions of $\overline{\phi}$ a), Area b) and the frequency of days with different numbers of EDJOs c) with the inclusion of the L^* and L^*_λ checks (blue), just L^*_λ (red) and just L^* (orange).

EDJOs per day are shown. Including only the L^*_λ check results in a higher $\overline{\phi}$ density at northern latitudes, which are smaller EDJOs in area because of Earth's curvature. Including only the L^* check removes the EDJOs at high north latitudes but retains a higher density of small EDJOs that occur on the south flank of the $\overline{\phi}$ distribution. Each of the length checks on their own results in an increase in the frequency of days with two EDJOs, which are typically smaller than on days with a single EDJO. Not until both L^* and L^*_λ are used together do we see a decrease in the occurrence of the smallest EDJOs.

Chapter 4

Predictability of the Eddy-Driven Jet

4.1 Introduction

Accurate prediction of the atmosphere is crucial for forecasting extreme weather events and enabling effective preparation and mitigation strategies. In the North Atlantic region, the winter North Atlantic Oscillation (NAO) is a well-studied phenomenon, known for its significant impact on weather patterns across Europe and North America. Previous studies have demonstrated the existence of predictable skill in the winter NAO, at lead times of approximately 1 to 4 months (Scaife et al., 2014). However, beyond NAO, the variability and predictability the North Atlantic of eddy-driven jet (EDJ) has received less attention, with only a few studies focussing on seasonal (Parker et al., 2019; Strommen, 2020) to decadal predictability (Marcheggiani et al., 2023; Strommen et al., 2023)

The EDJ is a key feature of the atmospheric circulation of the North Atlantic, closely linked to surface weather impacts, including precipitation, temperature, and wind storms. Understanding its variability, dynamics, and predictability is therefore essential for improving seasonal forecasts. Despite this, challenges remain in capturing the full spectrum of EDJ behaviour, including its latitude, strength, tilt, and variability, particularly in the context of seasonal forecast models such as the Met Office GloSea5

(Thornton et al., 2023). These challenges are compounded by the complex interactions between the EDJ and large-scale atmospheric patterns, including the NAO and the East Atlantic pattern (EA).

In this chapter, I explore the representation and predictability of the winter EDJ in GloSea5 using the Eddy-Driven Jet Object (EDJO) approach of Perez et al., 2024 introduced in Chapter 3. This includes an assessment of its biases, variability, and relationships with large-scale teleconnections, as well as an evaluation of its seasonal predictability.

By providing a detailed assessment of the EDJ in GloSea5, this chapter contributes to a greater understanding of the strengths and limitations of the model in simulating the atmospheric variability of the North Atlantic and offers insights into potential avenues for improving seasonal forecasting systems.

4.2 Data and Methods

4.2.1 Model and Observations

The fields used are the daily zonal wind 850hPa (U_{850}) and mean sea level pressure (MSLP) for the extended winter (November-February). The seasonal forecasting model used is GloSea5 (MacLachlan et al., 2014), which has an atmospheric resolution of $0.8° \times 0.5°$ in latitude and longitude with 85 vertical levels, while the ocean model uses the 0.25° grid with 75 vertical levels. Initial conditions for the atmosphere and land surface are taken from daily operational analysis fields, and the ocean is initialized via a 3D-variational data assimilation system that uses observations of temperature, salinity and sea-level anomaly.

I use hindcasts initialised from the 1st of October and ran until 31st March, for the period 1994-2016. Four model systems (12 to 15) with minor differences in model physics have been combined, each with seven ensemble members, giving an ensemble size of 28 members used in this study. I use ERA5 reanalysis as a reference dataset to compare with GloSea5. Data from the 1959-2020 period for ERA5 are also included. The longer period is included to account for any sampling bias in the 1994-2016 period in the

observations. Throughout the chapter, red will be used to represent data from GloSea5, black for data from ERA5 for data in the period 1994 - 2016. All data is available on the Copernicus Climate Data Store.

4.2.2 EDJO identification

The methodology developed from Chapter 3 is applied to the U_{850} field The algorithm parameters used in GloSea5 are the same as those used when analysing ERA5; that is, $U^*_{850} = 8\text{ms}^{-1}$, $L^* = 1661\text{km}$, and $L^*_\lambda = 20°$ also covering the same North Atlantic domain, 15-75°N and 0-60°W. The relative number of EDJOs identified in both ERA5 and GloSea5 is shown in Figure 4.1a, which shows little difference between GloSea5 and ERA5. In slightly more detail, Figure 4.1b shows the percentage difference between ERA5 and GloSea5 for the number of objects identified. This shows that GloSea5 detects slightly more zero ($< 1.7\%$) EDJO days than what is observed in GloSea5 and fewer one and two EDJO days ($< -1\%$). There is also a very small fraction of three EDJO days detected in GloSea5. This could suggest that there is a tendency for weaker winds in GloSea5, due to the higher number of detected zero EDJO days, though the differences are modest.

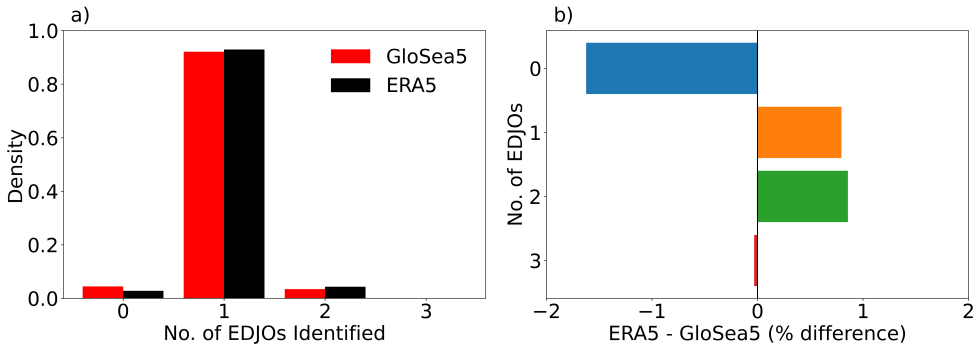

Figure 4.1: The number of EDJOs identified for the forecast period in GloSea5 and ERA5 a) and the perecentage difference in the occurrence of EDJOs b).

4.2.3 Definition of Large-Scale Patterns

North Atlantic Oscillation and the East Atlantic Pattern

The North Atlantic Oscillation (NAO) and the East Atlantic pattern (EA) are calculated using the deseasonalised winter anomalies of MSLP. The deseaonalisation of the data is done by taking the monthly mean (μ) and standard deviation (σ) of the MSLP calculating

$$MSLP' = \frac{MSLP - \mu}{\sigma} \tag{4.1}$$

for the days in the corresponding months. The NAO is defined as the difference between two area-averaged boxes defined over Gibraltar (36°N, 5.3°W) and Iceland (65°N, 22.8°W). The EA pattern is defined at the point 52°N, 27.5°W.

4.3 Assessing Model Differences

To quantify the differences between GloSea5 and ERA5 three metrics are used: bias, root mean square error (RMSE), and Kullback-Leibler divergence (KL). These metrics are defined as follows:

Bias

The bias measures the average difference between the forecast (F) and the observations (O) on the samples N. It is calculated as:

$$\text{Bias} = \frac{1}{N}\sum_{i=1}^{N} F_i - O \tag{4.2}$$

where F_i is the forecast, O is the observed value, and N is the number of ensemble members.

Root Mean Square Error (RMSE)

The RMSE measures the magnitude of errors between the forecast and observations. It gives greater weight to larger errors and is defined as:

$$\mathrm{RMSE} = \sqrt{\frac{1}{N}\sum_{i=1}^{N}(F_i - O)^2}. \tag{4.3}$$

Here, F_i and O_i are the same as above. A lower RMSE indicates better agreement between the forecast and the observations.

Kullback-Leibler (KL) Divergence

The KL divergence quantifies the difference between two probability distributions, observations, and forecasts. For discrete distributions, it is calculated as:

$$D_{\mathrm{KL}}(O \parallel F) = \sum_i O_i \log\left(\frac{O_i}{F_i}\right), \tag{4.4}$$

where O_i and F_i represent the probabilities of the i-th bin in the distributions of observations and forecasts, respectively. The lower the value of D_{KL}, the better the model represents the given set of observations.

4.4 Representation of EDJOs in GloSea5

4.4.1 Daily distributions

Figure 4.2 shows the distributions of daily winter values from 1993/94 to 2015/16 for $\overline{\phi}$, U_{mean}, α, and U_{mass}. The vertical solid lines represent the mean values for each variable and the dashed lines mark the two standard errors from the model mean. Model biases are reported as the mean difference from ERA5 with two standard errors, providing a measure of uncertainty. A table of summary statistics is shown in Table 4.1.

The mean values of ERA5 for all variables lie within the 95% confidence interval of GloSea5, indicating that there are no significant climatological biases in the model.

Figure 4.3 illustrates the relationships between the daily EDJO diagnos-

Variable	GloSea5 Mean	ERA5 Mean	GloSea5 Std	ERA5 Std
$\overline{\phi}$ (°N)	48.1±2.5	46.8	6.6± 2.4	7.1
U_{mean} (ms^{-1})	12.7±0.6	13.0	1.6±0.6	1.7
α (°)	6.4±3.8	6.8	10.1±3.64	10.6
U_{mass} (m^3s^{-1})	8.8±1.5	9.9	3.9±1.4	4.3

Table 4.1: Table of summary statistics for GloSea5 and ERA5 from the 1994-2016 period. GloSea5 values include the value of two standard errors.

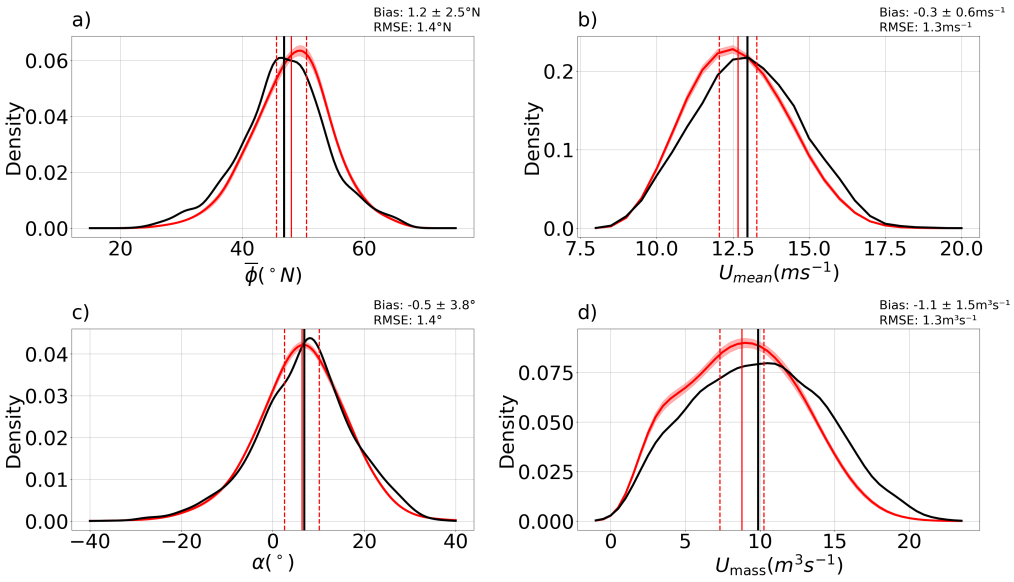

Figure 4.2: Distributions of $\overline{\phi}$ a), U_{mean} b), α c) and U_{mass} d) for GloSea5 (red) and ERA5 (black) for November-February between 1994-2016. Red shading represents two standard errors from the ensemble mean in GloSea5. The black vertical line is the mean for ERA5 and the red line shows the ensemble mean for GloSea5. Values of the mean and the standard deviation are given in the top left of each panel and the bias (with two standard errors) and RMSE in the top right.

tics as two-dimensional distributions. The contours of U_{mean} vs. $\overline{\phi}$ (Figure 4.3a), α vs. $\overline{\phi}$ (Figure 4.3b) and U_{mean} vs. α (Figure 4.3c) are shown, with GloSea5 in red and ERA5 in black. In each panel, the Kullback-Leibler (KL) divergence, displayed in the top right, quantifies the difference between the two distributions, with lower values indicating closer agreement. For U_{mean} versus $\overline{\phi}$ (Figure 4.3a), the KL divergence is 0.08, indicating strong agreement between GloSea5 and ERA5, where there is no clear relationship between latitude and strength, based on the low linear correlation. Similarly, for α versus $\overline{\phi}$ (Figure 4.3b), the KL divergence is the lowest among all panels (0.06), highlighting minimal differences between the two distributions.

In contrast, a distinct pattern is observed between U_{mean} and α (Figure 4.3c), where higher values of U_{mean} are associated with a smaller spread in values of α, suggesting an EDJ that is generally less variable and more zonal. The KL divergence of 0.07 indicates that GloSea5 captures this behaviour well. For U_{mean}, the relationships with $\overline{\phi}$ (Figure 4.3d) and with α (Figure 4.3e) show slightly higher KL divergence values of 0.12 and 0.11, respectively. These higher values suggest that, while GloSea5 reproduces the overall structure of these relationships, there are noticeable differences in the distributions compared to ERA5. This difference is related to the larger values of U_{mass} (Figures 4.3 d and e), which GloSea5 tends to underestimate. In general, the KL divergence values show that GloSea5 more accurately represents the relationships involving $\overline{\phi}$, U_{mean}, and α, while greater discrepancies arise in the relationships involving U_{mass}.

4.4.2 Time varying statistics

To understand how the EDJ evolves during the NDJF period, Figure 4.4, shows the climatological timeseries of the daily EDJO variables in ERA5 and GloSea5. The evolution of $\overline{\phi}$ (Figure 4.4a) in ERA5 shows an equatorward trend from early November to late December, where $\overline{\phi}$ sits at a mean value of 44°N until early January, when it moves poleward to around its mean position. In GloSea5, the early winter equatorward trend is somewhat captured, but the amplitude of the equatorward movement lies outside the spread of GloSea5 during the late December and early January period.

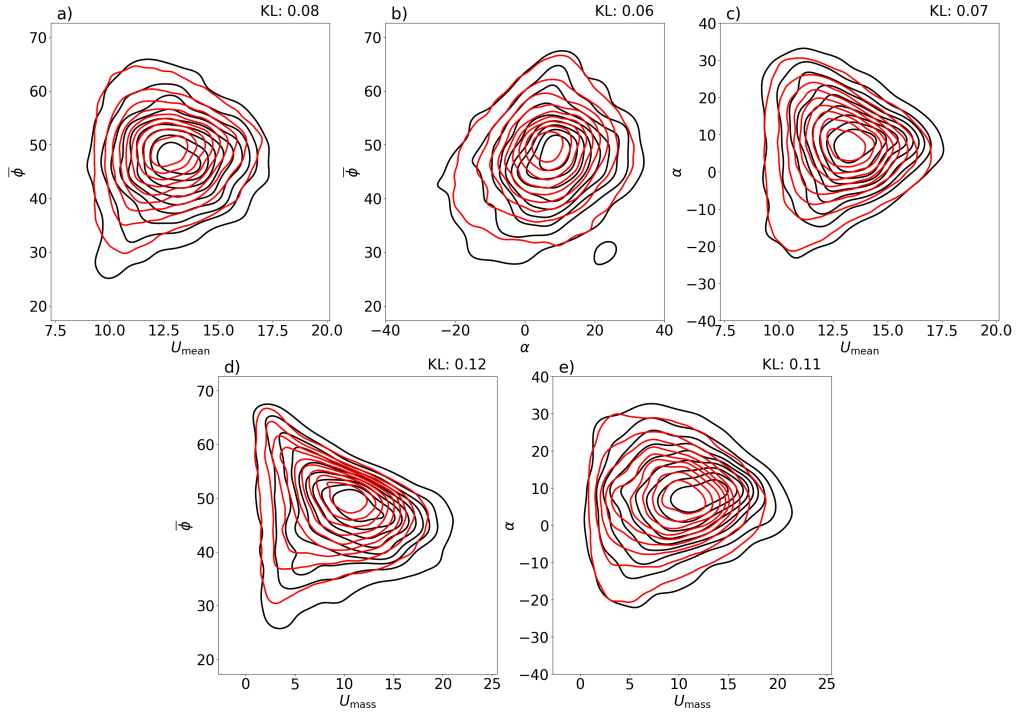

Figure 4.3: Two-Dimensional distributions of $\overline{\phi}(^{\circ}\mathrm{N})$ against $U_{\mathrm{mean}}(ms^{-1})$ a), $\overline{\phi}(^{\circ}\mathrm{N})$ against $\alpha(^{\circ})$ b), $\alpha(^{\circ})$ against $U_{\mathrm{mean}}(ms^{-1})$ c), $\overline{\phi}(^{\circ}\mathrm{N})$ against $U_{\mathrm{mass}}(\mathrm{m}^3\mathrm{s}^{-1})$ d) and $\alpha(^{\circ})$ against $U_{\mathrm{mass}}(\mathrm{m}^3\mathrm{s}^{-1})$ for all members of GloSea5 (red) and ERA5 (black) for NDJF between 1994-2016.

There is a slight poleward trend in the EDJ in GloSea5 starting in January and extending into February. For U_{mean} (Figure 4.4b), the trend in ERA5 shows a general strengthening of EDJ throughout November and December and a peak in early January, after which it begins to weaken. This is well captured in GloSea5 with a similar trend in the ensemble mean. The other measure of the EDJ strength U_{mass} shows a similar trend in both ERA and GloSea5; however, the largest amplitude U_{mass} lies outside the spread of GloSea5. Lastly, α (Figure 4.4c), the overall trend increases throughout the November-February period, which is well captured by GloSea5, with ERA5 values well within the model spread of GloSea5.

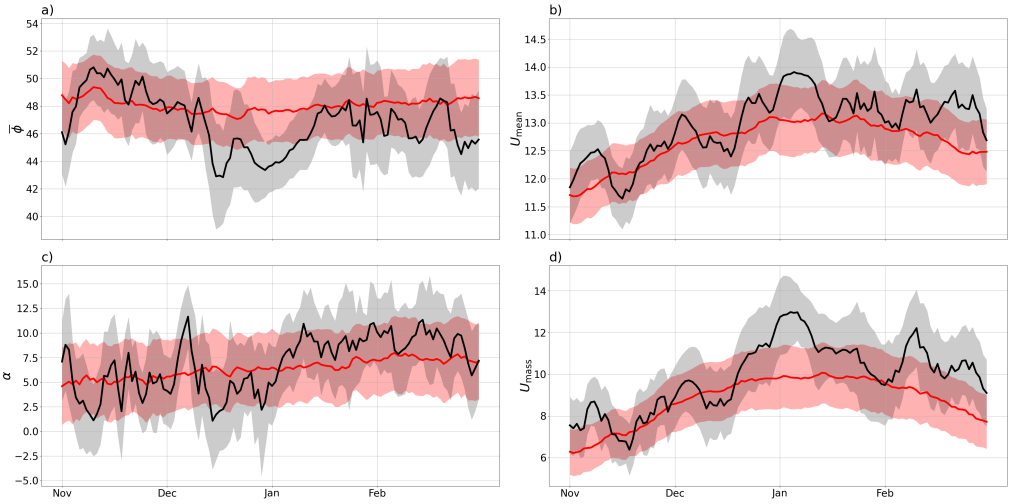

Figure 4.4: Averaged winter evolution of $\overline{\phi}(^{\circ}\text{N})$ a), $U_{\text{mean}}(ms^{-1})$ b), $\alpha(^{\circ})$ c) and $U_{\text{mass}}(\text{m}^3\text{s}^{-1})$ d) for ERA5 (black) and GloSea5 (red). The solid lines are the mean value and the shading represents two standard errors from the mean.

To further understand the time variability, I compute the autocorrelation function (ACF) out to a 15-day lag. I remove the winter mean within each NDJF winter and ensemble member to remove any winter mean offset. For each winter, I then calculate the lag-k autocorrelation ($k = 1..15$) and average the individual ACF estimates over all winters and the 28 ensemble members. This yields the mean model ACF at each lag. The standard error at each lag is then calculated in a similar manner to the mean.

The ACF in Figure 4.4 shows that the mean autcorrelation in GloSea5 is consistently lower in each diagnostic compared to ERA5. In ERA5, the

ACF of $\overline{\phi}$ and α (Figures 4.4 a and c) lies on the edge of the spread of the GloSea5 members, while U_{mean} (Figure 4.4b) falls within the spread. Interestingly, the ACF for U_{mass} (Figure 4.4d) shows that the persistence is too low in GloSea5. This pattern is not unique to GloSea5, as other studies have also indicated a low persistence of the EDJ position in IFS (Strommen, 2020). Each diagnostic in GloSea5 exhibits the same e-folding time as ERA5, with lag dropping below the dashed line at consistent values in all plots. If too low a persistence of the EDJ occurs, it could potentially lead to issues with pinpointing surface impacts and their duration. The lower persistence in $\overline{\phi}$ is likely due to the tendency of GloSea5 to produce EDJs that are weaker than in ERA5 U_{mean} and U_{mass} (Figures 4.2 b and d), therefore, weaker jets tend to show greater variability in their position (Figure 4.3a). The low persistence in the IFS model was proposed to be caused by a poor representation of weather regimes (Strommen, 2020) Other potential sources could include the weak response of the EDJ to remote drivers through eddy feedback (Hardiman et al., 2022).

The ACF in Figure 4.4 confirm that the amplitude of the mean autocorrelation in GloSea5 is systematically lower than in ERA5 for each diagnostic. For $\overline{\phi}$ and α (Figures 4.5 a and c), the ERA5 curve sits on the upper edge of the GloSea5 ensemble spread, whereas for U_{mean} (Figure 4.5b) it lies well within the model spread. The reduced persistence could impact the duration and intensity of different surface impacts. The weaker mean jets in GloSea5 (Figure 4.2 b and d), which are associated with greater positional variability (Figure 4.3a), may partly explain the offset, while additional contributions may arise from the weak response to remote drivers in the North Atlantic due to weak eddy feedback (Hardiman et al., 2022).

4.5 North Atlantic Variability and Predictability

This section explores the relationship between the NAO and EA, in ERA5 and GloSea5. The distributions of the daily NAO and EA indices for GloSea5 and ERA5 are shown in Figure 4.6 with summary statistics of each in the top left of each panel. From Figure 4.6a, the NAO is well captured in

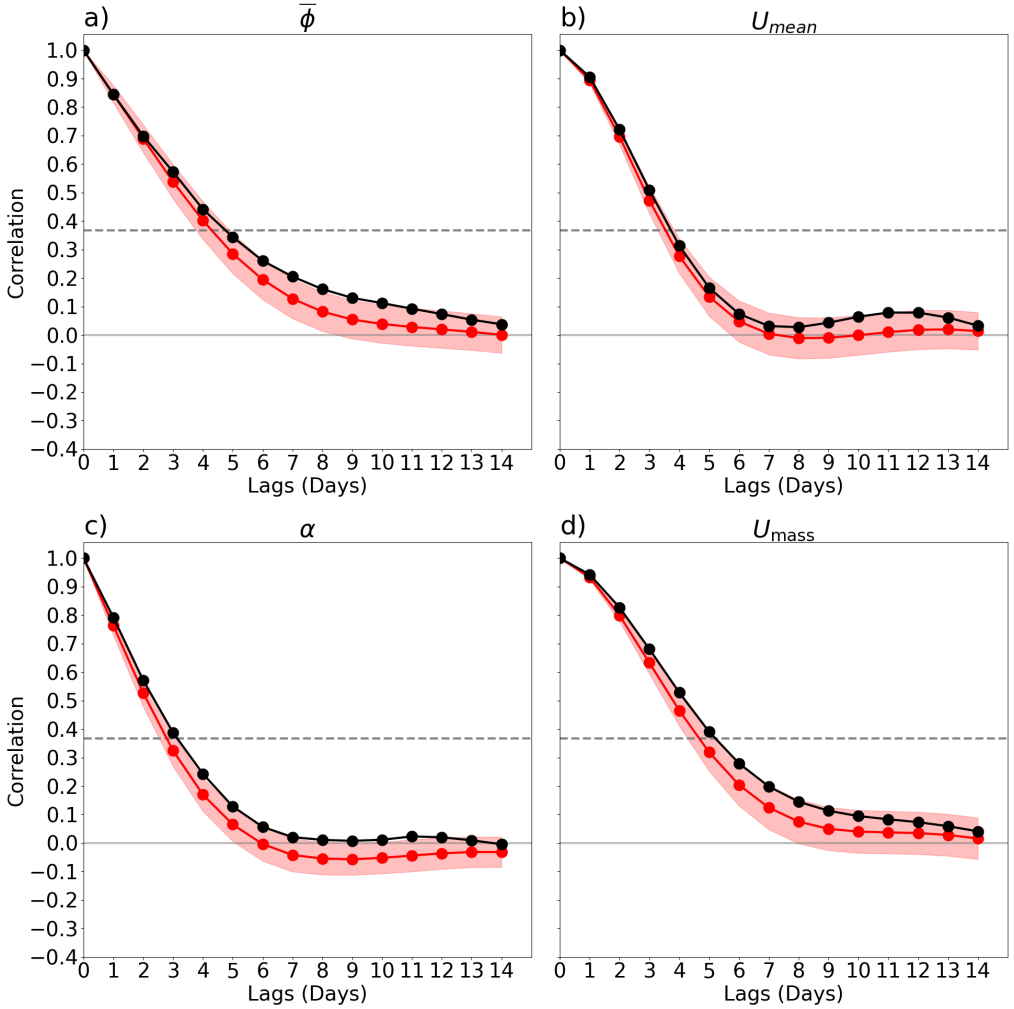

Figure 4.5: Autocorrelation functions of $\overline{\phi}$ a), U_{mean} b), α c) and U_{mass} d) for ERA5 (black) and GloSea5 (red). The solid read line represents the ensemble mean and the red shading represents the two standard errors from the mean at each lag.

GloSea5, with the ERA5 distribution within the spread of GloSea5. There are some differences between the EA distributions (Figure 4.6b), where the number of positive EA events occurs is higher than in ERA5. Further, from the values of the statistics it can be seen that each of the statistics for the NAO match up well with GloSea5, but there are some differences seen in the variance and the kurtosis in the EA pattern.

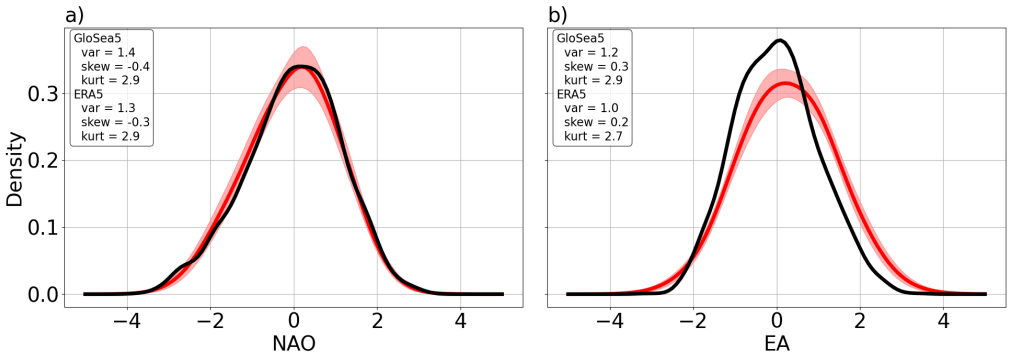

Figure 4.6: Distributions of the NAO (a) and the EA (b) indices for GloSea5 (red) and ERA5 (black).

As shown in Section 3.6, there is a link between the daily NAO and the EA pattern and the various EDJO diagnostics. To test how well GloSea5 reproduces the observed links between the daily NAO and EA indices and each EDJO diagnostic, I apply bootstrapping to each NDJF winter (with a length of 121 days) from a single GloSea5 ensemble member which is treated as one resampling block. I then sample with replacement 10,000 winters to assemble a time series that is 2766 days long, matching the length of the hindcast period. For each replicate, I compute the Pearson correlation between that winters NAO (or EA) index with the respective EDJO diagnostic. This procedure preserves interannual variability across ensemble members, yielding a distribution of correlation coefficients against which the single ERA5 correlation can be used to assess GloSea5. If the correlation in ERA5 falls outside the 95% confidence interval of the model, I conclude that GloSea5 does not capture the relationship.

For $\overline{\phi}$ (Figures 4.7 a and b), GloSea5 reproduces both the sign and the order of magnitude of the observed correlations. In the NAO (Figure4.7a) the ERA5 correlation lies outside the upper tail of the model distribution and outside the 95% confidence interval, showing that the model struggles

to capture the positive NAO-latitude coupling with a too weak relationship between NAO and $\overline{\phi}$. In the EA (Figure4.7b) the relationship is negative; but the ERA5 correlation is outside the model range. Hence, GloSea5 simulates the correct negative EA-$\overline{\phi}$ relationship, yet the coupling between them is too strong (too negative) compared to ERA5.

For U_{mean} (Figures 4.7 c and d), GloSea5 again reproduces the observed sign of the correlations. In the NAO panel (Fig. 4.7 c), the ERA5 correlation lies on the lower edge of the model's 95% bootstrap envelope, indicating that the model captures the positive NAO–U_{mean} link but is stronger than observations. Looking at the EA pattern (Fig. 4.7d) the ERA5 correlation sits outside the confidence interval, showing that GloSea5 underestimates the strength of the influence of the EA pattern on U_{mean}.

Examining α (Figures 4.7e and f), GloSea5 captures the relationship for both the EA and NAO. In NAO (Figure 4.7e), the ERA5 correlation lies just above the upper edge of the CI, indicating that the model tends to underestimate the strength of the NAO-α relationship. Looking at the EA pattern (Figure 4.7f), the relationship is captured well, the ERA5 correlation being close to the mean correlation in GloSea5.

Turning to U_{mass} (Figures 4.7g and h), again GloSea5 correctly captures the sign of the correlation for both the NAO and the EA pattern. Looking at the NAO (Figure 4.7g), the ERA5 correlation falls within the confidence interval but toward the left tail of the distribution. This implies that GloSea5 tends to overestimate the strength of the relationship between NAO and U_{mass}. Then for the EA pattern (Figure 4.7h) the ERA5 correlation lies outside the upper edge of the GloSea5 confidence interval. Hence, the relationship between the EA pattern and U_{mass} is underestimated.

Across the four EDJO diagnostics, the NAO correlations lie within or near the edge of the 95% confidence interval, implying only second-order amplitude errors: the $\overline{\phi}$ and α responses are too weak, whereas the U_{mean} and U_{mass} responses are too strong. In contrast, three of the four EA correlations fall outside the 95% confidence interval. For the EA pattern, GloSea5 drives $\overline{\phi}$ too far equatorward (excessively negative correlation) and damps the influence of EA on both U_{mean} and U_{mass}; only the EA–α correlation is

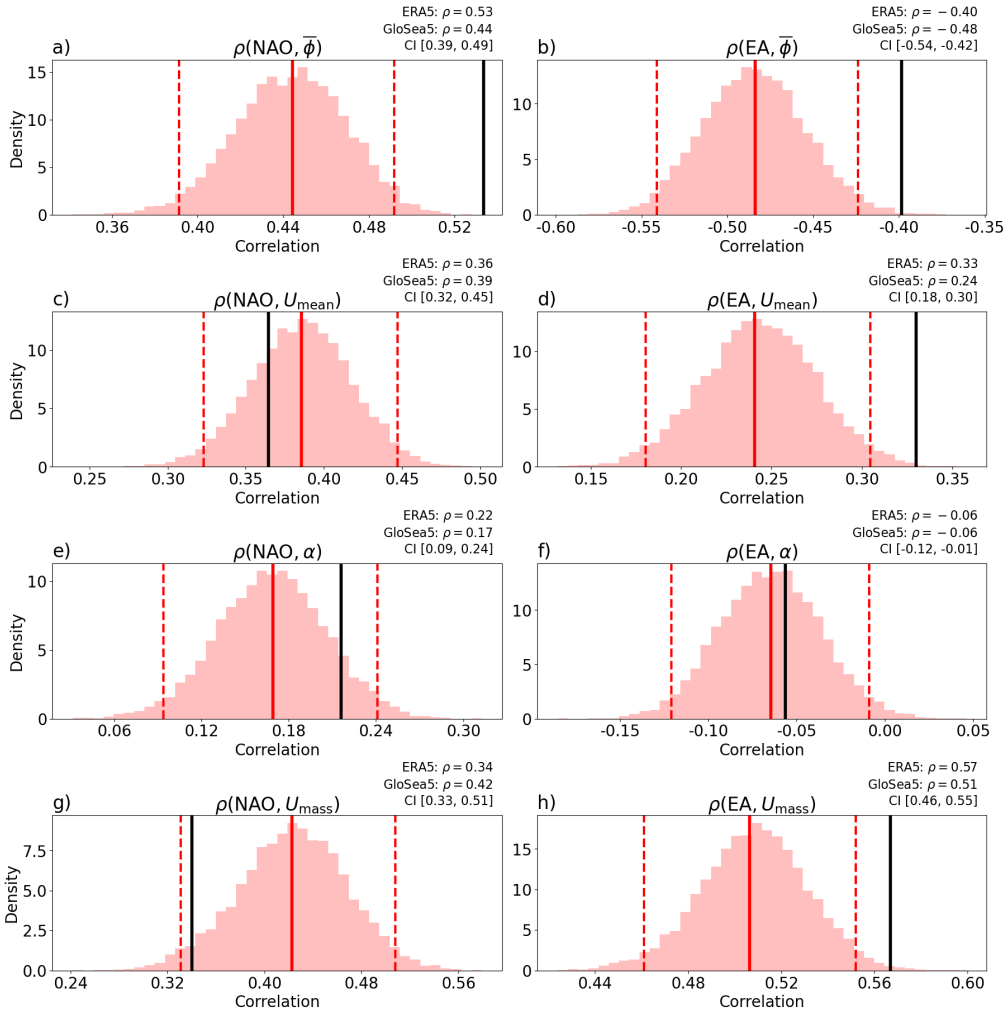

Figure 4.7: Distributions of the Pearson correlation coefficient per member of the daily values in GloSea5 between $\overline{\phi}$ and the NAO a), $\overline{\phi}$ and the EA pattern b), U_{mean} and the NAO c), U_{mean} and the EA pattern d), α and the NAO e), and α and the EA pattern f). The vertical black line is the correlation coefficient for ERA5.

reproduced within the sampling uncertainty. Taken together, the bootstrap analysis shows that the principal deficiency in GloSea5 is an inconsistent representation of EA forcing, while the coupling between the NAO and the EDJ is realistic, but produces inaccurate amplitudes.

4.5.1 Seasonal Predictability

This section considers the ability of GloSea5 to capture interannual variability in the winter (NDJF) mean jet characteristics. Seasonal time series are presented in Figure 4.8 for $\overline{\phi}$, α and U_{mean} from ERA5 and GloSea5. Skill is measured using the Pearson correlation coefficient (ρ) between the ensemble mean and ERA5. A value of 1 indicates a perfect predictive skill, 0 indicates no predictive skill, and -1 would indicate that the model is doing the opposite of what is observed. For each diagnostic, $\overline{\phi}$ is the only measure with significant predictive skill, while α, U_{mean} and U_{mass} show no predictive skill for winter.

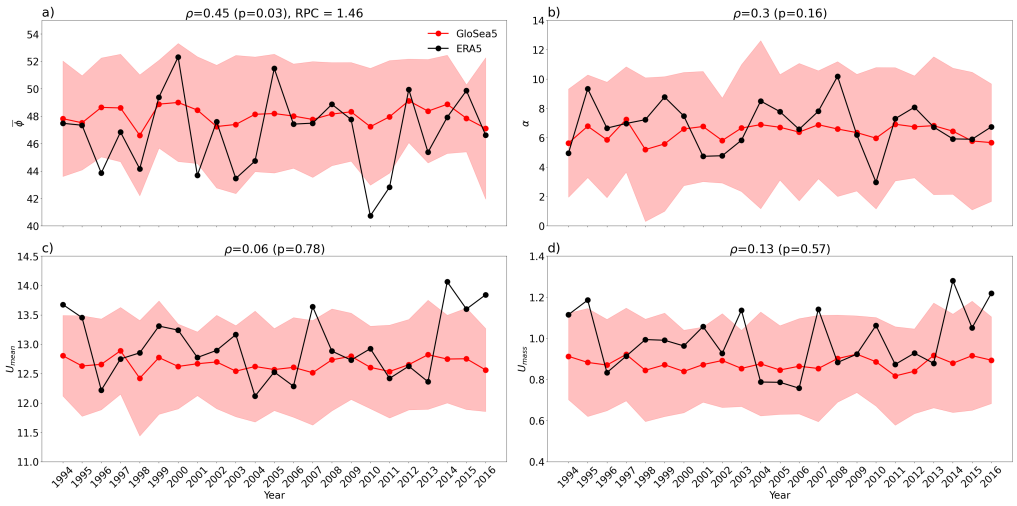

Figure 4.8: Seasonal plots (NDJF) of $\overline{\phi}$ a), α b), U_{mean} c) and U_{mass} for ERA5 (black) and GloSea5 (red) where red shading is the 2σ model spread. The pearsonr correlation score (ρ) where the p-value for the correlation is given in brackets and the ratio of predictable components (RPC) is given at the top of each plot for p-values less than 0.05.

From Chapter 3, we know that there is a relationship between the EDJ position, strength, and tilt, and the NAO and the EA pattern. Figure 4.9 shows the seasonal time series of the NAO and EA pattern indices. There

is no predictive skill in the NAO, but there is in the EA. This is initially surprising, given the abundance of literature supporting seasonal predictive skill in the NAO during winter. However, Thornton et al. (2023) shows that there is a switch in predictive skill between the NAO and the EA depending on the month of initialisation. Thornton et al. (2023) shows predictive skill in the NAO when initialised in November, but not with an initialisation in October, which has been used here. The fact that GloSea5 shows skill for predicting $\overline{\phi}$ but not the NAO is interesting, since the latitude of the EDJ is commonly associated with changes in the NAO. As was shown in the previous section GloSea5 underestimates the link between the NAO and $\overline{\phi}$ and overestimates the relationship to the EA pattern. This suggests that the skill in $\overline{\phi}$ may be driven by the EA pattern.

To further assess the forecasts I have calculated the ratio of predictable components (RPC)

$$\text{RPC} = \frac{\rho}{\sqrt{\frac{\sigma_S^2}{\sigma_N^2}}}, \tag{4.5}$$

where σ_S^2 is variance of the model ensemble mean and σ_N^2 represents variance from each ensemble member (Eade et al., 2014). In an ideal scenario, RPC should equal one, indicating perfect capture of predictable components by the model. However, RPC has meaning only for variables with significant predictable skill; therefore, it has been calculated only for $\overline{\phi}$ and for the EA and not for the others. For $\overline{\phi}$, RPC exceeds 1 which indicates an overconfidence in the forecasts. Sources of this may be the same as those proposed for the NAO, such as horizontal resolutions, air-sea coupling, or eddy-feedbacks. These are not explored in this work, but this does provide evidence for a signal-to-noise problem in the latitude of the EDJ.

4.6 Conclusions and Discussion

In this chapter, I explore how GloSea5 represents EDJOs compared to ERA5, with a focus on daily distributions, relationships among diagnostics, temporal evolution, and seasonal predictability. At the start, I presented an

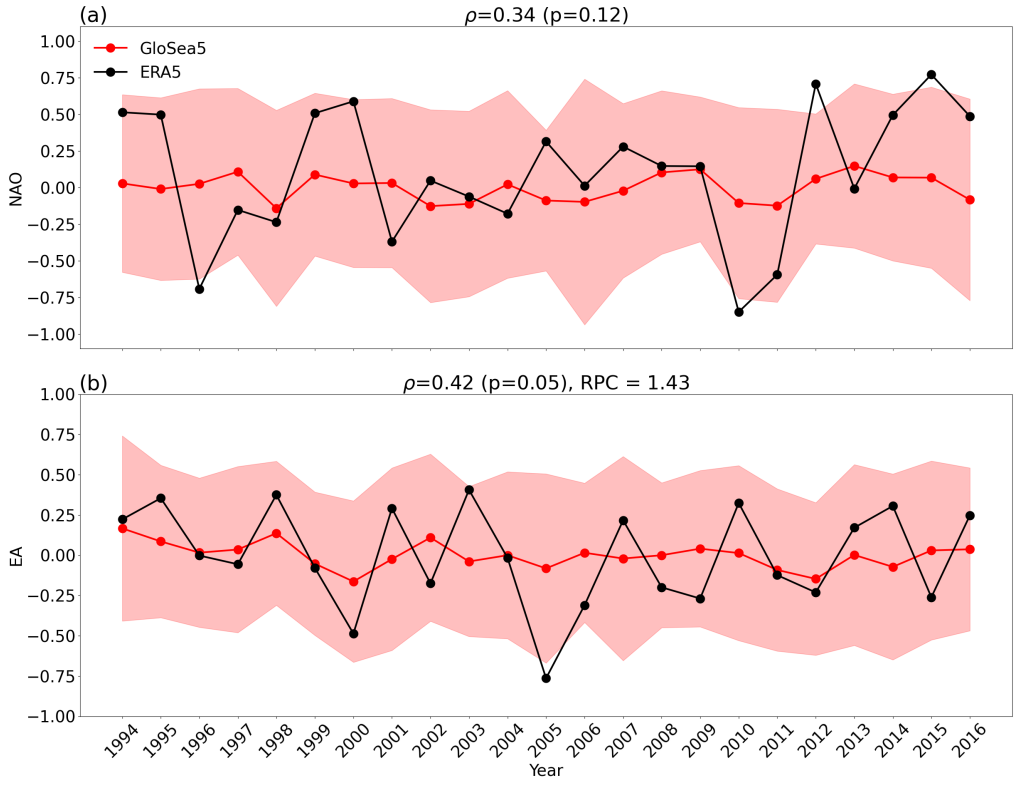

Figure 4.9: Same as Figure 4.5 but for the NAO a) and EA b) indices.

overview of the EDJOs and their representation in GloSea5. This revealed differences in each of the diagnostics, but all within the model spread (defined as two standard errors from the mean), meaning that GloSea5 represented each of the diagnostics well. The differences that I found in $\overline{\phi}$ agree with Parker et al. (2019) who found using the Jet Latitude Index (JLI) that there was an under-representation of southern EDJs and an increase in northerly EDJs in GloSea5. Similarly, Parker et al. (2019) also found that EDJ was weaker in GloSea5, but this is not consistent in different seasonal forecasting models. Looking further at the relationships, I looked at how GloSea5 represented the joint distributions compared to ERA5. Again, I found that GloSea5 did well in recreating these relationships, such as EDJs with α close to zero having less variability in $\overline{\phi}$.

I then looked at the time-variability of the EDJ in GloSea5. I started with the average daily evolution over the months November-February for each EDJ variable (Figure 4.4). Here I find that GloSea5 struggles to capture the evolution of $\overline{\phi}$, during late December and early January, where in ERA5 there is an equatorward shift in the EDJ which lies outside the spread of GloSea5. During this period, there is a high probability of stratospheric warming events (Ineson et al., 2023), which is known to lead to an equatorward movement of the EDJ, which, from this plot, we can see is not captured in GloSea5. The evolution of the other characteristics of the EDJ is well captured, the main difference being in the magnitude of U_{mass} and U_{mean} not being captured.

Following this, I focused on the persistence of the EDJ (Figure 4.5). Here I showed that the persistence in $\overline{\phi}$, α and U_{mass} is too low in GloSea5, but for U_{mean} the persistence falls within the spread of GloSea5. The lack of persistence in the strength and tilt of the EDJ has not previously been shown in the literature, but the lack of persistence in these measures will affect the longevity and strength of an extreme event in GloSea5 (García-Burgos et al., 2023). The lack of persistence in the models is likely to be part of the signal-to-noise paradox (Scaife and Smith (2018)), whereby models tend to underestimate the variability of the climate system, which has been linked to weak eddy feedbacks in seasonal forecasting models (Hardiman et al., 2022).

I applied a bootstrapping approach based on resampling winters from GloSea5, to evaluate both the sign and magnitude of each NAO–EDJO and EA–EDJO link in GloSea5 against ERA5. Although GloSea5 gets the sign right in every case, the magnitude of the correlations differ. For the NAO-$\overline{\phi}$ link, the ERA5 correlation lies above the 95% bootstrap interval, so GloSea5 underestimates that relationship; for EA–$\overline{\phi}$, ERA5 falls below the lower bound 95%, meaning that the model overestimates (the correlation is too negative) the link. By contrast, the NAO–U_{mean} and NAO–U_{mass} correlations in ERA5 both lie within the 95% CI, indicating the model captures their strength. Whereas for EA–U_{mean} and EA–U_{mass}, the ERA5 correlation again exceeds the upper 95% bound, showing GloSea5 underestimates the EA–EDJO relationships. Only α lies within the 95% CI for both the NAO and the EA. The deficiency in these pattern could be due to other biases in representing North-Atlantic dynamics. The potential sources for this weak connection could be an underestimate of the blocking frequency previously reported for climate models (Fabiano et al., 2020), where by lower blocking events the EDJ would not capture the associated shifts, hence leading to a EDJ that is too equatorward. The results of the bootstrapping agree with the results of Parker et al. (2019), who also finds that the EDJ latitude in GloSea5 has a stronger correlation with the EA and strength with the NAO, but with a shorter time period (1993-2009) and looking at the months December-February (DJF).

The seasonal predictability of NAO is well recorded in the literature (Scaife et al., 2014), but for the selected set of data I do not find a predictable skill in NAO but I do in the EA pattern (Figure 6.3). Thornton et al. (2023) shows that the forecasts initialised in October result in predictability in the EA, and predictability in the NAO occurs for the initialisations in November, which they suggest is due to variations in the El Niño Southern Oscillation. For the EDJ, I find that there is predictability in $\overline{\phi}$ (Figure 4.8), but not in any of the other characteristics of the EDJ. The predictability in $\overline{\phi}$ is interesting as it suggests that the EDJ latitude is predictable at longer lead times than the NAO and the EA pattern may be the source of this predictability. However, there is a signal-to-noise issue (Scaife et al., 2014), in $\overline{\phi}$ that indicates overconfidence in the seasonal forecast. From the

bootstrapping results, the predictability in $\overline{\phi}$ might be occurring for the wrong reasons due to its link to the EA being too strong in GloSea5 and too weak with the NAO.

Chapter 5

Configurations of the Eddy-Driven Jet and their relationship with Surface Climate

5.1 Introduction

This chapter explores the relationship between different configurations of the Eddy-Driven Jet (EDJ) and on surface climate variables, measured through precipitation (P) and 2m air temperature (T2m). In Chapter 4 I showed that there was seasonal predictability in the latitude of the EDJ ($\overline{\phi}$), but not in its strength or tilt (U_{mean}, U_{mass}, or α). By examining these relationships in ERA5 and GloSea5, my objective now is to understand how variations in EDJ characteristics contribute to the spatial distribution and intensity of P and T2m anomalies, particularly across Europe. This will also help assess the extent to which the variability of EDJ influences the predictability of surface impacts, including extremes in P and T2m.

The chapter is structured to provide a comprehensive assessment of these relationships. First, I present the spatial correlations between the individual EDJ diagnostics and P and T2m, highlighting regions where variability

in the latitude, strength, and tilt of the EDJ significantly impacts surface conditions. I will then evaluate the extent to which GloSea5 can replicate these patterns compared to ERA5, focussing on differences in magnitude and spatial representation. Second, I will analyse how specific configurations of the EDJ, based on combinations of $\overline{\phi}$, α, and U_{mass}, influence the P and T2m anomalies throughout Europe. By identifying these configurations, I aim to characterise the role of the EDJ in modulating regional surface climate. Finally, I will focus on the extremes in P and T2m in the UK, examining the evolution of the characteristics of EDJ before, during, and after these events. This analysis will assess the potential for using EDJ variability to predict extreme weather events and evaluate the ability of GloSea5 to capture extreme events compared to ERA5.

This work aims to improve our understanding of the interactions between EDJ and surface climate and to assess the ability of GloSea5 to represent these dynamics, particularly to forecast surface impacts and the timing of extremes.

5.2 Spatial Correlations

To understand the spatial relationship between the EDJOs, P and T2m, I have performed a linear regression at each grid point between $\overline{\phi}$, α, and U_{mass} for both P and T2m in ERA5 and GloSea5. The regression is calculated for each member in GloSea5 and then the average correlation is shown. Statistical significance of the regression is shown by stippling at each grid point at the 95% level.

5.2.1 Precipitation

For ERA5 (Figure 5.1a), the regression between $\overline{\phi}$ and P a pattern that resembles the NAO, with positive correlations over Iceland and a large region of negative correlation over the Azores. This indicates that an equatorward shifted jet leads to higher P in southern Europe and lower P in northern Europe. In GloSea5 (Figure 5.2a), the spatial correlation is very similar to ERA5, with the same regions of positive and negative correlations, but the strength of the correlation is weaker. The regression between α in ERA5

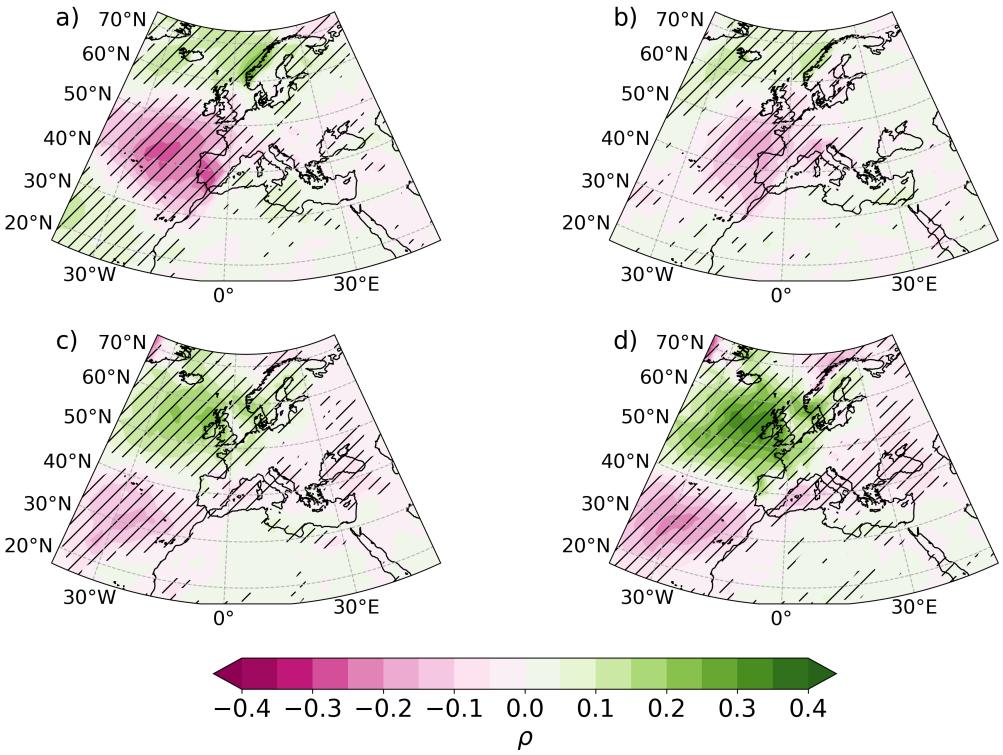

Figure 5.1: Gridpoint Pearson correlation coefficients of the daily precipitation with $\overline{\phi}$ a), α b), U_{mean} c) and U_{mass} d). Stippling indicates a significant correlation at the 95% level.

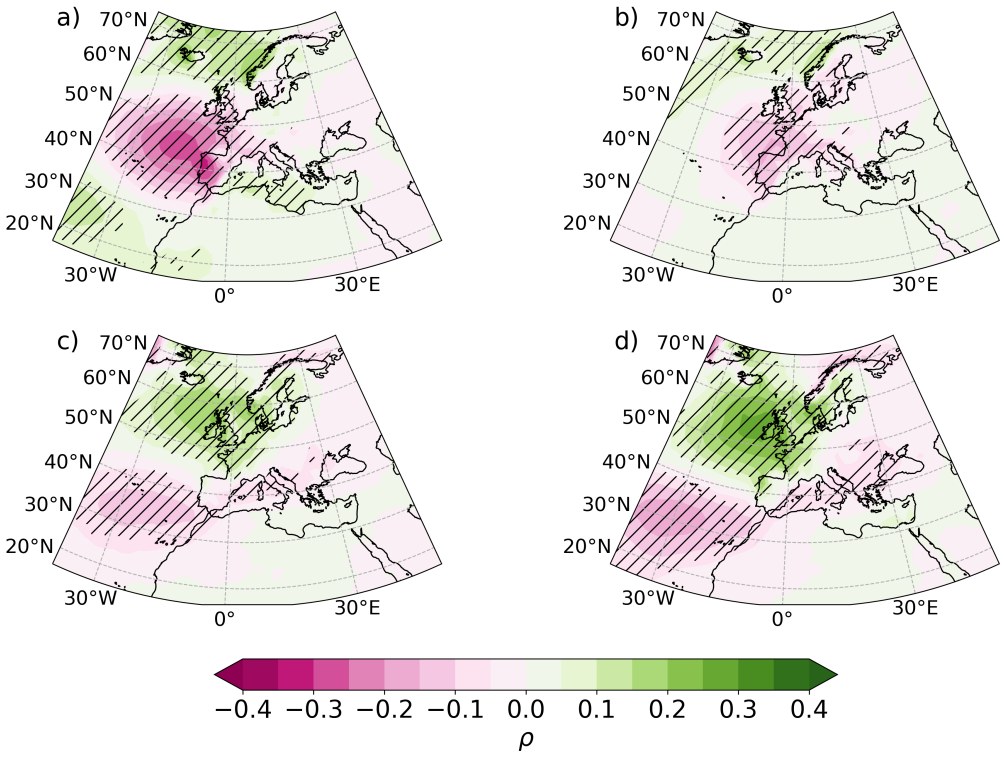

Figure 5.2: Same as Figure 5.1 but for GloSea5. The correlations are calculated each member and then averaged to give the resultant pattern.

(Figure 5.2 b), shows a similar pattern to $\overline{\phi}$, resembling an NAO-type pattern but shifted slightly poleward. This indicates that a more zonal EDJ would lead to more P in central Europe, and a tilted EDJ would lead to an increase in P in the north of the UK and Scandinavia. GloSea5 creates a similar pattern to ERA5 (Figure 5.2b). However, as before the correlations are weaker in GloSea5.

The strength of EDJ is measured by both U_{mean} and U_{mass}, where both correlation patterns in ERA5 (Figures 5.1c and d) are spatially similar, with stronger EDJs leading to more P over the north of Europe and weaker over the south. The magnitude of the correlation is much higher in U_{mass} than in U_{mean}, which means that the size of the EDJ plays a role in the impacts. This pattern resembles the EA pattern, that has been associated with modulation of the strength of the EDJ. The same relationship and spatial pattern are found in GloSea5 (Figures 5.2 c and d) and U_{mass} having a higher magnitude of correlation with P in GloSea5. The same theme

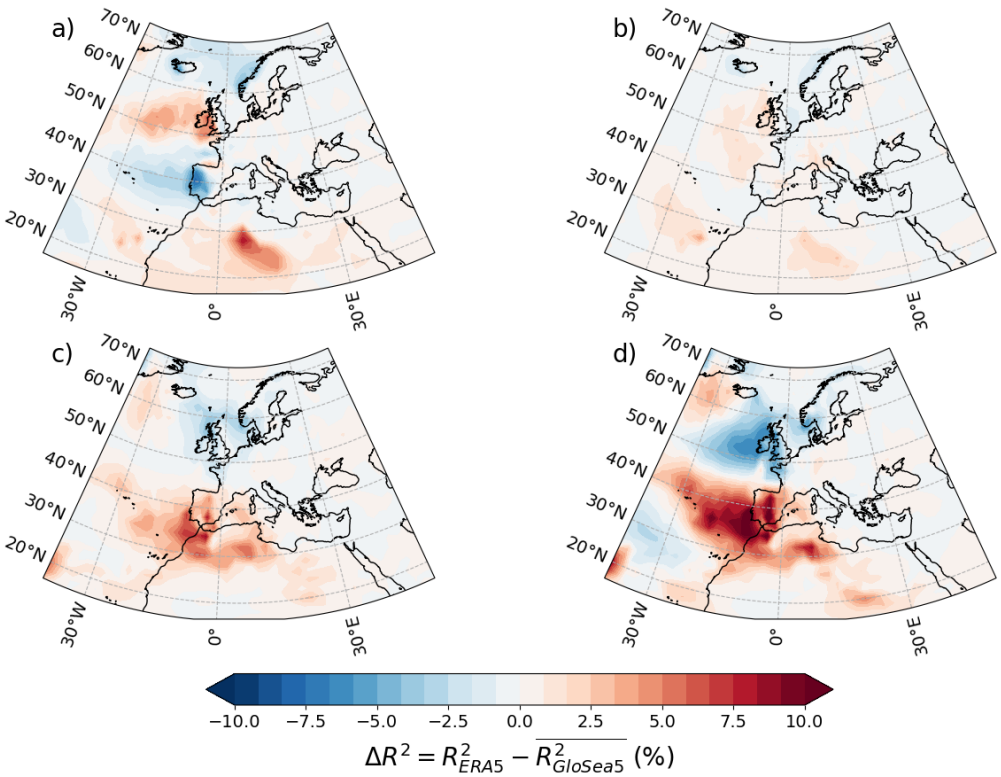

Figure 5.3: Difference in the variance explained (ΔR^2, expressed as a percentage) between ERA5 and GloSea5 for daily wintertime Precipitation for a) $\overline{\phi}$, b) α, c) U_{mean}, and d) U_{mass}. Positive values (red) indicate that the diagnostic explains more variance in ERA5 than in GloSea5, while negative values (blue) indicate greater explained variance in the opposite.

continues, where again the magnitude of the correlations is weak in the models.

Figure 5.3 shows the difference in the explained variance R^2 between ERA5 and GloSea5 for P for each of the EDJ diagnostics. For $\overline{\phi}$ (Figure 5.3a) explains more variability ($\Delta R^2 = 3\%$) over Ireland and the south west of the UK than in GloSea5, while GloSea5 explains a similar amount but over Iberia than ERA5. There is little difference between the two for α (Figure 5.3b). For U_{mean} (Figure 5.3c), there are regions over Iberia and North Africa where GloSea5 tends to underestimate the variability and overestimates over the UK. The differences in U_{mean} are amplified in U_{mass}, thus highlighting that GloSea5 tends to overestimate P over the UK and underestimate in Iberia and North Africa.

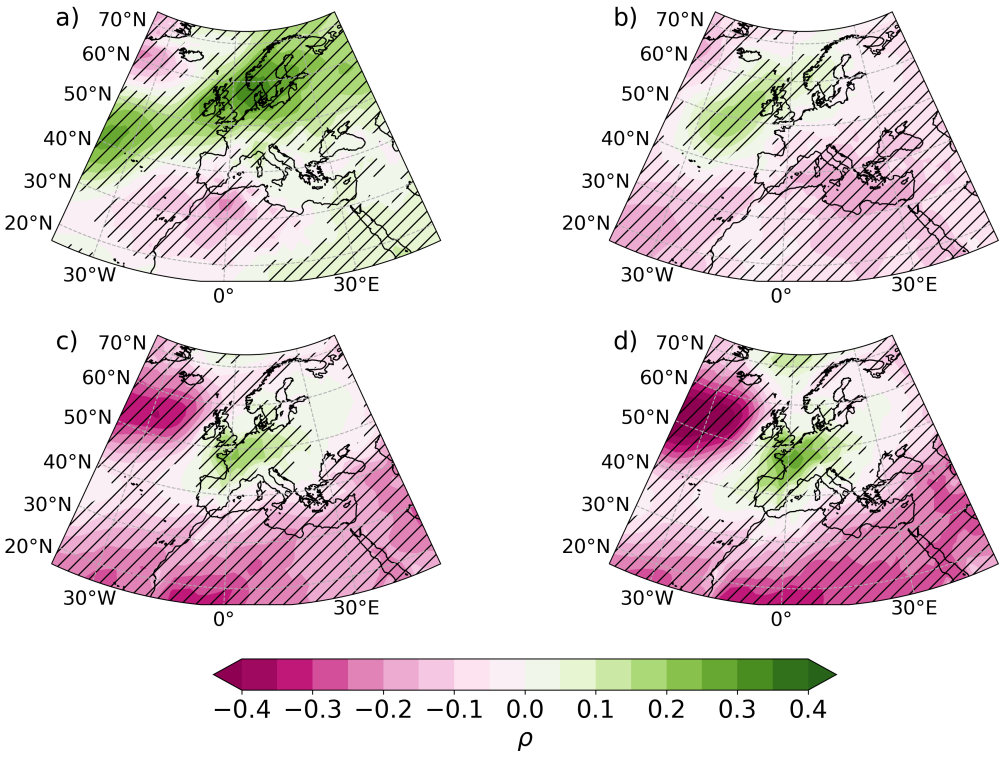

Figure 5.4: Same as Figure 5.1 but for T2m.

5.2.2 2m Temperature

In T2m, the correlation with $\overline{\phi}$ (Figure 5.4a) shows warmer temperatures over the UK, Scandinavia and northern and central Europe when the EDJ is anomalously poleward, and colder temperatures in Spain and northern Africa. This spatial pattern in ERA5 is recreated in GloSea5 very well (Figure 5.5a), the main difference being the stronger magnitude of the correlation over Spain and northern Africa. For α (Figure 5.4b), warmer temperatures are seen in the north of the UK and Scandinavia when the EDJ is positively tilted and colder temperatures are seen in the south.

It is interesting to note that P, that the patterns for $\overline{\phi}$ and α are quite similar, but not for T2m. Here for α, there is a positive correlation region that sits on a small part of the UK and Scandinavia, while for $\overline{\phi}$ it covers a larger area in northern Europe.

This pattern of α in GloSea5 (Figure 5.5 b) is again really well recreated in GloSea5, with the same significant positive correlations being seen in the

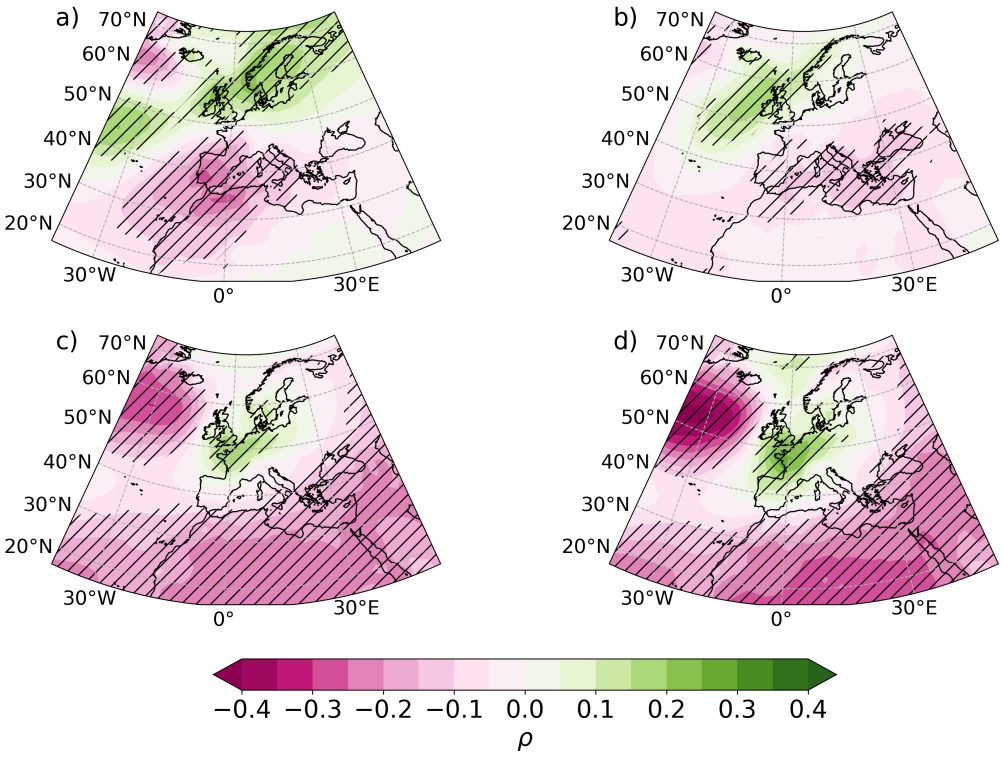

Figure 5.5: Same as Figure 5.2 but for T2m.

same areas as seen in ERA5. The patterns in U_{mean} and U_{mass} are similar in ERA5 (Figures 5.4 c and d), where there is a negative correlation region in the centre of the Atlantic and a positive correlation region in the UK.

Figure 5.6 shows the difference R^2 in T2m between ERA5 and GloSea5 for each of the EDJ diagnostics. Here we can see markedly different results from what we saw for the differences in P. There is a higher region of higher R^2 for $\overline{\phi}$ ($\Delta R^2 = 7\%$) over Egypt (Figure 5.6a) and no noticeable differences are seen for α (Figure 5.6b). The differences become more apparent in both U_{mean} and U_{mass} (Figures 5.6c and d), where there is a clear dipole in the centre of the Atlantic. The magnitude of the difference in U_{mass} is substantial compared to $\Delta R^2 = 20\%$.

5.3 EDJ Configuration and Impacts

Different states of the EDJ have been shown to have different impacts in different regions of Europe (Barriopedro et al., 2022). Here, I show different

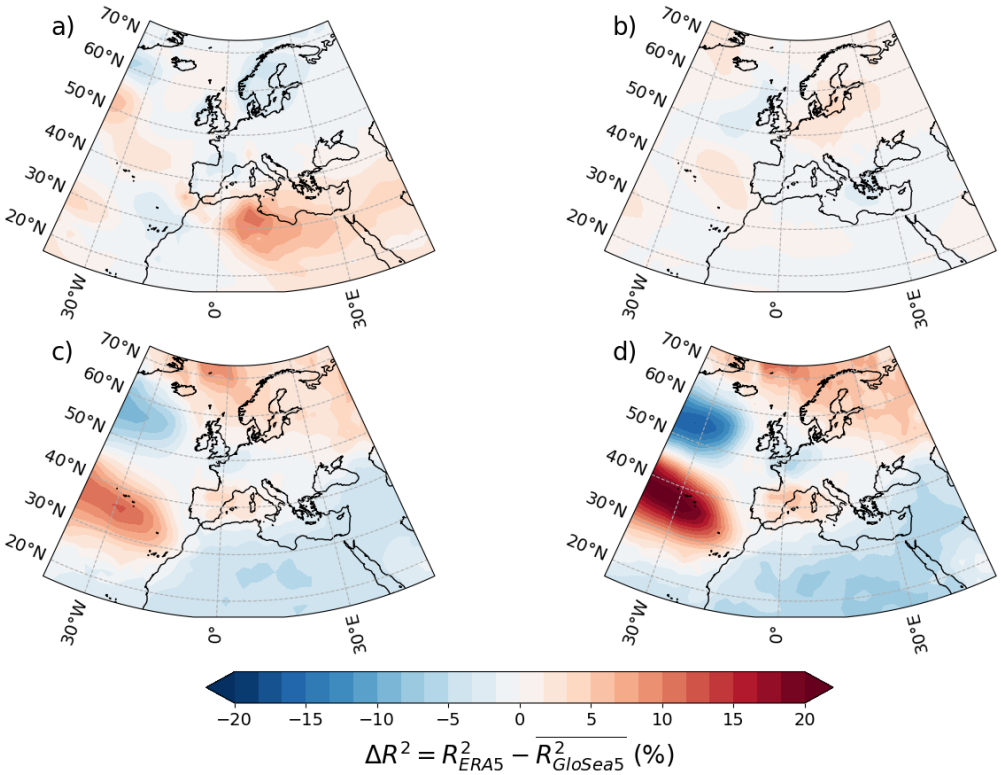

Figure 5.6: Same as Figure 5.3 but for T2m. Note magnitude of the colour-bar has changed.

configurations of the EDJ based on daily values of $\overline{\phi}$, α and U_{mass} being larger or less than the respective climatological mean. The partitioning of the EDJ diagnostics in this way leads to eight composite patterns. I have chosen to use U_{mass} over U_{mean} because it has been shown in the previous section to be more related to the variability of both P and T2m. Figures 5.7, 5.8, 5.9 and 5.10 show composites of P and T2m anomalies based on the different EDJ configurations in ERA5 and GloSea5, where the values at the top of each figure are the mean values for the respective data set. The anomalies are relative to the full-time mean in each dataset, where for GloSea5 it is calculated for each member and then averaged.

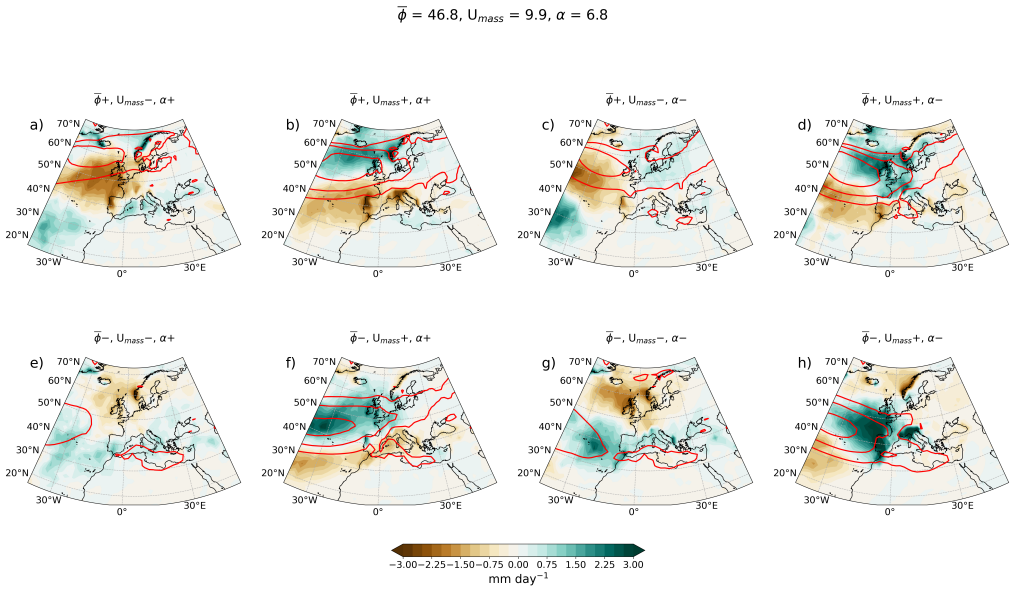

Figure 5.7: Anomalies of P (mm/day) in ERA5 for eight composites of the EDJO diagnostics, based on deviations from mean values: $\overline{\phi}$, U_{mass} and α. Each panel represents a different combination of values larger (+) or less than (-) the mean for these EDJ diagnostics, as indicated at the top of the Figure. Brown shades indicate drier-than-average conditions, and blue-green shades indicate wetter-than-average conditions. Red contours indicate the zonal wind at 850hPa.

The P anomalies generally follow the latitude of the EDJ. When the EDJ is positioned poleward ($\overline{\phi}+$), wetter than average conditions tend to dominate northern Europe, while drier anomalies are observed further south. In contrast, an equatorward EDJ ($\overline{\phi}-$) shifts the wetter anomalies toward southern Europe, with drier conditions extending across northern Europe.

This latitude-dependent structure is consistently captured in both ERA5 and GloSea5, highlighting that EDJ latitude has a significant influence on the spatial distribution of precipitation anomalies throughout Europe, which is captured in the model.

The strength of EDJ (measured by U_{mass}) acts to set the intensity of the P anomalies. Stronger than average jets ($U_{\text{mass}}+$) are associated with more pronounced precipitation anomalies, with wetter conditions in northern Europe and drier conditions in southern Europe when the EDJ is poleward and vice versa. Configurations with weaker than average jet strength ($U_{\text{mass}}-$) generally show more muted precipitation anomalies, regardless of position. This suggests that stronger EDJ events amplify wetter P anomalies in Europe, contributing to distinct wet and dry regions depending on the position of the EDJ. An example of this can be seen in Figures 5.7 and 5.8a and b, where the position is the same but the difference in U_{mass} leads to an increase in wet anomalies.

Further modifications to the spatial pattern of precipitation anomalies are introduced by α. For example, in poleward jet configurations ($\overline{\phi}+$), a positive tilt ($\alpha+$) shifts wetter conditions toward Scandinavia, while drier anomalies extend over central Europe. Similarly, for equatorward jet configurations ($\overline{\phi}-$), a positive tilt leads to wetter conditions in southern Europe and drier anomalies further north. This shows that the tilt of the EDJ can modify precipitation distributions within latitude-dependent patterns, creating regional shifts in precipitation anomalies. Another example of this can be seen in Figures 5.7 and 5.8b and c, where the poleward jet with a higher than average tilt ($\alpha+$) impacts more of northern Europe, but the shift to a lower than average tilt ($\alpha-$) leads to wet anomalies over the UK and central Europe and less over the north of Europe.

Together, the eight composites reveal a spectrum of spatially varied surface impacts. A poleward-displaced jet that is both weak and positively tilted ($\overline{\phi}+, U_{\text{mass}}-, \alpha+$) produces only a dry anomaly on the coast of Ireland and wet anomalies over Scandinavia. But when that same jet strengthens ($\overline{\phi}+, U_{\text{mass}}+, \alpha+$), the dipole intensifies, deepening the dryness over Iberia and enhancing the wet anomalies over Scandinavia. Retaining the jet yet reversing the tilt ($\overline{\phi}+, U_{\text{mass}}-, \alpha-$) shifts the region of dry anomalies west-

ward into the Atlantic. Again, the stronger counterpart ($\overline{\phi}+$, $U_{\text{mass}}+$, $\alpha-$) magnifies that west-shifted pattern but now with wet anomalies centered over the UK and some parts of central Europe.

For the configurations for an equatorward jet ($\overline{\phi}-$), there is a reversal in the sign of the anomalies: a weak, positively tilted equatorward jet ($\overline{\phi}-$, $U_{\text{mass}}-$, $\alpha+$) is where the wet and dry anomalies are weakest, while its strong analogue ($\overline{\phi}-$, $U_{\text{mass}}+$, $\alpha+$) leads to a large shift in the wet anomalies with the UK at the centre. With a negative tilt, the weaker equatorward jet ($\overline{\phi}-$, $U_{\text{mass}}-$, $\alpha-$) again shifts the dipole of westward wet anomalies so they are centred on the Canaries, with dry anomalies over the UK. The stronger counterpart to the negatively tilted configuration ($\overline{\phi}-$, $U_{\text{mass}}+$, $\alpha-$) produces the largest wet anomalies of all configurations, with the largest anomalies over Iberia and dry anomalies in Iceland and Scandinavia.

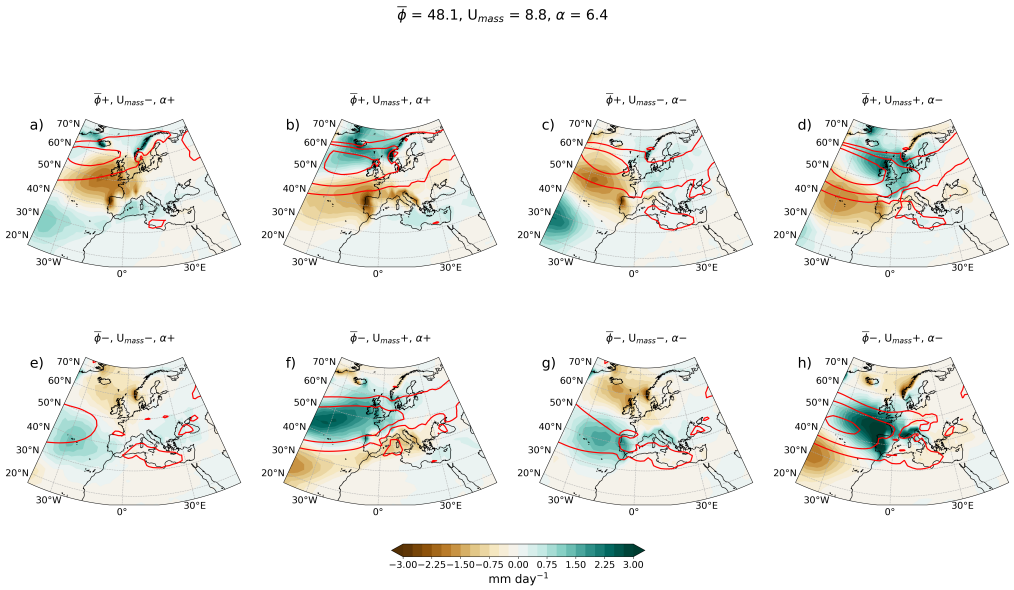

Figure 5.8: Same as Figure 5.7 but for GloSea5.

Looking now at the T2m anomalies, the warm anomalies generally align with the latitude of the EDJ, as with wet anomalies in the precipitation. When the EDJ is positioned poleward ($\overline{\phi}+$), warmer than average conditions tend to dominate northern Europe, while cooler anomalies are seen further south. Hence, an equatorward shifted EDJ ($\overline{\phi}-$) shifts the warmer

temperature anomalies toward southern Europe, with cooler conditions extending throughout northern Europe. This latitude-dependent structure is consistently captured in both ERA5 and GloSea5.

For U_{mass}, the relationship with the T2m anomalies is more complex. For poleward jets in ($\overline{\phi}+$), there are generally warm anomalies over northern Europe and Scandinavia regardless of the strength of the EDJ. Warm anomalies tend to extend further east when the jet is stronger than average ($U_{\text{mass}}+$), and are more confined to the west when weaker than average ($U_{\text{mass}}-$). It appears that the higher than average tilt ($\alpha+$) and the strength ($U_{\text{mass}}+$) localise the warm anomalies over the UK and Scandinavia, whereas the lower than average tilt ($\alpha-$) sees the warm anomalies spread over a larger area of Europe.

Focusing on equatorward-shifted jets ($\overline{\phi}-$), generally stronger jets ($U_{\text{mass}}+$) lead to warm anomalies and weaker jets ($U_{\text{mass}}-$) lead to colder anomalies. There is a direct spatial effect on the anomalies with α, where the higher than average tilt ($\alpha+$) shifts the warm anomalies over central Europe and the south of the UK, while the lower than average ($\alpha-$) creates a cold anomaly over the UK and warmer anomalies over southern Europe. The effect of α on weak jet days ($U_{\text{mass}}-$) is none for equatorward shifted jets, where there is a consistent cold anomaly over Europe for these configurations.

A weak, positively tilted poleward jet ($\overline{\phi}+$, $U_{\text{mass}}-$, $\alpha+$) produces a warm anomaly, with warming over Scandinavia and a cool tongue stretching from Iberia into the central Mediterranean. Keeping the same latitude and tilt combination but increasing the strength ($\overline{\phi}+$, $U_{\text{mass}}+$, $\alpha+$) simply amplifies the warm anomaly across southern Norway while the cold anomaly over the Mediterranean deepens. If the poleward jet remains weak yet the tilt is reversed ($\overline{\phi}+$, $U_{\text{mass}}-$, $\alpha-$), the pattern shifts westward so that positive anomalies are over Iceland–Scotland and negative anomalies sit over Iberia and the Bay of Biscay.

Increasing the jet strength ($\overline{\phi}+$, $U_{\text{mass}}+$, $\alpha-$) yields the most intense warming of any $\overline{\phi}+$ case, with a large warm anomaly over the Norwegian Sea and cold anomalies across Portugal. Mirroring the latitude flips the sign

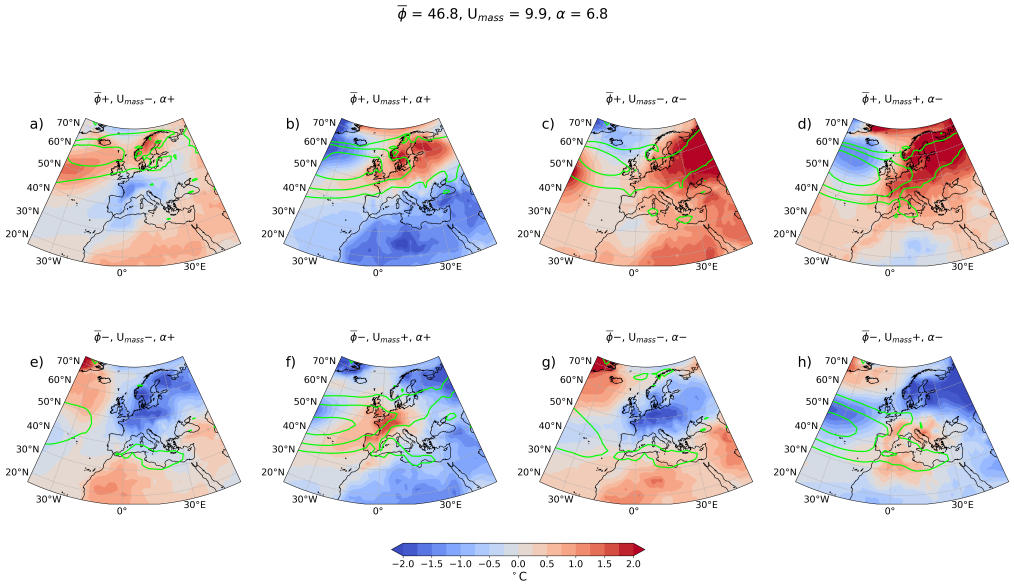

Figure 5.9: Same as Figure 5.7 but for 2m Temperature and zonal wind contours are in green.

of the dipole: a weak, positively tilted equatorward jet ($\overline{\phi}-$, $U_{\text{mass}}-$, $\alpha+$) brings warming to the central and eastern Mediterranean and cooling over the UK and Scandinavia, whereas for the stronger jet ($\overline{\phi}-$, $U_{\text{mass}}+$, $\alpha+$) delivers a southern response, with warm anomalies from Iberia to the Alps and large cold anomalies across the Barents Sea. With a negative tilt, the weak equatorward jet ($\overline{\phi}-$, $U_{\text{mass}}-$, $\alpha+$) again shifts the dipole of westward—warm anomalies now centres on Iberia–northwest Africa while cooling settles over the UK and North Sea and the strong, negatively tilted configuration ($\overline{\phi}-$, $U_{\text{mass}}+$, $\alpha-$) amplifies that pattern in Iberia/Morocco and from the North Sea to Scandinavia.

It is also interesting to note that the largest extremes for P and T2m occur under different configurations of the EDJ. For P, the highest wet anomalies occur for the ($\overline{\phi}-$, $U_{\text{mass}}+$, $\alpha-$) configuration (panel h in Figures 5.7 and 5.8) and the highest dry anomalies for the ($\overline{\phi}+$, $U_{\text{mass}}-$, $\alpha+$) configuration (panel a in Figures 5.7 and 5.8). For T2m, the warmest anomalies are seen for the configurations ($\overline{\phi}+$, $U_{\text{mass}}-$, $\alpha-$) (panel c in Figures 5.9 and 5.10) and ($\overline{\phi}+$, $U_{\text{mass}}+$, $\alpha-$) (panel d in Figures 5.9 and 5.10) and the coldest for the configurations ($\overline{\phi}+$, $U_{\text{mass}}-$, $\alpha+$), ($\overline{\phi}-$, $U_{\text{mass}}-$, $\alpha-$) and ($\overline{\phi}-$, $U_{\text{mass}}+$, $\alpha-$) (panels e, g, and h in Figures 5.9 and 5.10).

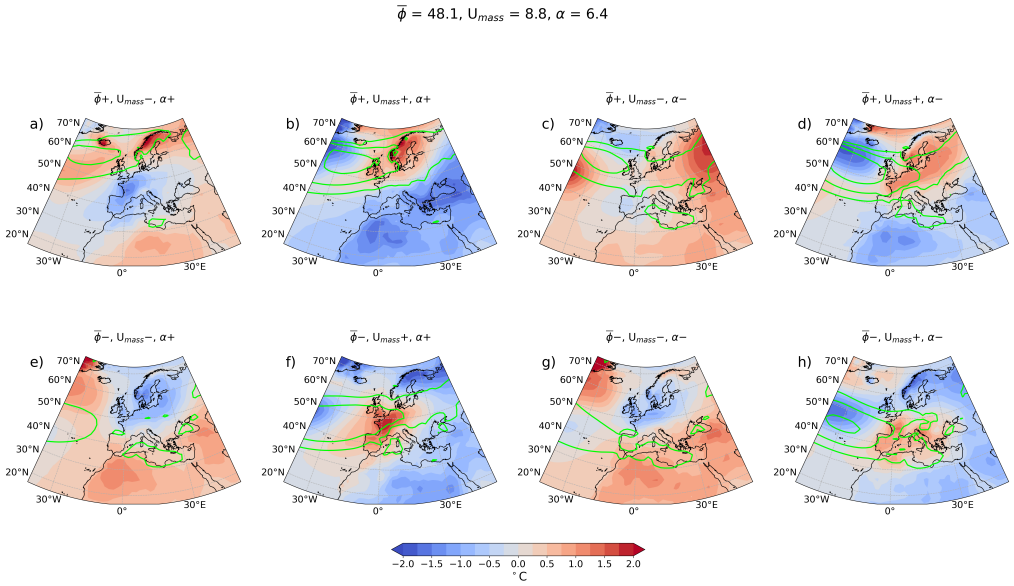

Figure 5.10: Same as Figure 5.10 but for GloSea5.

It is also worth highlighting the varying complexity of the relationship between the EDJ with both P and T2m. For P, wet and dry anomalies are largely driven by U_{mass} and spatially equatorward shifted EDJs ($\overline{\phi}-$) is where the most extreme wet anomalies are seen, with poleward EDJs ($\overline{\phi}+$) giving rise to drier anomalies. For T2m anomalies, the relationship is more complex with multiple configurations giving rise to both warm and cold extremes. Comparing GloSea5 with ERA5, GloSea5 effectively captures the general spatial patterns of the EDJ configurations observed in ERA5 for both T2m and P anomalies, even for the extreme cases outlined previously. However, GloSea5 consistently displays less intense anomalies, suggesting that it can reproduce the broad spatial relationships, it may under-represent the magnitude of both the temperature and precipitation extremes.

5.4 UK Extremes

The previous section showed that there is a strong connection between the spatial patterns of both P and T2m with various configurations of the EDJ. Hence, in this section, we will explore the evolution of the EDJ before and after an extreme in P and T2m over the UK. To identify extremes over

the UK, I define a box (49-61°N and 11°W - 2°E) and take a daily average of P and T2m to define two time series. Then, I define days that exceed the 95th percentile as extreme wet or hot days, and days below the 5th percentile as extreme dry or cold days. The average difference between the extremes in GloSea5 and ERA5 for extreme warm and cold days can be seen in Figures 5.11 a and c, and for extreme wet and dry days in Figures 5.11 b and d.

The differences between GloSea5 and ERA5 on warm days are shown in Figure 5.11a where there is a large negative difference (where GloSea5 is too cold) in the Norwegian Sea that extends over Scotland and into the North Sea, with differences reaching up to 3°C. There is little difference in the UK for the cold extremes (Figure 5.11c), suggesting that GloSea5 captures these events well in this region, while the differences appear mainly in eastern Europe where GloSea5 is too cold, particularly by around 1-2°C. The warm and dry extremes (Figures 5.11b and d) are well represented in the UK, with little difference in magnitude for both temperature and precipitation. Overall, the extreme days are generally well represented in GloSea5, with the main discrepancy being that GloSea5 tends to be too warm, especially affecting the north of Scotland in the warm extremes.

Next, I examine the evolution of $\overline{\phi}$, U_{mass}, and α 15 days before and after the extreme days to assess the behaviour of the EDJ around these extremes. To composite these days, I create a mask of days in the time series that exceeds the 95th percentile. Then, to avoid counting stretches of extreme days that occur more than once, I only identify the event that is at the onset. I also discard any events that start within the first or last 15 days of the winter to ensure that I am capturing the full 30 day evolution of the events.

The evolution of the T2m extremes is shown in Figure 5.12 and the P extremes is shown in Figure 5.13. For the warm extreme (Figure 5.12a). In both datasets, $\overline{\phi}$ (Figure 5.12c) sits around its mean position before the extreme event, where in ERA5 it begins to shift poleward, but in GloSea5 it remains around its mean. Analysing α (Figure 5.12e), before the event, the value of α reduces below the mean indicating a zonalization of EDJ in both, but in GloSea5 the magnitude is smaller. Even after the event, the EDJ

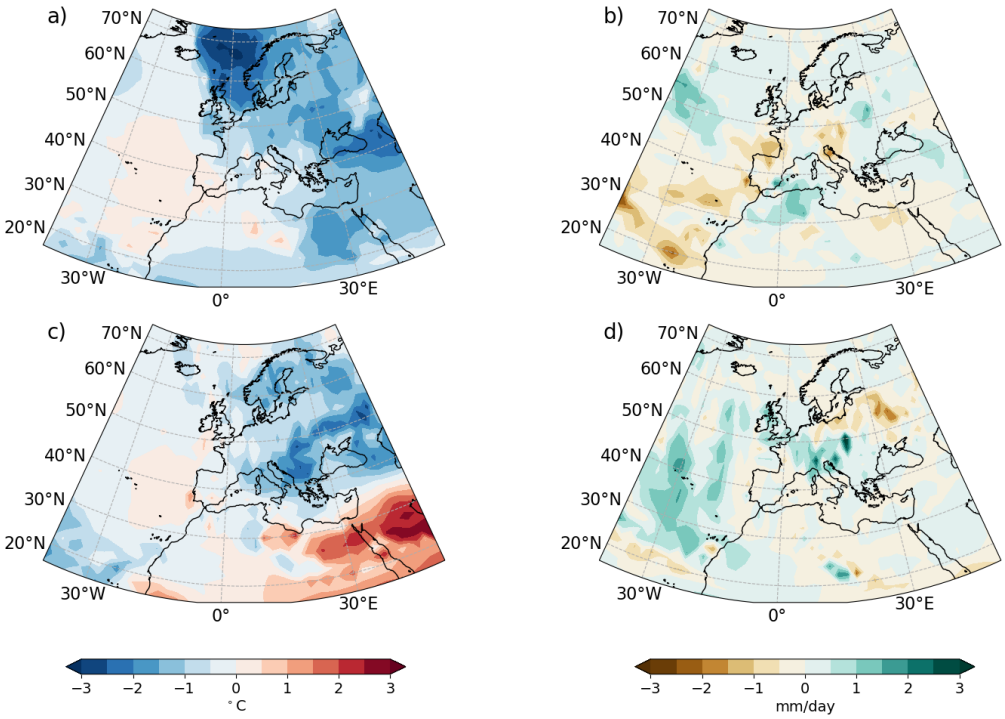

Figure 5.11: Differences between GloSea5 and ERA5 for extreme 2m air temperature and precipitation events over Europe. The extremes are defined based on area-averaged values over the UK. Panels a) and c) show 2m air temperature differences for days above the 95th percentile and below the 5th percentile, respectively. Panels b) and d) show precipitation differences for the same percentiles.

remains in a more zonal state in ERA5 before returning close to its mean. There is a sign of a reduction in α in GloSea5, but its magnitude is not close to that seen in ERA5. Then for U_{mass} (Figure 5.12g), in ERA5 the strength is around its mean value well before the event and then weakens below its mean afterward. However, in GloSea5, it appears to show a consistently weaker than average EDJ for the entire duration.

Considering the cold extremes (Figure 5.12b) the magnitude is higher in GloSea5 than in ERA5. The evolution of $\overline{\phi}$ for these event (Figure 5.12d) shows an equatorward shifted $\overline{\phi}$ starting on days 9 or 10 prior to the event and peaking around 2 days before, which is seen in both ERA5 and GloSea5. In α (Figure 5.12f), prior to the event, the EDJ shows a more zonal structure with values lower than the mean in both ERA5 and GloSea5, and this begins to recover to the mean 5 days after the cold event. For U_{mass}, there is a clear weakening of the EDJ in ERA5, which reaches a minimum 9 or 10 days before the event and begins to strengthen, reaching a maximum strength about 4 days after the event. In GloSea5, the evolution of U_{mass} is slightly different; the minimum in U_{mass} occurs only 2 or 3 days before the event, but the strengthening of the EDJ is captured, though it does not exceed its mean value. As was seen for the warm extremes, U_{mass} remains less than the mean value for the entire event.

Moving to the P extremes (Figure 5.13), we can see that the evolution of the EDJ is different from that for the T2m extremes. For wet extremes (Figure 5.13a), $\overline{\phi}$ (Figure 5.13 c) stays at its mean value before, during and after the extreme event. This is reflected in the evolution of the EDJ in GloSea5. In α (Figure 5.13e), there is a tendency for the EDJ to be more zonal before the event, returning back to climatology after the event. Again, we see that GloSea5 recreates the evolution of α. For U_{mass}, there is a clear strengthening of the EDJ, which exceeds the mean strength around 10 days before the event, where the strength peaks and begins to decline, returning to around the mean on day 7. GloSea5 captures the strengthening of the EDJ, but growth occurs around 5 days prior to the event, peaking 1 day before the event.

For dry extremes (Figure 5.13b), the evolution of $\overline{\phi}$ (Figure 5.13d) in ERA5 differs from the evolution in GloSea5. In ERA5 the EDJ remains close to

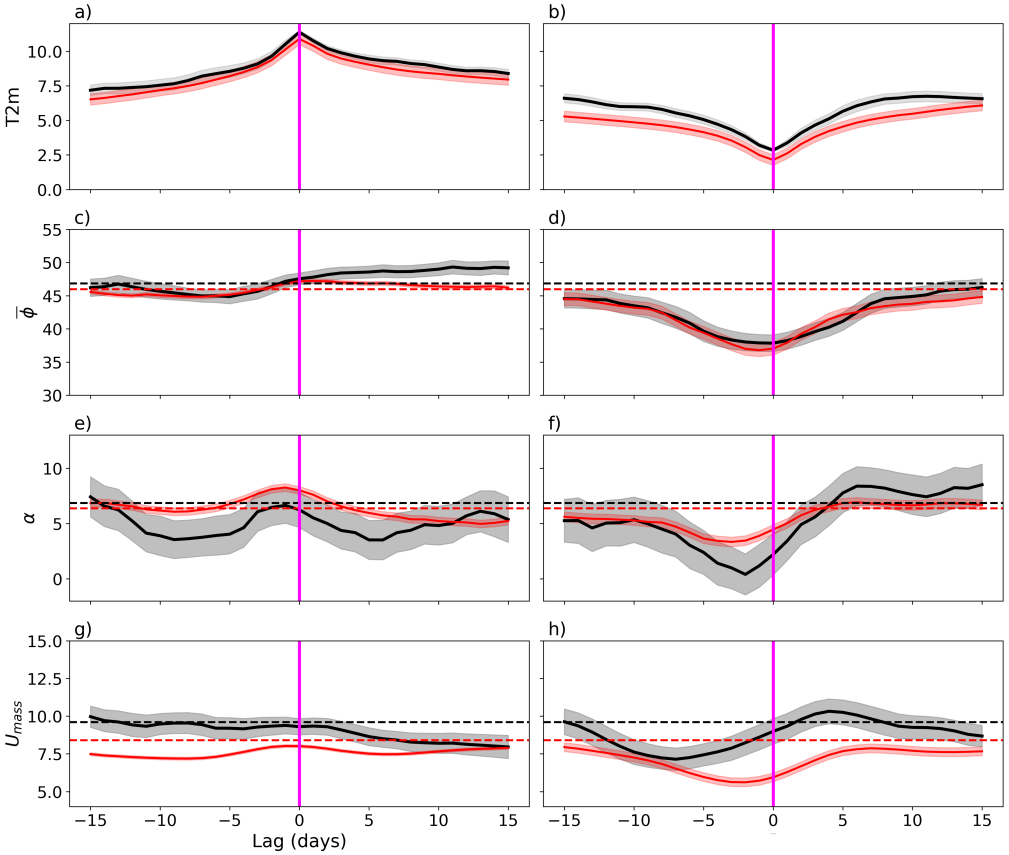

Figure 5.12: Composite analysis of the evolution of T2m, $\overline{\phi}(^{\circ}\mathrm{N})$, $\alpha(^{\circ})$, and $U_{\mathrm{mass}}(\mathrm{m}^3\mathrm{s}^{-1})$ in ERA5 (black) and GloSea5 (red) during extreme temperature events. Panels a, c, e, and g represent composites around the 95th percentile (warm events), while panels b, d, f, and h represent composites around the 5th percentile (cold events). Solid lines represent the ensemble mean, while shaded regions indicate the 95% spread. The horizontal dashed lines represent the mean value for each dataset, and the vertical magenta line mark the onset of the extreme event.

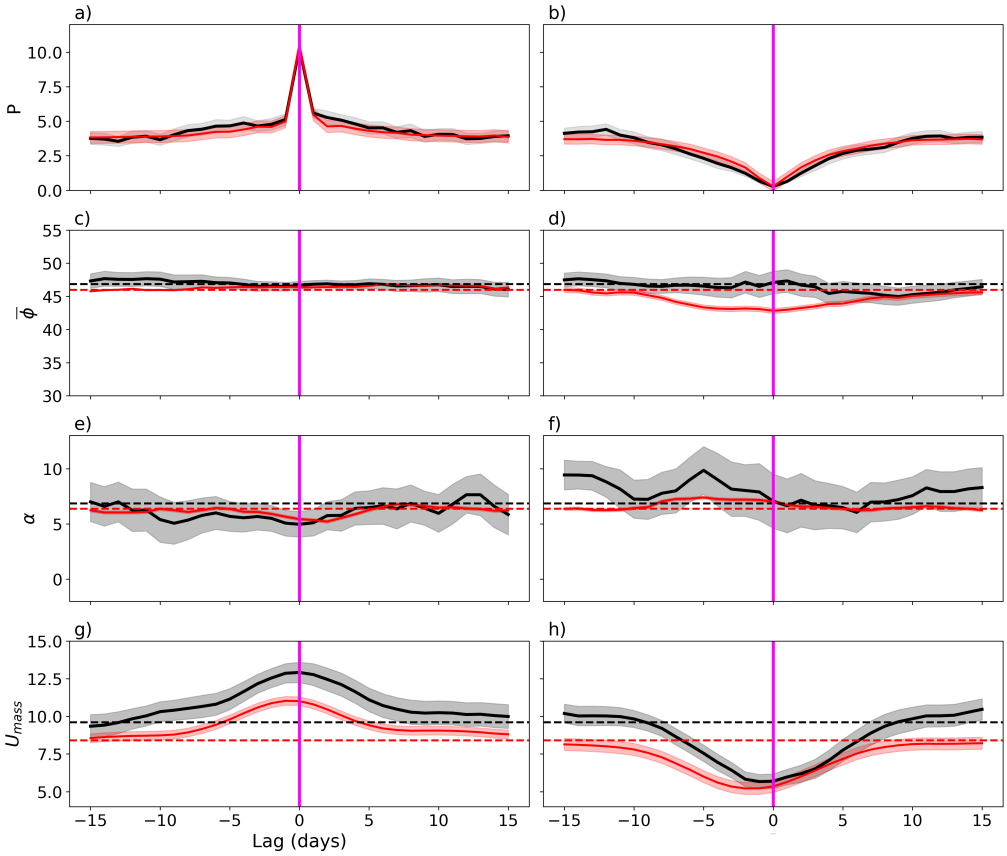

Figure 5.13: Same as Figure 5.12 but for P and for wet and dry events.

its mean latitude prior to and during the event, whereas in GloSea5 the EDJ moves equatorward 10 days prior to the event and remains around this latitude until 5 days after, where it returns back to its mean. From α (Figure 5.13f) in ERA5, there is generally a greater than average tilt in the EDJ before the day of the event and after it is closer to mean. In GloSea5, the same level of variability is not seen, with the evolution of α sitting close to the mean for the duration. Lastly, U_{mass} (Figure 5.13h), there is a weakening of the EDJ that begins 7 days before the dry event and then reaches its minimum on the day of the event before strengthening again afterward. This is well captured in GloSea5, which matches the timing of weakening and minimum.

5.5 Conclusions and Discussion

In this chapter I have examined how different characteristics of the EDJ; latitude ($\overline{\phi}$), tilt (α), mean strength (U_{mean}) and mass (U_{mass}) are related to precipitation (P) and 2m air temperature (T2m) in ERA5 and analysed their representation in GloSea5 to understand the relationship between EDJ and surface impacts.

I started by showing the spatial patterns of the correlations of each component with P and T2m across Europe and found distinct patterns for each of the EDJ components in GloSea5 that were spatially similar ERA5 (Figures 5.1, 5.2, 5.4 and 5.5). For P, $\overline{\phi}$ influences the precipitation distribution, with poleward jet excursions associated with wetter conditions in northern Europe and drier conditions in the south and vice versa. For T2m, $\overline{\phi}$ has a similar relationship with temperature, with warmer anomalies related to poleward jets and cooler anomalies for equatorward jets. GloSea5 effectively captured these spatial patterns. Interestingly, U_{mass} and U_{mean} both showed similar correlation patterns, but the correlations were higher in U_{mass}, indicating that the actual size and strength of the EDJ play an important role in understanding surface impacts.

To assess how much of the day-to-day surface variability is actually controlled by the jet, I then compared the fraction of variance explained (R^2) in ERA5 and GloSea5. For precipitation, ERA5 shows that $\overline{\phi}$ for up to

3% more variance than the model over Ireland and the south-west UK, whereas GloSea5 has a larger R^2 over Iberia. There is little contribution from α in either dataset, but for both U_{mean} and for U_{mass} the model underexplains the variability in Iberia and North Africa while having large R^2 in the British Isles with differences ranging from 5 to 7% for U_{mean} and up to 10% for U_{mass}.

For T2m, ERA5 links poleward jet excursions to pronounced warming over Egypt ($\Delta R^2 = 7\%$), that is not captured in GloSea5. A dipole pattern of ΔR^2 appears in the centre of the Atlantic for both U_{mean} and U_{mass}, with GloSea5 underestimating R^2 over the Canary Islands and overestimating south of Iceland. Both of the regions show a $|\Delta R^2| = 20\%$ for U_{mass}. Collectively, these R^2 differences confirm that while GloSea5 reproduces the pattern of jet–surface coupling, it underestimates the magnitude and sometimes misplaces the location of that influence, especially for U_{mean} and U_{mass}.

From the correlation analysis, I then defined eight composites based on days with parameters above or below the mean value the mean values of $\overline{\phi}$, α and U_{mass} (Figures 5.7,5.8, 5.9 and 5.10) to understand how different multivariate configurations of the EDJ are related to different surface climate signals in Europe. In P, U_{mass} determines the intensity of precipitation anomalies. Stronger jets amplify wet anomalies, while α influences regional shifts, with a more zonal jet leading to different impacts compared to a tilted jet. For T2m, $\overline{\phi}$ and α play a greater role in determining the location of the anomalies T2m. For example, stronger EDJs often lead to warm anomalies in central and southern Europe, depending on the tilt and latitude.

Based on understanding how different configurations of the EDJ change the T2m and P anomalies, I specifically focused on extremes in P and T2m over the UK and how the evolution of the EDJ does or does not differ. I defined a wet extreme event from P by selecting days that exceed the 95th percentile of an area-average of P over the UK and dry extremes as days less than the 5th percentile. The same thresholds are used for T2m to define warm and cold events, respectively. Then I looked at 15 days before and after the extreme event and looked at the averaged evolution in

$\overline{\phi}$, α and U_{mass} (Figures 5.12 and 5.13). Overall, while GloSea5 captured the broad spatial patterns of EDJ evolution during UK extremes, it consistently showed reduced intensity and variability compared to ERA5. This under-representation suggests that GloSea5 struggles to accurately forecast extreme temperature and precipitation events, particularly in terms of their timing and severity.

Chapter 6

Sub-Seasonal and Seasonal drivers of the Eddy-Driven Jet

6.1 Introduction

The variability of the North Atlantic circulation is strongly influenced by teleconnections, which modify large-scale atmospheric patterns through the propagation of Rossby waves (Strong and Magnusdottir, 2008; Woollings et al., 2008). This first part of this chapter focusses on two key teleconnection patterns: ENSO and the QBO. Both ENSO and QBO have been shown to alter the phase of the NAO (Ayarzagüena et al., 2018; Cai et al., 2022; O'Reilly et al., 2024), which directly connected with the storm tracks and the structure of the EDJ. Chapter 3 presented a new two-dimensional method for describing the EDJ structure that can offer additional insights to other methods that perform zonal averaging. This chapter examines how variations in the latitude ($\overline{\phi}$), strength (U_{mean}), size (U_{mass}), and tilt (α) of EDJ are affected by the different characteristics of seasonal predictability. Here I aim to explore the seasonal impacts of ENSO and QBO phases on the EDJ, with a particular focus on the differences between early winter (November–December) and late winter (January–February). These periods are characterised by distinct modes of variability, with the East Atlantic (EA) pattern dominating early winter and the NAO becoming more prominent in late winter (Thornton et al., 2023). By investigating the

intra-seasonal differences, I seek to provide a more nuanced understanding of EDJ variability under these modes of variability.

In addition to seasonal variability, in this chapter I examined the subseasonal variability of the EDJ, which is also modulated by the tropics, particularly through the MJO. The MJO is a major source of subseasonal variability in the tropics that influences North Atlantic atmospheric circulation via changes in the likelihood of positive and negative phases of the NAO (Cassou, 2008; Skinner et al., 2022). However, relatively little research has investigated how the MJO influences the specific characteristics of the EDJ. Using ERA5 and the EDJO framework, I will explore the lagged response of the EDJ to different phases of MJO, identifying how each MJO phase influences the latitude, strength, size, and tilt of the EDJ over time.

This chapter is organised as follows. First, I investigated the seasonal variability of the EDJ in different ENSO and QBO phases, comparing the responses in ERA5 and GloSea5 for early and late winter. The aim is to assess the model's ability to capture observed EDJ variability and identify biases in the representation of teleconnection impacts. Second, I used ERA5 to examine the subseasonal variability of the EDJ in response to the MJO, focussing on how the EDJ responds to different MJO phases and the timescales of these responses. By combining these analyses, this chapter aims to provide a comprehensive understanding of how seasonal and subseasonal drivers modulate EDJ characteristics, with implications for the predictability of the North Atlantic circulation and its associated impacts.

6.2 Data and Methods

6.2.1 Datasets

This chapter uses two datasets, the ERA5 reanalysis (Hersbach et al., 2020) and data from the Met Office seasonal forecasting model GloSea5 (MacLachlan et al., 2014). From GloSea5 I took data initialised on 1st of October to capture the extended winter November-February (NDJF) for the years 1994 - 2016. For ERA5 I use data from 1960 - 2020 for NDJF.

Throughout the chapter I refer to data as being from either the hindcast period or the full period, which corresponds to the 1994-2016 period and the 1960-2020 respectively. The full period is used to provide more samples of the different phases of ENSO and the QBO, and this also allows us to say whether the hindcast period is unique or not based on the historical record.

6.2.2 El Niño Southern Oscillation

ENSO is calculated using the NINO3.4 index, where an area average is taken over 170°W -120°W and 5°N - 5°S of sea surface temperature anomalies (SST) with respect to the full winter climatology. A threshold of ±0.5°C is used to define the El Niño and La Niña phases, respectively. Here I have also excluded extreme El Nino years (when anomalies exceed 2°C) as it has been shown that the dynamics of these years are significantly different from the typical response seen in other El Niño years (Hardiman et al., 2019; Toniazzo and Scaife, 2006).

6.2.3 Quasi-Biennial Oscillation

The QBO is calculated from the 50hPa zonal wind averaged between $5°\text{N} - 5°\text{N}$. An anomaly threshold of $\pm 5\text{ms}^{-1}$ is used to define the westerly phase of the QBO (QBOw) and the easterly phase (QBOe) (Gray et al., 2018).

6.2.4 Statistical Testing for ENSO and the QBO

The Kolmogorov-Smirnov (KS) test is a non-parametric statistical test used to determine whether two datasets are drawn from the same underlying distribution. The KS test compares the empirical cumulative distribution functions (ECDFs) of the observed dataset and the hindcast dataset. The null hypothesis (H_0) states that the observed and hindcast distributions are identical, while the alternative hypothesis (H_1) states that they differ.

The KS test statistic, D, is defined as

$$D = \max_x \left| F_{\text{obs}}(x) - F_{\text{hcst}}(x) \right|, \tag{6.1}$$

where $F_{\text{obs}}(x)$ is the empirical cumulative distribution function of the observed values and $F_{\text{hcst}}(x)$ is the empirical cumulative distribution function of the hindcast values.

The statistic D represents the maximum vertical distance between the two ECDFs. A higher value of D indicates a greater disagreement between the observed and hindcast distributions. In the context of this study, the KS test is applied to evaluate the agreement between the ERA5 and GloSea5 distributions for variables such as $\overline{\phi}$, U_{mean}, α and U_{mass}. This allows for a quantitative assessment of how well the forecast model reproduces the observed variability and distribution of these key metrics. Identifying where significant differences occur helps to pinpoint the variables or conditions where the forecast performance is weakest.

The data used in the tests are daily data and have an autocorrelation associated with them, as shown in previous chapters. To account for this in the KS test, the effective degrees of freedom (N_{eff}) is used. The definition of N_{eff} is

$$N_{\text{eff}} = N\frac{1-\rho_1}{1+\rho_1}, \tag{6.2}$$

where N is the sample size and ρ_1 is lag-1 autocorrelation.

6.2.5 Madden-Julian Oscillation

The MJO index is calculated for the months of November to April, following Cassou (2008) and Skinner et al. (2022).

I have calculated the real-time multivariate MJO index (RMM), developed by Wheeler and Hendon (2004). Following Wheeler and Hendon (2004), the RMM calculation involves the following steps:

- **Data:** Zonal wind at 850hPa and 200hPa, and outgoing long-wave radiation (OLR), which serves as a proxy for deep convection. The OLR data I used are provided by NOAA from 1974-2020. These variables are averaged over the 15°S–15°N. All data is re-gridded to a 2.5×2.5 degree grid.

- **Removing Long-Term Variability:** To isolate intraseasonal MJO variability, long-term components are removed. This is achieved by removing the annual mean and the first three harmonics of the seasonal cycle.
- **Removal of ENSO variability:** To account for interannual variability, especially related to ENSO, a running mean of 120 days is calculated and removed from each of the variables.
- **EOF Analysis:** Empirical Orthogonal Function (EOF) analysis is conducted on the combined OLR and wind fields. Each field is normalised by its global variance to ensure equal contributions. The analysis is performed over all longitudes. The first two EOFs capture the dominant variability associated with the MJO. The daily anomaly fields are projected onto the leading two EOFs, producing two principal component (PC) time series, which are the RMM1 and the RMM2.

Using RMM1 and RMM2, both the phase and the amplitude is defined as

$$\text{Phase} = \arctan\left(\frac{\text{RMM2}}{\text{RMM1}}\right), \qquad \text{A} = \sqrt{\text{RMM1}^2 + \text{RMM2}^2}, \tag{6.3}$$

where the phase is used to define the location of anomaly and for days when $A > 1$, the MJO is defined as being active.

The phase defines the centres of convective activity as the MJO propagates over the Maritime Continent. Figure 6.1, shows the OLR anomaly in ERA5 for each phase of the MJO, for days when the MJO is active. Negative (positive) anomalies indicate regions of enhanced (suppressed) convection. This shows a negative OLR anomaly that propagates eastward, starting in east Africa (Phase 1) over the Indian Ocean (Phases 2 and 3) and over the Maritime Continent (Phase 4) into the Pacific Ocean (Phases 5, 6 and 7). The cycle then begins again near the east of Africa (Phase 8).

Figure 6.2 shows an example phase space for the period 2017/18. The RMM1 and RMM2 indices are combined in a two-dimensional phase space, where rotations in the phase space indicate eastward propagation of the MJO. Points outside the grey circle are days when the MJO is active.

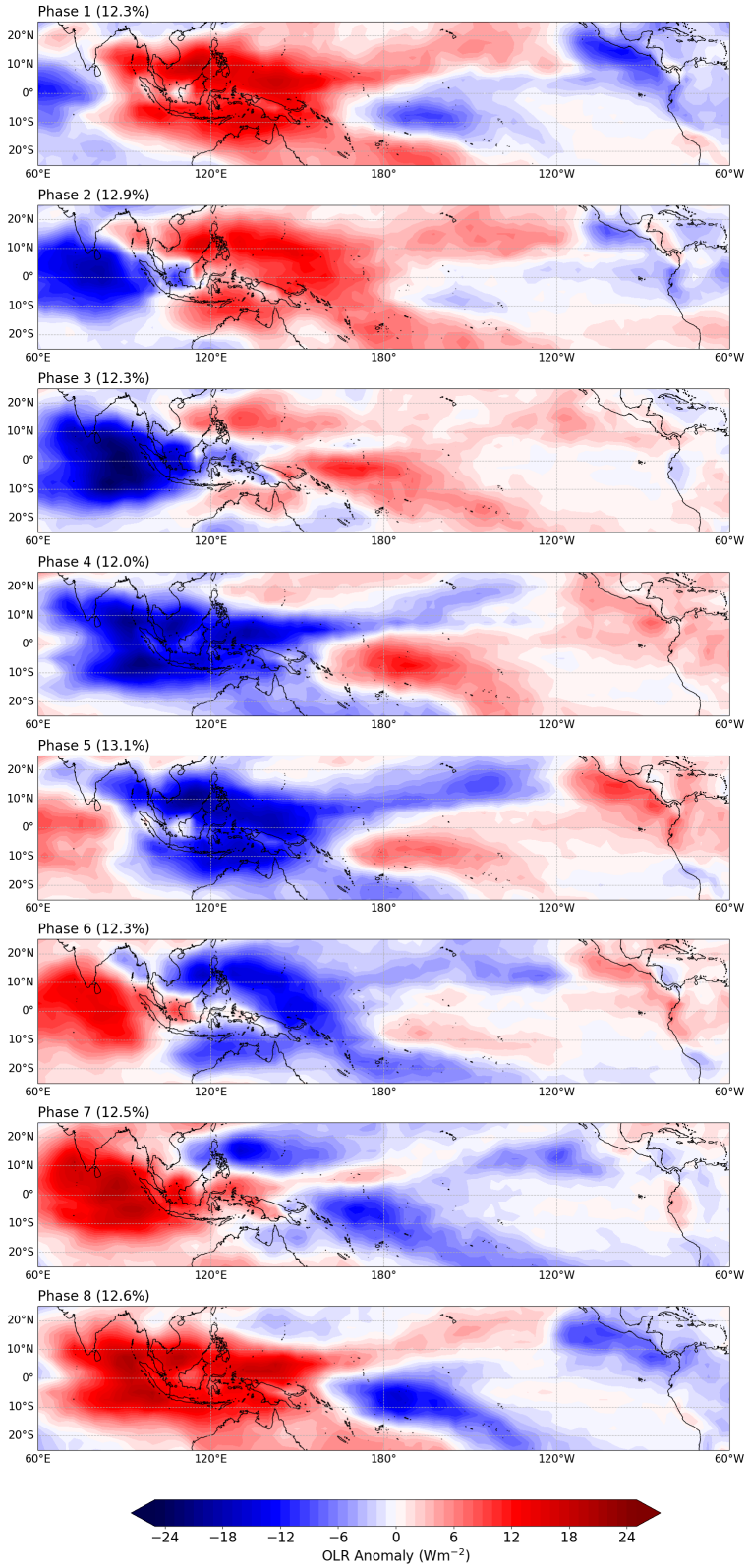

Figure 6.1: OLR anomaly in each phase of the MJO. Positive anomalies are regions of suppressed convection and negative are regions of enhanced convection. The value in the top left of each panel indicates the percentage of days in each phase.

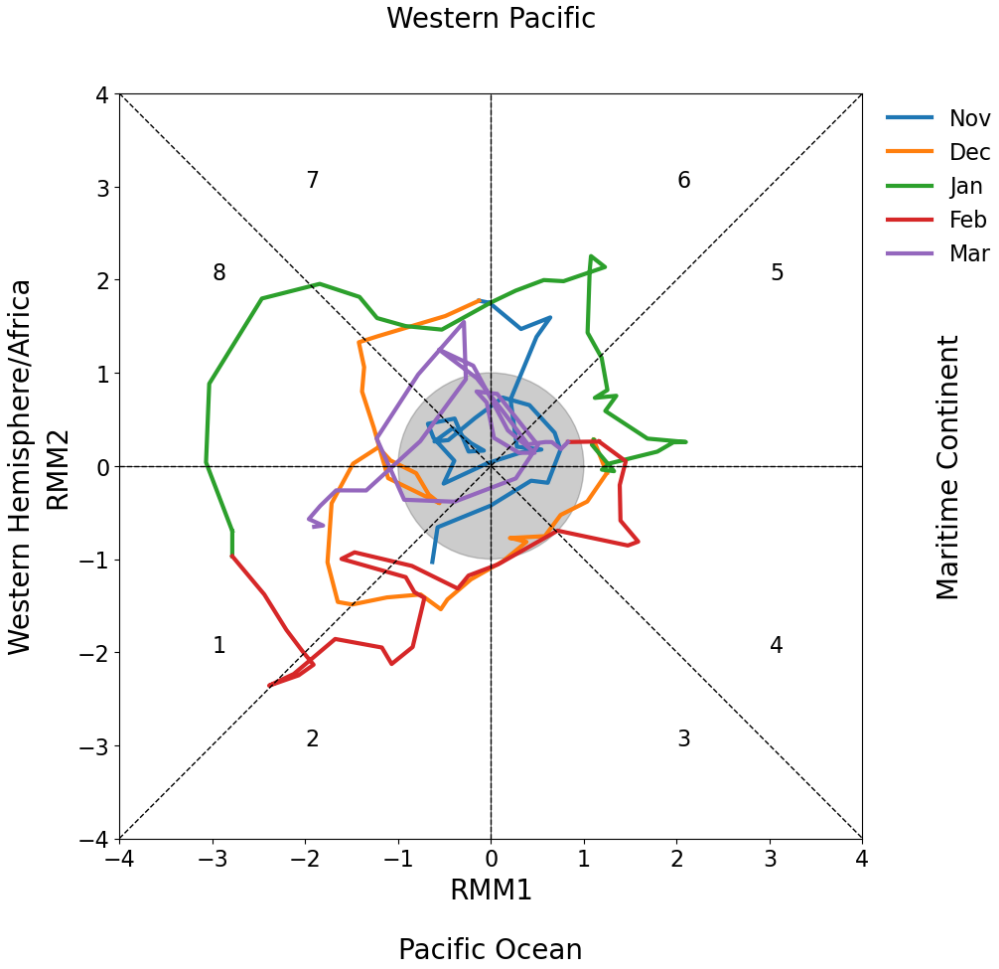

Figure 6.2: Example RMM1 and RMM2 phase space plot for November - March of 2017/2018. The grey circle indicates the regions where A <1 and colours of each of the lines indicate the respective month.

During this period, there is a strong MJO signal towards the end of January that propagates into the Pacific. High-amplitude MJO events have been associated with an increased probability of a sudden stratospheric warming (SSW) events (Garfinkel et al., 2012) and the negative phase of NAO (Cassou, 2008; Skinner et al., 2022). During this year, the UK saw extreme snowfall caused by a high pressure system that was positioned over Scandinavia.

Contingency Tables

To assess the influence of the MJO on the EDJ in the North Atlantic, I calculate contingency tables using standardised distributions of $\overline{\phi}$, U_{mean}, U_{mass} and α.

Following both Cassou, 2008 and Skinner et al., 2022, using days when the MJO is active ($A \geq 1$), then in each MJO phase. I count the number of days when each EDJO diagnostic exceeds 1 or is less than -1 standard deviation (σ). Then I calculate the phase-specific probability

$$P^{\pm}_{\text{phase}} = \frac{\text{days(diagnostic} \geq \pm 1\sigma \text{ in phase)}}{\text{total days in that phase}}, \tag{6.4}$$

and I express percentage change for each MJO phase is then calculated by comparing the probability of these days to the mean climatological occurrence within the respective MJO phase,

$$\Delta P^{\pm}_{\text{phase}} = 100 \times \frac{P^{\pm}_{\text{phase}} - P^{\pm}_{\text{clim}}}{P^{\pm}_{\text{clim}}} \tag{6.5}$$

where $P^{\pm}_{\text{clim}}$ is the long therm probability of exceeding $\pm 1\sigma$ on any active MJO-day. To investigate the time-lagged effects, this calculation is repeated with lags between 1-15, with the MJO leading.

Statistical testing for the MJO

To test for significant changes in climatology at each lag, I use a two-sample proportional t-test with a confidence level of 95%. Specifically, for each diagnostic (that exceeds the threshold $\pm 1\sigma$), I test whether $P^{\pm}_{\text{phase}} = P^{\pm}_{\text{clim}}$ precedes $P^{\pm}_{\text{phase}} \neq P^{\pm}_{\text{clim}}$.

I use the standard t-test for two proportions

$$t = \frac{P^{\pm}_{\text{phase}} - P^{\pm}_{\text{clim}}}{\sqrt{\hat{P}(1-\hat{P})(\frac{1}{n_{\text{phase}}} + \frac{1}{n_{\text{clim}}})}} \tag{6.6}$$

where $\hat{P}$ is the pooled proportion and n are the sample sizes of the number of active MJO days in each phase and for the full climatology. A result is significant if $|t| > 1.96$, which defines the confidence level of 95%. This approach follows Skinner et al., 2022, as it accounts for the fact that not all days will exceed the $\pm 1\sigma$ threshold.

6.3 Seasonal Variability

6.3.1 El Niño Southern Oscillation

The boreal winter ENSO time series is shown in Figure 6.3, where the blue line represents the 1960-2020 period and the black line represents 1994-2016 period for both ERA5 and the red line for GloSea5. For the hindcast period, GloSea5 recreates the observed ENSO with a significant Pearson correlation and an RPC of almost one. In some of the years, there are differences in the magnitude of La Niña years where ERA5 shows a weaker amplitude than in GloSea5.

Sampling sensitivity

To assess the potential sampling bias between the hindcast and the full periods, Figure 6.4 shows the distributions of each EDJO diagnostic for NDJF for both periods. The hindcast period spans just 23 winters, which is less than half of the 62 year full-period record; therefore, there may be some noise contributing to the shapes of the distributions. However, the difference in the sample means between the two periods are well within the realms of sampling variability. To quantify this, I calculated the standard error in the hindcast period as the standard deviation (of the winter mean anomaly for each of the 23 years) in the full period divided by the square root of the number of seasons in the forecast period,

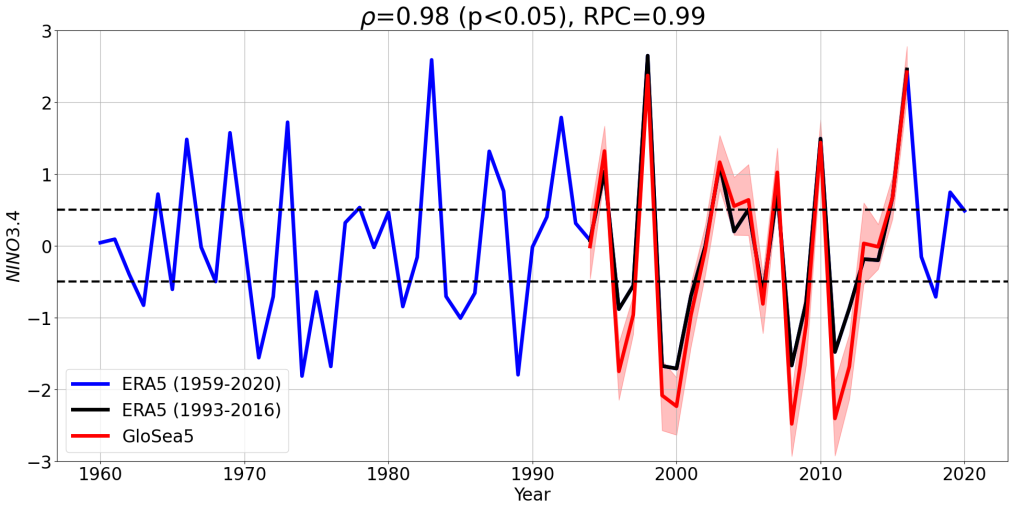

Figure 6.3: Time series of the seasonal NINO3.4 index for NDJF for ERA5 between 1960 - 2020 in blue, ERA5 between 1993/4-2015/16 in black and GloSea5 between 1993/4-2015/16 in red. The solid red line is the Glosea5 ensemble mean and the shading represents the 2σ model spread. The black horizontal dashed lines mark the ± 0.5°C anomaly used to define El Niño and La Niña years. The Pearson correlation coefficient (ρ) with p-value (p) and the RPC score are given at the top.

$$SE_{\text{hindcast}} = \frac{\sigma_{\text{full}}}{\sqrt{23}}. \tag{6.7}$$

For $\overline{\phi}$ (Figures 6.4a and e), $SE_{\text{hindcast}} = 1.46°N$ and the observed difference is approximately 1°N for both El Niño and La Niña. Likewise, for U_{mean} the $SE_{\text{hindcast}} = 0.3\text{ms}^{-1}$ (Figures 6.4b and f), U_{mass} the $SE_{\text{hindcast}} = 0.8\text{m}^3\text{s}^{-1}$ (Figures 6.4c and g) and α the $SE_{\text{hindcast}} = 2.3°$ (Figures 6.4d and h). For El Niño the mean difference between the two periods are $\Delta\, U_{\text{mean}} = 0.4\text{ms}^{-1}$, $\Delta\, U_{\text{mass}} = 0.9\text{m}^3\text{s}^{-1}$, and $\Delta\alpha = 0.6°$. For La Niña they are $\Delta\, U_{\text{mean}} = 0.3\text{ms}^{-1}$, $\Delta\, U_{\text{mass}} = 0.75\text{m}^3\text{s}^{-1}$, and $\Delta\alpha = 0.4°$. Each of the mean differences lies within one standard error, hence the minor mean changes in the forecast period curves are entirely attributable to statistical noise, rather than the forecast period being unique from the full period.

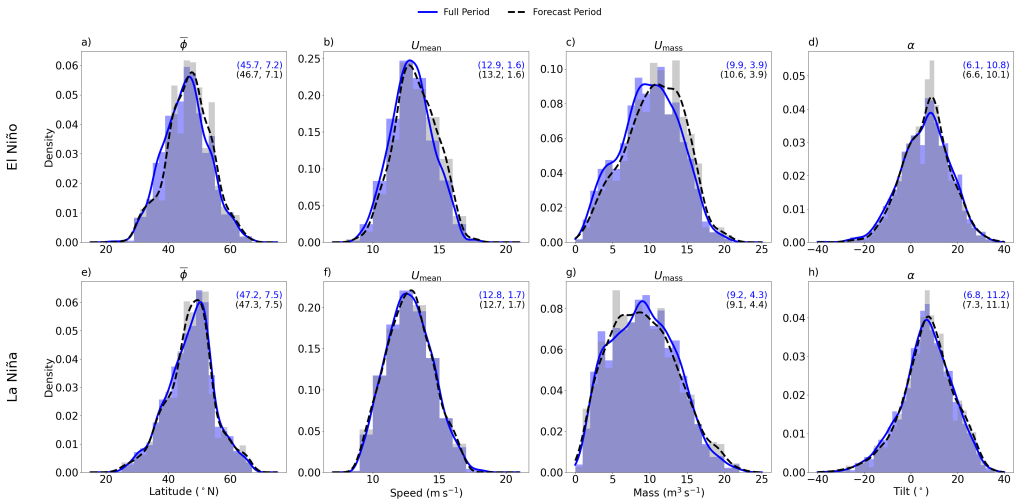

Figure 6.4: Distributions of $\overline{\phi}$ (a and e), U_{mean} (b and f), U_{mass} (c and g) and α (d and h) for El Niño years (top row) and La Niña (bottom row). Both the full period (blue) and the forecast period (black dashed line) are shown, with the mean and standard deviation given in the top right of each panel.

Early and late winter responses

I now focused on the intra-seasonal variability within each ENSO phase. To remove any seasonal cycle that would appear in the EDJ strength (which is known to reach its maximum in January to February (Woollings et al., 2018), I deseasonalise all data by removing the monthly climatology calculated from ERA5, from the ERA5 and also GloSea5 so they are compared against the same baseline and I can asess any systematic biases in the GloSea5.

Starting with ERA5, Figure 6.5 shows the deseasonalised distributions of the four EDJO diagnostics during El Niño (magenta) and La Niña (green) for early winter (ND) and late winter (JF). Starting with the anomalies of $\overline{\phi}$ (Figures 6.5a and e), both ENSO phases in ND are centred at zero, but La Niña exhibits a slightly larger spread ($\sigma_{\text{LN}} = 7.5°\text{N}$) than El Niño ($\sigma_{\text{EN}} = 6.6°\text{N}$), a difference of 0.9°. The two distributions also differ in shape: the El Niño histogram shows a weak bimodality with modes near $-4°\text{N}$ and $+9°\text{N}$, whereas the La Niña distribution is more unimodal, peaking around $+3°\text{N}$ and featuring a pronounced negative tail.

By JF, the EDJ during El Niño shifts equatorward ($\mu_{EN} = -0.4°$N) while in La Niña it has shifted poleward ($\mu_{LN} = 1.0°$N). El Niño variability remains larger ($\sigma_{\text{EN}} = 7.6°$N) than La Niña ($\sigma_{\text{LN}} = 7.2°$N), with a difference of 0.4°. The El Niño distribution retains its bimodal characteristic of JF, but now with peaks near −6°N and +3°N. It also shows an enhanced tail of extreme equatorward anomalies between −15° and −10°N. These higher order features underscore that beyond the mean shifts, ENSO imparts distinct changes in the full shape of the anomaly distribution of $\overline{\phi}$.

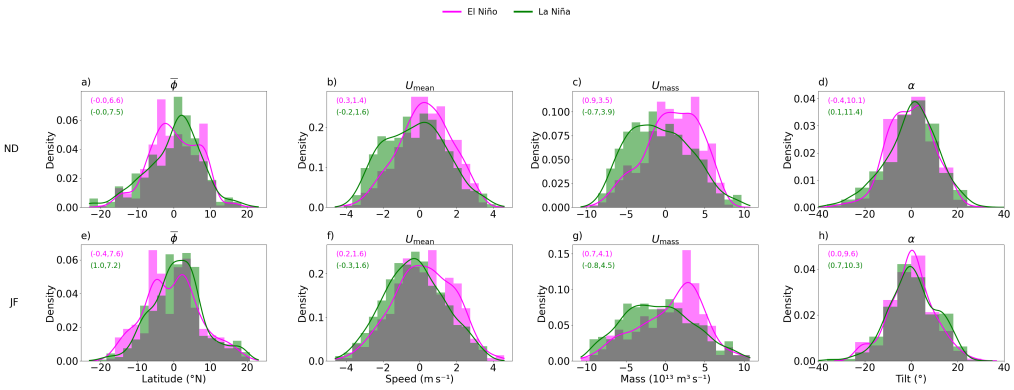

Figure 6.5: ERA5 Anomaly distributions of $\overline{\phi}$ (a and d), U_{mean} (b and e) and α (c and f) for November - December (top row) and January - February (bottom row) for El Niño years (pink) and La Niña years (green) for the hindcast period. The values in brackets in each panel are the mean and standard deviation coloured by the phases of ENSO.

Looking next at the EDJ strength, U_{mean} and U_{mass} (Figures 6.5b, c, f, and g), there is a robustly stronger EDJ during El Niño years that persists through ND into JF. In ND, the U_{mean} anomaly shifts by approximately $0.3\,\text{ms}^{-1}$ (El Niño composite peak at $1.4\,\text{ms}^{-1}$ versus La Niña at -1.6ms^{-1}) and the U_{mass} anomaly by $0.9\times10^{13}\,\text{m}^3\text{s}^{-1}$ (El Niño peak $3.5\times10^{13}\text{m}^3\text{s}^{-1}$ vs. La Niña $-3.9\times10^{13}\text{m}^3\text{s}^{-1}$). The JF composites exhibit a similar pattern: U_{mean} is stronger by $0.4\,\text{ms}^{-1}$ under El Niño (peak $1.6\,\text{ms}^{-1}$ vs. La Niña $-1.6\,\text{ms}^{-1}$), and U_{mass} by $0.7\times10^{13}\,\text{m}^3\text{s}^{-1}$ (peaks $4\times10^{13}\text{m}^3\text{s}^{-1}$ vs. La Niña $-4.5\times10^{13}\text{m}^3\text{s}^{-1}$). The increased strength seen in El Niño could be contributed to the fact that the EDJ is generally more equatorward during those years as seen in the $\overline{\phi}$ distribution and as shown in Chapter 3, poleward EDJs tended to have lower U_{mass} and U_{mean} and vice versa for equatorward EDJs.

Lastly, there is α (Figures 6.5d and h) where for ND, there is a sign that the EDJ is more zonal/negatively tilted for El Niño years than La Niña years with $\mu_{EN} = -0.4°$ and $\mu_{LN} = 0.1$. Moving to JF, there is a prominent shoulder at higher values of α for La Niña years, indicating a higher likelihood of tilted EDJ during those years. During El Niño years, α lies close to its climatological mean and shows reduced variability across the extended winter. The variability in α between the two phases can be linked to the relationship between α and the strength, whereby stronger EDJs display less variability in α and are more zonal, as shown in Chapter 3.

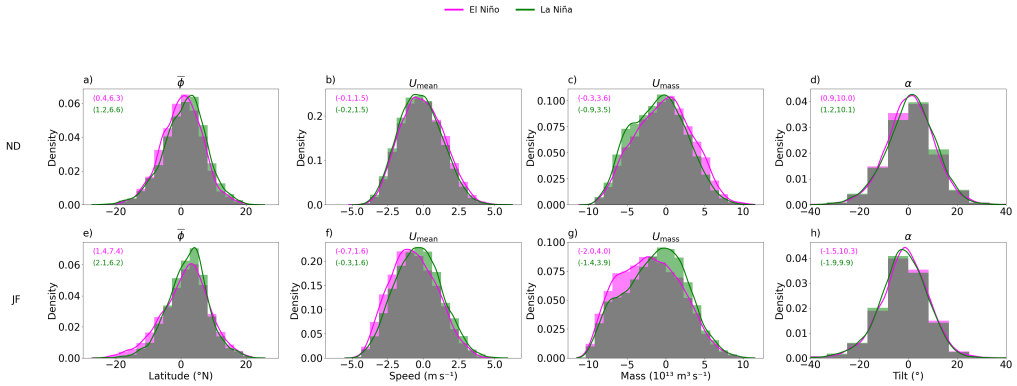

Figure 6.6: Same as Figure 6.5 but for GloSea5.

I then considered the anomalies in GloSea5 compared with the behaviour seen in ERA5. To accompany this, I have performed a KS-test on the ERA5 and GloSea5 distributions for each phase of ENSO and for the early and late winter. The test statistic (D) is shown in Table 6.1 where the values in bold indicate where the distributions exhibit a significant difference at the 95% level.

Figure 6.6 displays the $\overline{\phi}$ anomalies in GloSea5. In ND, both ENSO phases exhibit a modest poleward shift: the mean anomaly is $\mu_{\mathrm{EN}} = 0.4°\mathrm{N}$ during El Niño and $\mu_{\mathrm{LN}} = 1.2°\mathrm{N}$ during La Niña. In JF, this poleward displacement intensifies in both phases, reaching $\mu_{\mathrm{EN}} = 1.4°\mathrm{N}$ and $\mu_{\mathrm{LN}} = 2.1°\mathrm{N}$, the largest increase occurring under La Niña. The interseasonal change in the standard deviation for La Niña remains small ($|\Delta\sigma_{\mathrm{ND}\to\mathrm{JF}}| = 0.3°$), whereas El Niño shows a much larger variability increase ($|\Delta\sigma_{\mathrm{ND}\to\mathrm{JF}}| = 1.4°$). A similar magnitude of variability change is observed in ERA5, indicating that GloSea5 is capturing a similar change throughout the season.

Table 6.1: Table showing the Kolmogorov-Smirnov test statistic D for distributions of ND and JF for each phase of ENSO for each EDJO diagnostic. Values in bold indicate a significant difference ($p < 0.05$).

	$\overline{\phi}$	U_{mean}	U_{mass}	α
El Niño ND	0.06	**0.14**	**0.15**	0.08
El Niño JF	**0.17**	**0.24**	**0.31**	0.12
La Niña ND	0.04	0.06	0.06	0.06
La Niña JF	**0.11**	**0.03**	**0.07**	**0.12**

For U_{mean} and U_{mass}, the stronger ND jets in El Niño compared to La Niña found in ERA5 (Figures 6.5b,c) is reproduced in GloSea5 (Figures 6.6b,c), albeit at roughly half the magnitude ($\Delta\ U_{\text{mean}} = 0.15\text{ms}^{-1}$ vs. 0.3ms^{-1}), $\Delta\ U_{\text{mass}} = 0.3\times10^{13}\ \text{m}^3\ \text{s}^{-1}$ vs.$0.9\times10^{13}\text{m}^3\text{s}^{-1}$). In late winter (Figures 6.6f and g) the sign even reverses: La Niña jets become stronger than El Niño, not consistent with ERA5. Moreover, unlike ERA5 where the standard deviation for U_{mean} and U_{mass} increase by 0.3ms^{-1} and $1.4\text{m}^3\text{s}^{-1}$from ND to JF, in GloSea5 the variability are identical between ND and JF for both phases, an indication of potential uniform internal variability.

The anomalies for α, also reveal differences in the intraseasonal eveolution of the ENSO signal in GloSea5. GloSea5 produces a positive mean tilt in ND ($\mu_{EN} = 0.9°$, $\mu_{LN} = 1.2°$), then a complete reversal in JF ($\mu_{EN} = -1.5°$, $\mu_{LN} = -1.9°$), which was not observed in ERA5.

To further quantify these differences, Table 6.1 shows the test statistics values D for a KS test, where I have tested the respective distribution from GloSea5 to ERA5 and the values in bold indicate a significant difference ($p < 0.05$) from ERA5. What stands out is that for both phases of ENSO, the JF part of winter is significantly different across all variables. The only case where there is no difference is for ND in El Niño for $\overline{\phi}$ and α and for all variables in ND for La Niña. These results are interesting in the context of other work that has highlighted limitations in intraseasonal forecasting models (O'Reilly, 2025).

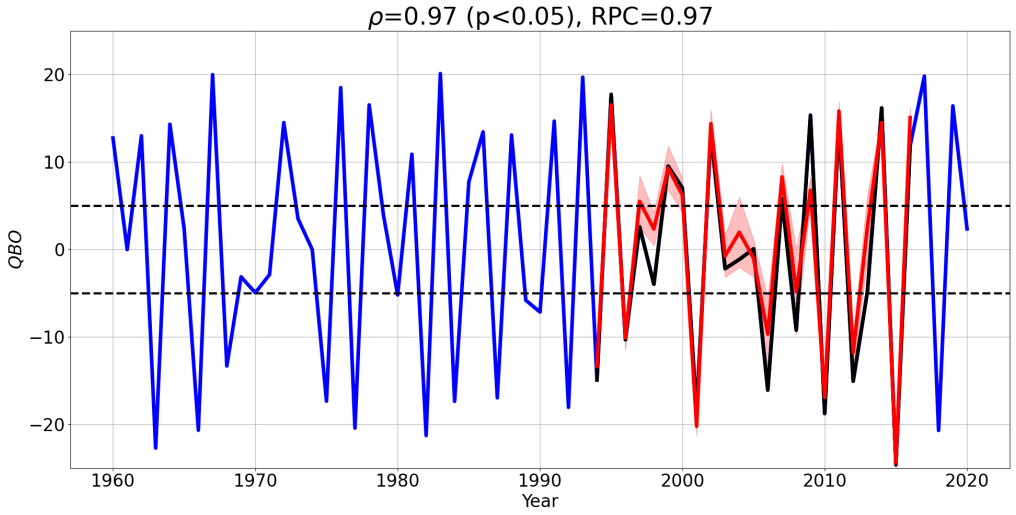

Figure 6.7: Same as Figure 6.3 but for the QBO with units of ms^{-1}. The black horizontal dashed line represents the thresholds for defining the QBO west and QBO east years.

6.3.2 Quasi-Biennial Oscillation

Figure 6.7 shows the QBO time series for the full period of ERA5 and the forecast period for ERA5 and GloSea5. This shows the QBO is very well represented for the forecast period in GloSea5 with a significantly high pearson correlation and an RPC close to one.

Sampling sensitivity

Following the analysis for ENSO, the NDJF distributions of the EDJO distributions are compared for the full and forecast periods for both phases of the QBO, shown in Figure 6.8. Starting with QBOe for $\overline{\phi}$ and calculating $SE_{\text{forecast}} = 1.5°\text{N}$, the mean shifts by only $\Delta\,\overline{\phi} = 0.5°\text{N}$; U_{mean} has $SE_{\text{forecast}} = 0.35\text{ms}^{-1}$ with $\Delta\,U_{\text{mean}}\,0.3ms^{-1}$; U_{mass} has $SE_{\text{forecast}} = 0.9 \times 10^{13}\text{m}^3\text{s}^{-1}$ with $\Delta\,U_{\text{mass}} = 0.8 \times 10^{13}\text{m}^3\text{s}^{-1}$; and for α the $SE_{\text{forecast}} = 2.25°$ with $\Delta\alpha = 0.6°$.

For QBOw, the full period $\overline{\phi}$ standard deviation $\sigma_{\overline{\phi}} = 7.1°\text{N}$ implies a forecast period $SE_{\text{forecast}} = 1.48°$ but the observed mean shift is only $\Delta\,\overline{\phi} = 0.1°$. Similarly, for U_{mean} the $SE_{\text{forecast}} = 0.35\text{ms}^{-1}$ with $\Delta\,U_{\text{mean}} = 0.01\text{ms}^{-1}$; U_{mass} produces a $SE_{\text{forecast}} = 0.88{\times}10^{13}\text{m}^3\text{s}^{-1}$ and with $\Delta\,U_{\text{mass}} = 0.03 \times 10^{13}\text{m}^3\text{s}^{-1}$; and for α, $SE_{\text{forecast}} = 2.3°$, with $\Delta\alpha = 0.2°$.

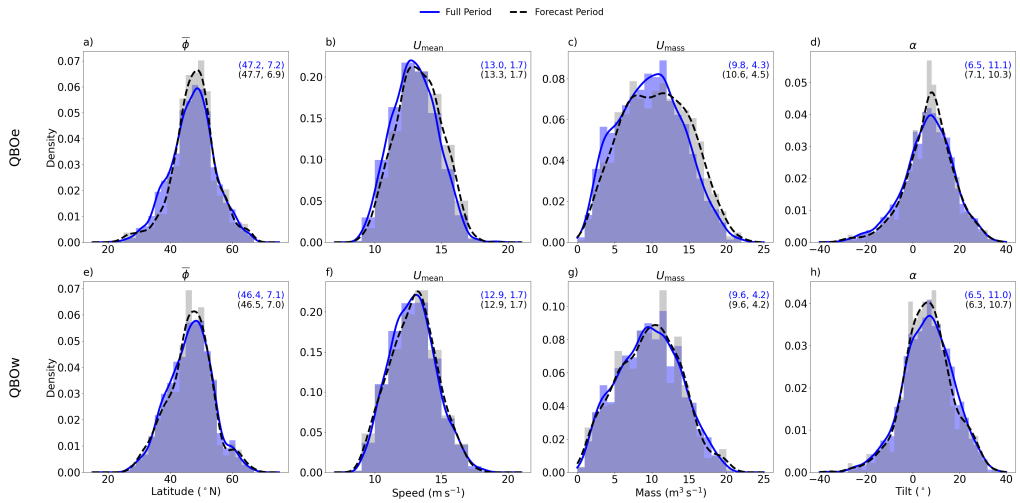

Figure 6.8: Same as Figure 6.5 but for the QBO.

Therefore the mean EDJ characteristics in ERA5 are not distinguishable between the hindcast and full periods.

Early and Late winter response

We now compare the distributions of the EDJO diagnostics seperately in ND and JF in ERA5 for each phase of the QBO. Starting with $\overline{\phi}$ (Figures 6.9a and e) there is a phase-dependent shift under each phase of the QBO. In ND, the QBOe EDJ is displaced poleward by $\mu_{\text{QBOe}} = 0.9°\text{N}$ (with $\sigma = 7.3°\text{N}$), while the QBOw winters are close to climatology ($\mu_{\text{QBOw}} = -0.1°$, $\sigma = 6.7°$). By JF, QBOe maintains the same anomaly as in ND ($\mu_{\text{QBOe}} = 0.9°\text{N}$) while in QBOw there is an equatorward EDJ shift with a negative anomaly of ($\mu_{\text{QBOw}} = -0.6°$). The spread under QBOw increases ($\sigma_{\text{QBOw}} = 7.3°$) while there is a decrease in variability in QBOe ($\sigma_{\text{QBOe}} = 5.9°$), indicating an increase in latitudinal variability during QBOw. In particular, the QBOe $\overline{\phi}$ histogram retains a slight secondary mode near $-5°\text{N}$ in ND which is gone in JF, while the QBOw distribution is more unimodal and symmetric in parts of winter.

Turning to the strength of the EDJ (Figure 6.9b, c, f and g), the anomalies of U_{mean} in ND are nearly identical in both phases ($\mu_{U_{\text{mean}}} = 0.1\,\text{m}\,\text{s}^{-1}$, $\sigma_{U_{\text{mean}}} = 1.6\,\text{m}\,\text{s}^{-1}$), and U_{mass} anomalies are similar ($\mu_{U_{\text{mass}}} = 0.2 \times 10^{13}\text{m}^3\text{s}^{-1}$ for QBOe and $\mu_{U_{\text{mass}}} = 0.1 \times 10^{13}\text{m}^3\text{s}^{-1}$ for QBOw, $\sigma = 4.0 \times$

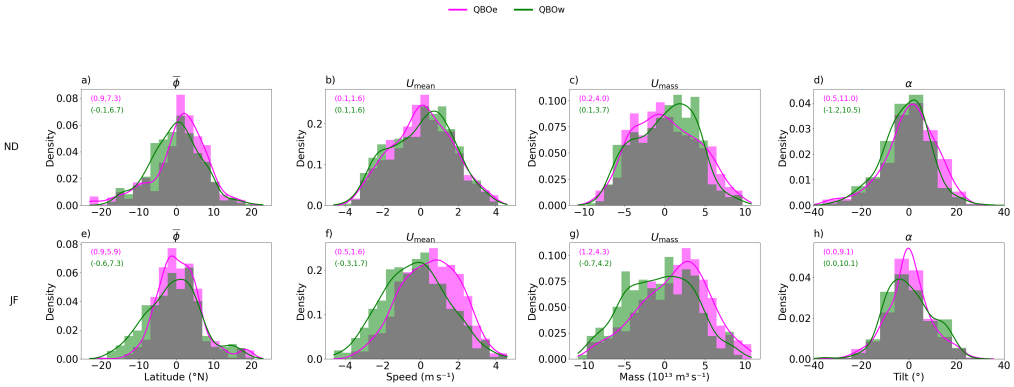

Figure 6.9: Same as Figure 6.5 but for the QBO, with QBOe in the top row and QBOw in the bottom row.

$10^{13}\mathrm{m}^3\mathrm{s}^{-1}$ vs. $3.7 \times 10^{13}\mathrm{m}^3\mathrm{s}^{-1}$).

By JF, the EDJ strengthens in QBOe ($\mu_{U_{\mathrm{mean}}} = 5\,\mathrm{m\,s}^{-1}$; $\mu_{U_{\mathrm{mass}}} = 1.2 \times 10^{13}\,\mathrm{m}^3\mathrm{s}^{-1}$) while in QBOw the EDJ anomaly weakens compared with ND ($\mu_{U_{\mathrm{mean}}} = -0.3\,\mathrm{m\,s}^{-1}$; $\mu_{U_{\mathrm{mass}}} = -0.7 \times 10^{13}\,\mathrm{m}^3\,\mathrm{s}^{-1}$). The variability in both U_{mean} and U_{mass} remains close to climatology throughout the winter.

Finally, jet tilt α (Figure 6.9d and h) shows differences during ND ($\mu_{\mathrm{QBOe}} = 0.5°$, $\mu_{QBOw} = -1.2°$) but by JF, both have returned back close to climatology.

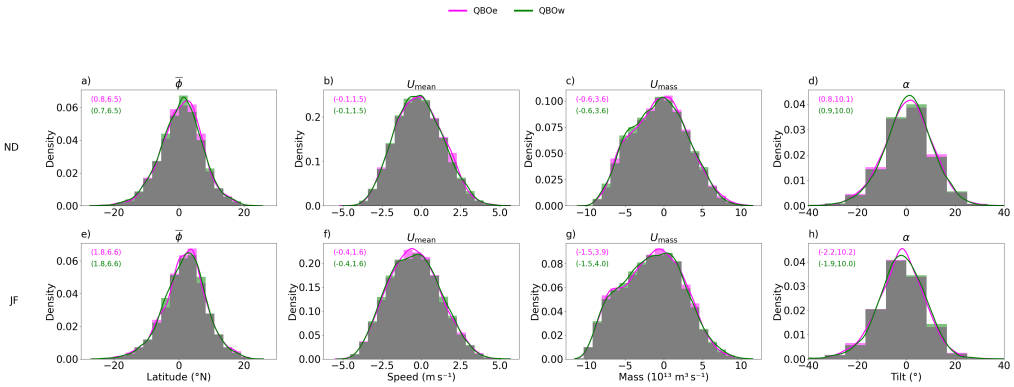

Figure 6.10: Same as Figure 6.6 but for the QBO

In GloSea5, the $\overline{\phi}$ distributions under QBOe and QBOw are virtually indistinguishable in both ND and JF. Both phases share almost identical means and variances for $\overline{\phi}$, U_{mean}, U_{mass}, and α, while in ERA5 each phase exhibits a clear phase-dependent mean change (for example, a 0.9°N poleward

shift in QBOe but a –0.1°N in QBOw in ND, that persists into JF). This underestimation of the teleconnection amplitude in GloSea5 is consistent with other work studying the NAO (Anstey et al., 2021; Scaife and Smith, 2018).

	$\overline{\phi}$	U_{mean}	U_{mass}	α
QBOe ND	0.06	0.14	0.15	0.08
QBOe JF	**0.13**	**0.24**	**0.27**	**0.14**
QBOw ND	0.06	0.11	0.12	0.09
QBOw JF	**0.17**	**0.06**	**0.11**	**0.09**

Table 6.2: Same as Table 6.1 but for the QBO.

Even with the lack of phase-dependence, I have still performed the KS test for the difference between ERA5 and GloSea5 distributions, with the results shown in 6.2. The results of the tests show that JF statistically different for both phases of the QBO, but ND is statistically similar.

6.4 Sub-seasonal variability associated with the MJO

6.4.1 NAO and MJO response

As shown in Cassou, 2008, there is a statistical relationship between the MJO and the NAO. In Figure 6.11, I show the contingency tables for NAO+ (green) and NAO- (pink). Here, it can be seen that there is a similar relationship for NAO as was found in Cassou, 2008, with a significant increase in the occurrence of NAO + 8 days after an active MJO in phase 3 that persists into phase 4 (Figures 6.11 c and d). The decreased occurrence of NAO- events can also be seen throughout these phases. The likelihood of NAO- events begins to rise roughly 13 days after a an active MJO in phase 6, and this enhanced occurrence carries through into phase 8 of the MJO life cycle (Figures 6.11f, g and h).

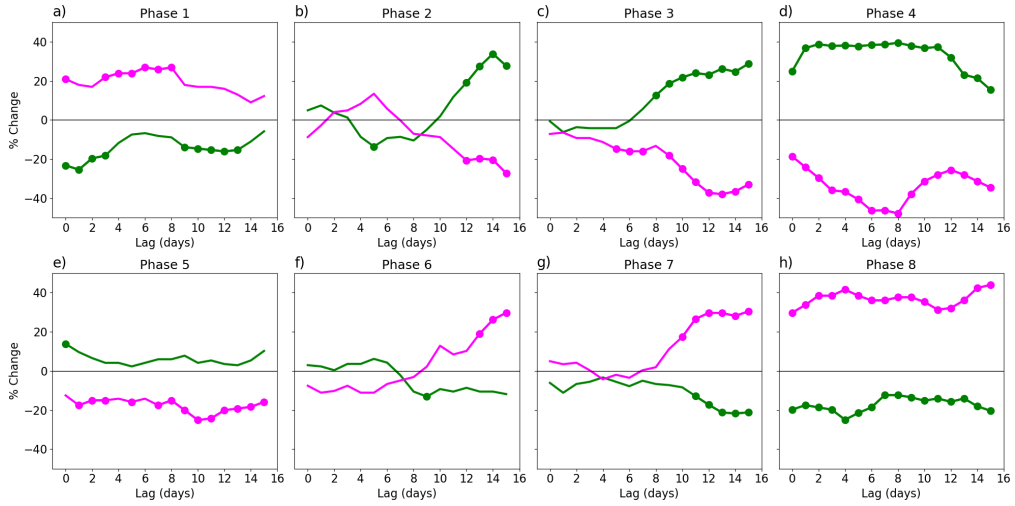

Figure 6.11: Contingency tables for the postive NAO (green) and the negative NAO (pink) for each phase of the MJO. Circles mark the lags that are significantly different from the climatology at the 95% level.

6.4.2 EDJ and MJO response

The results for $\overline{\phi}$, U_{mean}, U_{mass} and α are shown in Figures 6.12, 6.13, 6.14 and 6.15, respectively. In each plot, green lines represent the case for values greater than 1 and pink lines for values less than -1. Physically, this is interpreted as an increased likelihood of poleward or equatorward shifting of the EDJ for $\overline{\phi}$, stronger or weaker EDJ for U_{mean}, larger or smaller EDJ for U_{mass} and a tilted or zonal/negatively tilted EDJ for α.

Across each of the EDJ characteristics, there is a sign of a significant signal within the MJO phases. For $\overline{\phi}$ (Figure 6.12), there are significant changes in the phases with a similar timing to when there are changes in the NAO. There is a clear increase in the likelihood of an equatorward EDJ across all lags for phases 1 and 8 (Figures 6.12a and h), which matches the increased likelihood of NAO- events. This is reflected in the decreased likelihood of poleward EDJs within the same phases. The occurrence of EDJs begins to show significant decreases in phases 3-6 (Figures 6.12c, d and e), at lags of 5-16 days from the MJO phase onset

For poleward EDJs, the only phase showing increased occurrence is phase 6 (Figure 6.12f), where significant increases occur 5-10 days later. The decreased occurrences of poleward and equatorward EDJs in phases 2-4

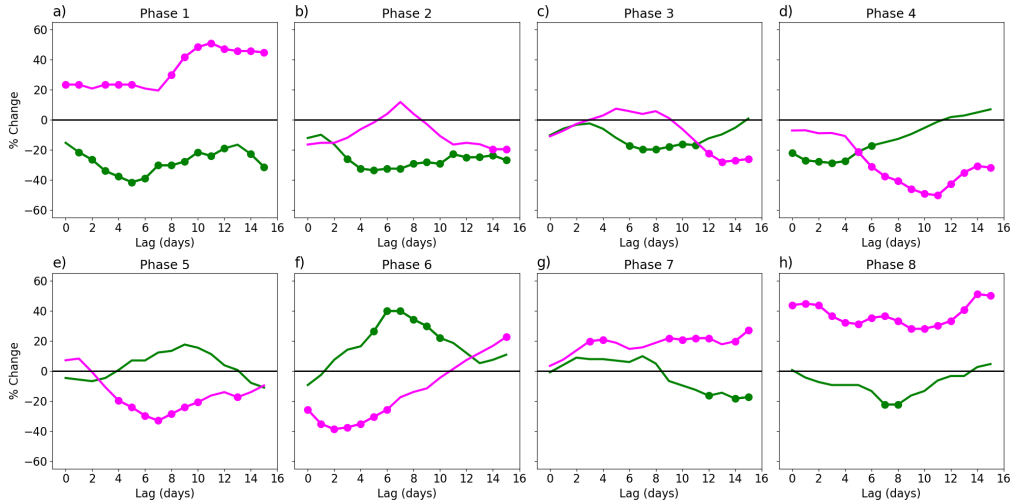

Figure 6.12: Contingency tables for the occurrence of days where the standardised $\overline{\phi}$ exceeds 1 (green) or is less than -1 (pink), for days when the MJO is active at different lags. Points with solid circles indicate significantly different from climatology at the 95% level.

(Figures 6.12b, c, and d) can be explained by what happens to the changes of U_{mean} (Figure 6.13) during the same phases. There is a clear increase in the occurrence of strong EDJs during phases 3 and 4 (Figure 6.13c and d), which is significant with a delay of 8-16 days for phase 3 and 0-10 days for phase 4. This increased occurrence of stronger EDJs accompanies the increased occurrence of NAO+ events. Hence, the lack of change in poleward or equatorward EDJs is due to having a much stronger EDJ, anchoring the EDJ at the given latitude.

The contingency tables for U_{mass} (Figure 6.14) echo the broad features seen in U_{mean}, yet several timing differences stand out. Most notably, a stronger EDJ emerges one phase earlier in U_{mass}, whereas U_{mean} the strengthening of the EDJ occurs in phases 3 and 4, There are already signs of a strengthening in U_{mass} in phase 2 (Figure 6.14b). This intensified signal remains significant across all lags in phase 3 (Figure 6.14c) and then weakens again in phase 4 (Figure 6.14d). A second difference appears in phase 6. Here, U_{mass} reveals a robust, all-lag signature of a smaller EDJ spanning from lags 3 to 16 (Figure 6.14f), a behaviour not seen in U_{mean}. The phases that feature a higher occurrence of stronger EDJs tend to show fewer instances of smaller jets, and vice-versa, with this contrast more pronounced in U_{mass}

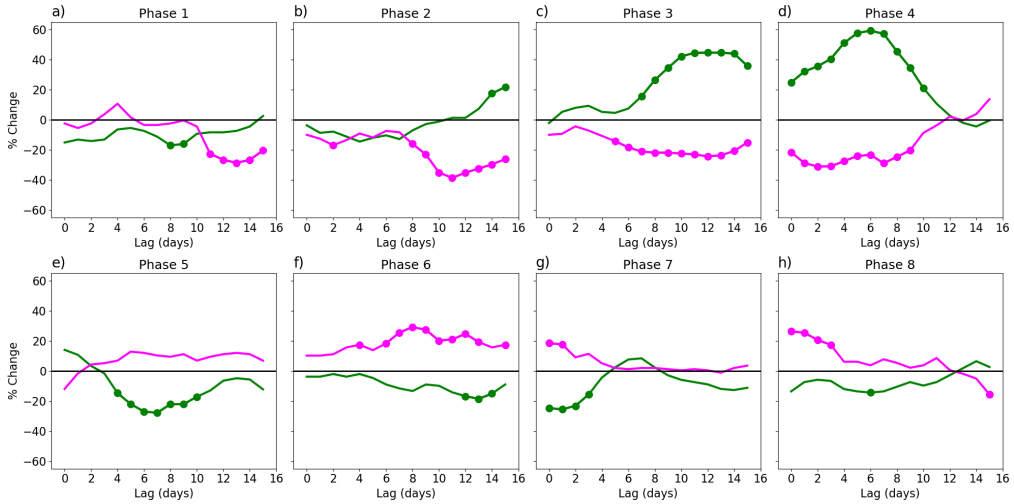

Figure 6.13: Same as Figure 6.12, but for U_{mean}.

than in U_{mean}. Taken together, these results imply that changes in EDJ size precede changes in overall strength.

Lastly α (Figure 6.15), exhibits more sporadic and phase-dependent changes compared to the other characteristics of EDJ. The only consistent sequence of lags occurs in phase 4 (Figure 6.15, where at lags 0-9, there is a decreased likelihood of a zonal/negatively tilted jet. There is also a sign of an increased likelihood of a tilted EDJ during phase 2 (Figure 6.15 b) for lags of 0-6 days.

6.5 Conclusions and Discussion

In this chapter, I have explored the effects of sources of seasonal and subseasonal variability on different EDJ characteristics. The two measures of seasonal variability I looked at were ENSO and the QBO, and for subseasonal the MJO. To investigate seasonal variability and its impacts, I use both ERA5 and GloSea5 to build up a larger sample of the different phases of ENSO and QBO for the extended winter of November - February (NDJF). The choice of NDJF is also made as it has been shown that there is interseasonal variability in the North Atlantic with the early winter (November and December) displaying an East Atlantic pattern (EA) signal and evolving into the North Atlantic Oscillation (NAO) into the late winter

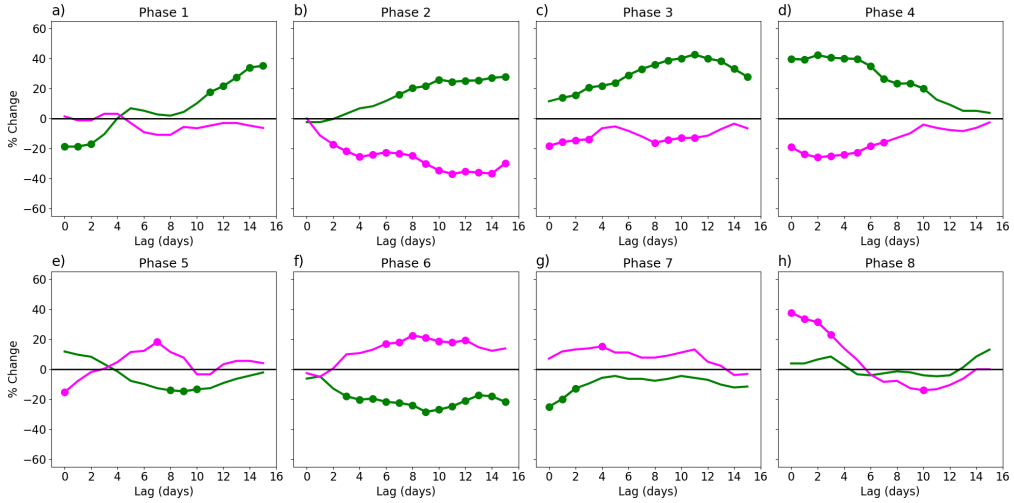

Figure 6.14: Same as Figure 6.12, but for U_{mass}.

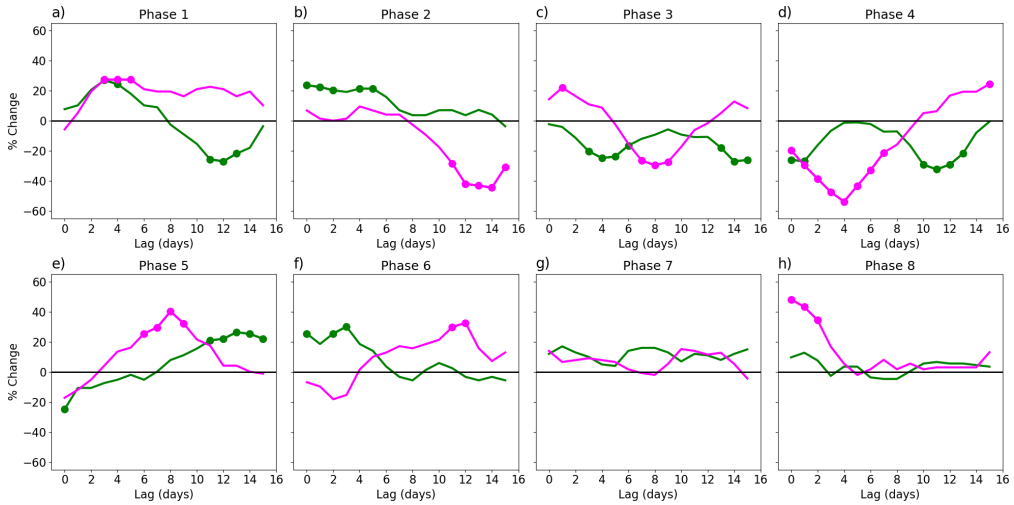

Figure 6.15: Same as Figure 6.12, but for α.

(January-February).

6.5.1 Seasonal variability

To investigate the differences in EDJ under different seasonal drivers, I combine $\overline{\phi}$, U_{mean}, U_{mass} and α in the respective phases of ENSO and QBO then divide them by early (ND) and late winter (JF). For each phase of both modes. I then remove the monthly climatology from every field so that both ERA5 and GloSea5 anomalies share the same baseline. This allows a direct, season-by-season assessment of how well GloSea5 reproduces the observed EDJ anomalies under each ENSO and QBO phase.

For ENSO, ERA5 exhibits pronounced intraseasonal variability in every EDJ metric. In El Niño winters, $\overline{\phi}$ distributions remain bimodal in both ND and JF (Figures 6.5 a and e) - initially peaking near $-4°$N and 9°N, then shifting equatorward to approximately $-6°$N and 3°N by JF. This equatorward shift is accompanied by increased variability and a pronounced negative tail in the JF, indicating a higher frequency of extreme equatorward jets. Conversely, La Niña jets display a unimodal distribution, moving consistently poleward from ND to JF, with fewer equatorward excursions. These findings underscore that ENSO modulates not only the mean jet position but also the likelihood of extreme latitudinal shifts, particularly equatorward extremes during El Niño late winters. The intraseasonal patterns are closely aligned with the changes in the JLI reported by O'Reilly et al., 2024.

For the EDJ strength measures (U_{mean} and U_{mass}), El Niño years consistently show stronger and larger jets throughout winter compared to La Niña years, with the strongest differences evident in early winter (ND). This strengthening aligns with the observed equatorward displacement, consistent with the findings presented in Chapter 3 where equatorward-shifted jets tend to be stronger. La Niña, in contrast, is characterised by weaker and poleward-shifted jets, particularly pronounced in late winter (JF). The tilt (α) also exhibits phase-dependent characteristics, with a higher tendency towards negatively tilted or zonal jets during El Niño and more positively tilted jets during La Niña, especially evident in JF. Inter-

estingly, the strongest difference for each ENSO phase is seen in U_{mass}, but no predictability was found for U_{mass} in Chapter 4 but there was for $\overline{\phi}$ even though GloSea5 does not appear to capture the equatorward shift seen in the late winter in $\overline{\phi}$.

GloSea5 generally captures the sign of ENSO-driven changes in the early winter; however, it struggles significantly in the late winter. In particular, GloSea5 tends to systematically bias $\overline{\phi}$ poleward in both phases of ENSO, fails to reproduce the increase in variability from ND to JF seen in ERA5, and reverses the observed relationship between ENSO phase and EDJ strength by the end of winter. These differences underscore a critical limitation of GloSea5 in representing intraseasonal variability linked to ENSO, which can affect forecast skill in the late winter months. This suggests a signal-to-noise issue (Scaife et al., 2014), where the ENSO teleconnection is strong enough in ND but does not persist through JF and hence does not capture the full range of variability as a result.

Turning to the QBO, I have shown in ERA5 a distinct phase-dependent impact on EDJ, which is in agreement Cai et al. (2022) who shows similar results in ERA5 but looking at differences in surface pressure. The QBOe phase is associated with a poleward and stronger EDJ that maintains its structure from early to late winter. Conversely, the QBOw phase exhibits an equatorward shift and weakening in the late winter. However, these clear distinctions in ERA5 are largely absent in GloSea5. The lack of phase dependence between QBO phases in GloSea5 likely arises from the single-level definition of the QBO that I have used in this study, where it has been shown in ensemble climate models that there are systematically weak QBO amplitudes at 50hPa (Anstey et al., 2021). To rectify this, this analysis would benefit from defining the QBO with multiple pressure levels that characterise the vertical structure, as shown in Gray et al. (2018) using an EOF-based approach. It is demonstrated that defining the QBO with multiple pressure levels using EOF analysis effectively captures its vertical structure, providing a more robust and consistent identification of QBO teleconnections compared to a single-level approach. This improved representation could address the weak QBO signal observed in GloSea5 and improve the detection of the associated EDJ variability.

6.5.2 Sub-seasonal variability

The final part of this chapter focused on subseasonal variability and its impacts on EDJ in the North Atlantic. Here I analysed the relationship in ERA5, however data was not available to assess this in GloSea5 as well. I chose to include the months of March and April in this analysis to capture the effect of the MJO moving into spring, as is done in Cassou (2008) and Skinner et al. (2022).

I perform a lead-lag analysis within each MJO phase and look for a significant change in the occurrence of events of either greater or less than 1 standard deviation of the standardised EDJ characteristic. Physically for each component of the EDJ, this relates to a poleward (equatorward) shift in $\overline{\phi}$, a stronger (weaker) jet in U_{mean}, larger (smaller) in U_{mass} and tilted (zonal/negatively tilted) in α for larger than 1 standard deviation (smaller than -1 standard deviation). I have shown that different EDJ characteristics change in different phases of the MJO.

Phases 1 and 8 of the MJO enhance the equatorward shifts in $\overline{\phi}$ at later lags, whilst phases 2-4 there is an increase in the likelihood of stronger and larger EDJs. This work directly links with the variations in the NAO, but has broken down which components of the EDJ are changing in the different phases. Interestingly, there is no phase where there is a consistent increase in poleward shifting of the EDJ, to the same degree to which equatorward shifting has been observed. This appears to be manifesting as an increase in the size and strength of the EDJ, since the phases that have been shown to see an increased likelihood of positive NAO events match the phases where there is an increase in both U_{mean} and U_{mass}. The signal seen in U_{mass} differs slightly from U_{mean}, with significant differences occurring in earlier phases than in U_{mean}.

Chapter 7

Conclusions and Further Work

In this thesis I have examined the characteristics of the variability and predictability of the North Atlantic EDJ, and its relationship to surface climate parameters. This has been achieved utilising a new methodology to characterise the jet structure using 2-dimensional moment analysis applied to the lower tropospheric zonal wind field presented in Chapter 3. This framework characterises multiple diagnostics including jet tilt and jet mass and offers a more nuanced representation of high frequency jet variability compared with some earlier approaches.

The key insights from this are:

- The moment-based approach provides an improved and robust characterisation of the EDJ latitude ($\overline{\phi}$), strength (U_{mean}) and tilt (α). The approach also allows for the classification of split jet days.
- From the results of the moment-based methodology, the trimodal regimes of the JLI are called into question particularly the northern regime, which is shown to contain days when the EDJ is split, tilted, or displays a broad profile.
- Temporal analyses demonstrate that EDJOs more accurately capture the persistence and transitional behaviours of the jet, leading to a deeper understanding of its variability. This analysis also shows that transitions between regimes of the JLI can be sensitive to local changes in the zonal wind field and do not consistently reflect changes

in the large-scale structure of the EDJ.

- The moment-based EDJ metrics exhibit stronger correlations with large-scale climate drivers, particularly the NAO and the EA pattern, than the JLI and JAI. Interestingly, the mass-weighted strength (U_{mass}) shows a stronger correlation with the EA pattern than the averaged strength (U_{mean}), indicating a stronger link between the size and strength of the EDJ and the EA pattern.

In Chapter 4, I explored the seasonal predictability of the EDJ using the GloSea5 seasonal forecasting system. The evaluation revealed key biases and varying levels of predictability in different EDJ metrics.

- At lead times of 1-5 months, GloSea5 simulates the winter mean and variability of the EDJ latitude, tilt and strength relatively well with no significant biases compared with ERA5 reanalysis.

- GloSea5 shows significant biases in the relationship between the moment-based EDJ metrics and the NAO and EA pattern. Specifically for $\overline{\phi}$ the correlation with the NAO is too weak and the anticorrelation with the EA pattern is too strong.

- Seasonal predictability at lead times of 1-5 months (November - February) is only found for $\overline{\phi}$. An RPC greater than 1, indicates model overconfidence in $\overline{\phi}$ agreeing with other studies on the predictability of the NAO and the EA pattern (Scaife et al., 2014; Thornton et al., 2023).

In Chapter 5, I looked at different moment-based EDJ configurations and explored their relationships to impacts on the surface climate variables (precipitation and 2m air temperature) in the EDJO framework. Key findings include:

- EDJ latitude ($\overline{\phi}$) has a significant influence on precipitation patterns in Europe, with poleward shifts correlating with wetter northern conditions.

- Strong correlations were identified between the EDJ metrics and anomalies of T2m, providing information on the dynamics of temperature extremes.

- Multiple combinations of the moment-based EDJ metrics revealed unique patterns of extremes in T2m and P fields.
- Although GloSea5 captured general spatial patterns of precipitation and temperature anomalies, it systematically underestimated their magnitudes.
- The analyses of extreme events over the UK revealed variability in jet latitude and strength during wet and dry periods, with GloSea5 capturing only partial aspects of these dynamics.

In Chapter 6, I explored the role of seasonal and subseasonal drivers of variability in the North Atlantic EDJ, including the ENSO, QBO, and MJO. Key findings include:

- ENSO phases modulate EDJ characteristics significantly, though GloSea5 displayed notable biases in its late winter representations. In particular in the late winter during El Niño years, there is a clear bimodality in the distribution of $\overline{\phi}$ that is not captured in GloSea5.
- GloSea5 struggles to capture the late winter EDJ teleconnections, with significant differences in each EDJ characteristic. Both U_{mean} and U_{mass} show significant differences in the early and late winter periods in GloSea5 for both QBO and ENSO.
- The MJO exerts phase-dependent impacts on latitude ($\overline{\phi}$), strength (U_{mean} and U_{mass}), and tilt (α). This analysis breaks down the understanding of the similar analysis performed looking at the NAO, where each phase of the MJO exerts a slightly different change in the EDJ in the North Atlantic. In particular, phases 1 and 8 of the MJO are associated with an increased likelihood of equatorward shifting of the EDJ, and phases 2-4 with an increased likelihood of above average strength of the EDJ.

My work in this thesis has helped to further the field by providing a novel two-dimensional object-based framework for characterising the North Atlantic EDJ, overcoming the limitations of the traditional zonal mean indices and capturing the spatial structure of the EDJ, in more detail than some earlier methods. This new approach also highlighted specific cases that

zonal-mean indices struggle to identify, such as tilted and broad EDJs. In addition, robust links between surface climate and different configurations of the EDJ have been shown based on the new moment-based metrics. Further to this I have shown that the persistence of the EDJ is larger than previously shown through comparisons of autocorrelation functions between the JLI and the EDJOs. I have also been able to characterise different types of EDJ structures such as broad and tilted jets where approximately 20% of winter days have an EDJ that is negatively tilted.

Furthermore, by evaluating GloSea5, I have demonstrated that it is capable of predicting the EDJ latitude, but struggles with the tilt and the strength. Within this, I also highlight a signal-to-noise issue with the predictions of EDJ latitude, whereby GloSea5 is overconfident in its forecast. I also show that there is a mismatch between the links between the EDJ latitude and strength with the NAO and the EA, where the correlation between the EA with the latitude and the NAO with the speed is statistically too strong in the model when compared to ERA5. This raises questions over whether the predictability in latitude that was shown is being produced for the wrong reasons, with the EA driving variations in the latitude where it is known that the NAO that typically drives this (Parker et al., 2019).

I also quantify how major remote drivers like ENSO, the QBO, and the MJO modulate jet behaviour on subseasonal to seasonal timescales, ultimately providing a more comprehensive, multidimensional understanding of mid-latitude EDJ.

7.1 Further Work

With regard to methodology, the choice of flood parameter U_{crit}, has been chosen to be 8ms^{-1} from the testing of the wind speed values at the grid point during winter seen in other studies (Woollings et al., 2010). However this choice is really only suited for the winter and would not be a good choice if one wanted to study the EDJ over diferent seasons. Exploring a temporally or seasonally varying parameter, such as the daily averaged positive zonal winds or a seasonal parameter, would be interesting to assess the EDJOs over different seasons and answer questions such as: in what

season do the highest occurrence of multiple EDJOs occur?

There is also the choice of domain and region; here I have specifically focused on the North Atlantic because of the unique trimodal structure of the JLI there. Exploring other domains with the EDJOs may provide insights between the connection between the Pacific and North Atlantic EDJs, or differences in the spatial distributions within each region, which may provide new insights on the regional variability with the use of the EDJOs. There is also the potential for the methodology to not be domain-specific and instead be applied globally or hemispherically, allowing for no restriction on the size or location of the EDJOs. This would require a modification to the assigning of points to an EDJO, to account for the periodicity of Earth.

In terms of the predictability of the EDJ, the first step would be to increase the ensemble size to improve the confidence in the results that were shown in Chapter 4. Similarly, there are questions about how different initialisations may affect predictability, as shown in Thornton et al. (2023),

The predictability of the main modes of variability in the North Atlantic changes from the EA pattern in early winter for initialisations in October to the NAO in the late winter for initialisations in November. This would be interesting to explore from an EDJ perspective to see how the predictability of the different characteristics may change with different forecast initialisation dates. Deficiencies in the representation of the EDJ in GloSea5 were also shown. Trying to explain these features in terms of a dynamical mechanism in the model, such as the eddy-momentum flux or the baroclinicity, that contribute to the model biases would be important to improve the representation of the EDJ.

The surface impacts highlighted how spatially varied P and T2m are with respect to each characteristic of the EDJ individually and in combination. The next steps in this work would be to understand how these configurations affect the transport of extratropical cyclones. This is important because it would tie together the low-frequency and high-frequency variability, helping to improve the understanding of not only the link between temporal scales but also the variability in P and T2m. This could, for

example help with understanding serial clustering of cyclones, with a more in-depth measure of the different EDJ characteristics, and provide insight into the ideal EDJ conditions that lead to serial clustering.

The work on teleconnections could be extended by accounting for compounding affects. For example, it has been shown in the literature that the MJO teleconnection to the North Atlantic is modified by both the ENSO and QBO phases (Feng and Lin, 2019; Lee et al., 2020). This may lead to unique EDJ configurations, which in turn would lead to different impacts over Europe. Accounting for compounding affects would further improve our understanding of the connection between seasonal and subseasonal modes of variability and how the associated impacts of P and T2m are forecast.

References

Andrews, D. G., & McIntyre, M. E. (1976). Planetary Waves in Horizontal and Vertical Shear: The Generalized Eliassen-Palm Relation and the Mean Zonal Acceleration. *Journal of the Atmospheric Sciences*, *33*(11), 2031–2048. https://doi.org/10.1175/1520-0469(1976)033⟨2031:pwihav⟩2.0.co;2

Anstey, J. A., Simpson, I. R., Richter, J. H., Naoe, H., Taguchi, M., Serva, F., Gray, L. J., Butchart, N., Hamilton, K., Osprey, S., Bellprat, O., Braesicke, P., Bushell, A. C., Cagnazzo, C., Chen, C.-C., Chun, H.-Y., Garcia, R. R., Holt, L., Kawatani, Y., ... Yukimoto, S. (2021). Teleconnections of the Quasi-Biennial Oscillation in a multi-ensemble of QBO-resolving models. *Quarterly Journal of the Royal Meteorological Society*, *148*(744), 1568–1592. https://doi.org/10.1002/qj.4048

Ayarzagüena, B., Barriopedro, D., Garrido-Perez, J. M., Abalos, M., de la Cámara, A., García-Herrera, R., Calvo, N., & Ordóñez, C. (2018). Stratospheric Connection to the Abrupt End of the 2016/2017 Iberian Drought. *Geophysical Research Letters*, *45*(22). https://doi.org/10.1029/2018gl079802

Baker, L. H., Shaffrey, L. C., Sutton, R. T., Weisheimer, A., & Scaife, A. A. (2018). An Intercomparison of Skill and Overconfidence/Underconfidence of the Wintertime North Atlantic Oscillation in Multimodel Seasonal Forecasts. *Geophysical Research Letters*, *45*(15), 7808–7817. https://doi.org/https://doi.org/10.1029/2018GL078838

Baldwin, M. P., Gray, L. J., Dunkerton, T. J., Hamilton, K., Haynes, P. H., Randel, W. J., Holton, J. R., Alexander, M. J., Hirota, I., Horinouchi, T., Jones, D. B. A., Kinnersley, J. S., Marquardt, C., Sato, K., & Takahashi, M. (2001). The Quasi-Biennial Oscillation. *Reviews of Geophysics*, *39*(2), 179–229. https://doi.org/10.1029/1999rg000073

Barriopedro, D., Ayarzagüena, B., García-Burgos, M., & García-Herrera, R. (2022). A multi-parametric perspective of the North Atlantic eddy-driven jet. *Climate Dynamics*. https://doi.org/10.1007/s00382-022-06574-w

Brayshaw, D. J., Hoskins, B., & Blackburn, M. (2009). The Basic Ingredients of the North Atlantic Storm Track. Part I: Land–Sea Contrast and Orography. *Journal of the Atmospheric Sciences*, *66*(9), 2539–2558. https://doi.org/10.1175/2009jas3078.1

Butler, A. H., Polvani, L. M., & Deser, C. (2014). Separating the stratospheric and tropospheric pathways of El Niño–Southern Oscillation teleconnections. *Environmental Research Letters*, *9*(2), 024014. https://doi.org/10.1088/1748-9326/9/2/024014

Cai, Q., Ma, T., Chen, W., Wei, K., Pogoreltsev, A. I., & Koval, A. V. (2022). The observed connection between the Quasi-Biennial Oscillation and the persistence of the North Atlantic Oscillation in boreal winter. *International Journal of Climatology*, *42*(16), 8777–8791. https://doi.org/10.1002/joc.7769

Cassou, C. (2008). Intraseasonal interaction between the Madden–Julian Oscillation and the North Atlantic Oscillation. *Nature*, *455*(7212), 523–527. https://doi.org/10.1038/nature07286

Ceppi, P., Zelinka, M. D., & Hartmann, D. L. (2014). The response of the Southern Hemispheric eddy-driven jet to future changes in shortwave radiation in CMIP5. *Geophysical Research Letters*, *41*, 3244–3250. https://doi.org/10.1002/2014GL060043

Charlton-Perez, A. J., Ferranti, L., & Lee, R. W. (2018). The influence of the stratospheric state on North Atlantic weather regimes. *Quarterly Journal of the Royal Meteorological Society*, *144*(713), 1140–1151. https://doi.org/10.1002/qj.3280

Charney, J. G. (1947). The Dynamics of Long Waves in a Baroclinic Westerly Current. *Journal of Meteorology*, *4*(5), 136–162. https://doi.org/10.1175/1520-0469(1947)004⟨0136:tdolwi⟩2.0.co;2

Charney, J. G., & Drazin, P. G. (1961). Propagation of planetary-scale disturbances from the lower into the upper atmosphere. *Journal of Geophysical Research*, *66*(1), 83–109. https://doi.org/10.1029/jz066i001p00083

Charney, J. G., & DeVore, J. G. (1979). Multiple Flow Equilibria in the Atmosphere and Blocking. *Journal of the Atmospheric Sciences*, *36*(7), 1205–1216. https://doi.org/10.1175/1520-0469(1979)036⟨1205:mfeita⟩2.0.co;2

Charney, J. G., & Straus, D. M. (1980). Form-Drag Instability, Multiple Equilibria and Propagating Planetary Waves in Baroclinic, Orographically Forced, Planetary Wave Systems. *Journal of the Atmospheric Sciences*, *37*(6), 1157–1176. https://doi.org/10.1175/1520-0469(1980)037⟨1157:fdimea⟩2.0.co;2

Christiansen, B. (2007). Atmospheric Circulation Regimes: Can Cluster Analysis Provide the Number? *Journal of Climate*, *20*(10), 2229–2250. https://doi.org/10.1175/jcli4107.1

Crommelin, D. T. (2003). Regime Transitions and Heteroclinic Connections in a Barotropic Atmosphere. *Journal of the Atmospheric Sciences*, *60*(2), 229–246. https://doi.org/10.1175/1520-0469(2003)060⟨0229:rtahci⟩2.0.co;2

Crommelin, D. T., Opsteegh, J. D., & Verhulst, F. (2004). A Mechanism for Atmospheric Regime Behavior. *Journal of the Atmospheric Sci-*

ences, *61*(12), 1406–1419. https://doi.org/10.1175/1520-0469(2004)061⟨1406:amfarb⟩2.0.co;2

Cullen, M., & Brown, A. (2009). Large eddy simulation of the atmosphere on various scales. *Philosophical Transactions of the Royal Society A: Mathematical, Physical and Engineering Sciences*, *367*(1899), 2947–2956. https://doi.org/10.1098/rsta.2008.0268

Di Capua, G., & Coumou, D. (2016). Changes in meandering of the Northern Hemisphere circulation. *Environmental Research Letters*, *11*(9), 094028. https://doi.org/10.1088/1748-9326/11/9/094028

Dorrington, J., & Strommen, K. J. (2020). Jet Speed Variability Obscures Euro-Atlantic Regime Structure. *Geophysical Research Letters*, *47*(15). https://doi.org/10.1029/2020gl087907

Duchon, C. E. (1979). Lanczos Filtering in One and Two Dimensions. *Journal of Applied Meteorology and Climatology*. https://doi.org/10.1175/1520-0450(1979)018⟨1016:lfioat⟩2.0.co;2

Dunstone, N., Smith, D., Scaife, A., Hermanson, L., Eade, R., Robinson, N., Andrews, M., & Knight, J. (2016). Skillful predictions of the winter North Atlantic Oscillation one year ahead. *Nature Geoscience*, *9*(11), 809–814. https://doi.org/10.1038/ngeo2824

Eade, R., Smith, D., Scaife, A., Wallace, E., Dunstone, N., Hermanson, L., & Robinson, N. (2014). Do seasonal-to-decadal climate predictions underestimate the predictability of the real world? *Geophysical Research Letters*, *41*(15), 5620–5628. https://doi.org/10.1002/2014gl061146

Eady, E. T. (1949). Long Waves and Cyclone Waves. *Tellus*, *1*(3), 33–52. https://doi.org/10.3402/tellusa.v1i3.8507

Edmon, H. J., Hoskins, B. J., & McIntyre, M. E. (1980). Eliassen-Palm Cross Sections for the Troposphere. *Journal of the Atmospheric Sciences*, *37*(12), 2600–2616. https://doi.org/10.1175/1520-0469(1980)037⟨2600:epcsft⟩2.0.co;2

Fabiano, F., Christensen, H., Strommen, K., Athanasiadis, P., Baker, A. J., Schiemann, R., & Corti, S. (2020). Euro-atlantic weather regimes in the primavera coupled climate simulations: Impact of resolution and mean state biases on model performance. *Climate Dynamics*. https://doi.org/10.1007/s00382-020-05271-w

Falkena, S. K., Wiljes, J., Weisheimer, A., & Shepherd, T. G. (2020). Revisiting the identification of wintertime atmospheric circulation regimes in the Euro-Atlantic sector. *Quarterly Journal of the Royal Meteorological Society*, *146*(731), 2801–2814. https://doi.org/10.1002/qj.3818

Feng, P.-N., & Lin, H. (2019). Modulation of the MJO-Related Teleconnections by the QBO. *Journal of Geophysical Research: Atmospheres*, *124*(22), 12022–12033. https://doi.org/10.1029/2019jd030878

Frame, T. H. A., Ambaum, M. H. P., Gray, S. L., & Methven, J. (2011). Ensemble prediction of transitions of the North Atlantic eddy-driven jet. *Quarterly Journal of the Royal Meteorological Society*, *137*(658), 1288–1297. https://doi.org/https://doi.org/10.1002/qj.829

Franzke, C., Woollings, T., & Martius, O. (2011). Persistent Circulation Regimes and Preferred Regime Transitions in the North Atlantic. *Journal of the Atmospheric Sciences*, *68*(12), 2809–2825. https://doi.org/10.1175/jas-d-11-046.1

Fyfe, J. C., & Lorenz, D. J. (2005). Characterizing midlatitude jet variability: Lessons from a simple GCM. *Journal of Climate*, *18*, 3400–3404. https://doi.org/10.1175/JCLI3486.1

García-Burgos, M., Ayarzagüena, B., Barriopedro, D., & García-Herrera, R. (2023). Jet Configurations Leading to Extreme Winter Temperatures Over Europe. *Journal of Geophysical Research: Atmospheres*, *128*(24). https://doi.org/10.1029/2023jd039304

Garfinkel, C. I., Feldstein, S. B., Waugh, D. W., Yoo, C., & Lee, S. (2012). Observed connection between stratospheric sudden warmings and

the Madden-Julian Oscillation. *Geophysical Research Letters*, *39*(18). https://doi.org/10.1029/2012gl053144

Gray, L. J., Anstey, J. A., Kawatani, Y., Lu, H., Osprey, S., & Schenzinger, V. (2018). Surface impacts of the Quasi Biennial Oscillation. *Atmospheric Chemistry and Physics*, *18*(11), 8227–8247. https://doi.org/10.5194/acp-18-8227-2018

Greening, K., & Hodgson, A. (2019). Atmospheric analysis of the cold late February and early March 2018 over the UK. *Weather*, *74*(3), 79–85. https://doi.org/10.1002/wea.3467

Hannachi, A., Woollings, T., & Fraedrich, K. (2011). The North Atlantic jet stream: a look at preferred positions, paths and transitions. *Quarterly Journal of the Royal Meteorological Society*, *138*(665), 862–877. https://doi.org/10.1002/qj.959

Hardiman, S. C., Dunstone, N. J., Scaife, A. A., Smith, D. M., Ineson, S., Lim, J., & Fereday, D. (2019). The Impact of Strong El Niño and La Niña Events on the North Atlantic. *Geophysical Research Letters*, *46*, 2874–2883. https://doi.org/10.1029/2018GL081776

Hardiman, S. C., Dunstone, N. J., Scaife, A. A., Smith, D. M., Comer, R., Nie, Y., & Ren, H.-L. (2022). Missing eddy feedback may explain weak signal-to-noise ratios in climate predictions. *npj Climate and Atmospheric Science*, *5*(1). https://doi.org/10.1038/s41612-022-00280-4

Hartmann, D. L. (2016). Atmospheric General Circulation and Climate. In *Global physical climatology* (pp. 159–193). Elsevier. https://doi.org/10.1016/b978-0-12-328531-7.00006-2

Hersbach, H., Bell, B., Berrisford, P., Hirahara, S., Horányi, A., Muñoz-Sabater, J., Nicolas, J., Peubey, C., Radu, R., Schepers, D., Simmons, A., Soci, C., Abdalla, S., Abellan, X., Balsamo, G., Bechtold, P., Biavati, G., Bidlot, J., Bonavita, M., ... Thépaut, J.-N. (2020). The ERA5 global reanalysis. *Quarterly Journal of the Royal Mete-*

orological Society, *146*(730), 1999–2049. https://doi.org/10.1002/qj.3803

Holton, J. R., & Hakim, G. J. (2013). *An Introduction to Dynamic Meteorology (Fifth Edition)* (Fifth Edition). Academic Press. https://doi.org/https://doi.org/10.1016/B978-0-12-384866-6.00012-X

Holton, J. R., & Tan, H.-C. (1980). The Influence of the Equatorial Quasi-Biennial Oscillation on the Global Circulation at 50 mb. *Journal of the Atmospheric Sciences*, *37*(10), 2200–2208. https://doi.org/10.1175/1520-0469(1980)037⟨2200:tioteq⟩2.0.co;2

Hoskins, B. J., & Karoly, D. J. (1981). The Steady Linear Response of a Spherical Atmosphere to Thermal and Orographic Forcing. *Journal of the Atmospheric Sciences*, *38*(6), 1179–1196. https://doi.org/10.1175/1520-0469(1981)038⟨1179:tslroa⟩2.0.co;2

Ineson, S., Dunstone, N. J., Scaife, A. A., Andrews, M. B., Lockwood, J. F., & Pang, B. (2023). Statistics of sudden stratospheric warmings using a large model ensemble. *Atmospheric Science Letters*, *25*(3). https://doi.org/10.1002/asl.1202

Keel, T., Brierley, C., & Edwards, T. (2024). jsmetrics v0.2.0: a Python package for metrics and algorithms used to identify or characterise atmospheric jet streams. *Geoscientific Model Development*, *17*(3), 1229–1247. https://doi.org/10.5194/gmd-17-1229-2024

Kerzenmacher, T. (2025). Time–height section of monthly mean zonal winds (m/s) at equatorial stations: Canton Island, 3S/172W (Jan 1953–Aug 1967), Gan/Maledive Islands, 1S/73E (Sep 1967–Dec 1975) and Singapore, 1N/104E (since Jan 1976). Isopleths at 10 m/s intervals; westerlies shaded (updated from Naujokat, 1986) [Last updated 2025-05-09; accessed 2025-05-30].

Knight, J., Scaife, A., Bett, P. E., Collier, T., Dunstone, N., Gordon, M., Hardiman, S., Hermanson, L., Ineson, S., Kay, G., McLean, P., Pilling, C., Smith, D., Stringer, N., Thornton, H., & Walker, B.

(2020). Predictability of European Winters 2017/2018 and 2018/2019: Contrasting influences from the Tropics and stratosphere. *Atmospheric Science Letters*, *22*(1). https://doi.org/10.1002/asl.1009

Koch, P., Wernli, H., & Davies, H. C. (2006). An event-based jet-stream climatology and typology. *International Journal of Climatology*, *26*(3), 283–301. https://doi.org/https://doi.org/10.1002/joc.1255

Lee, J. C. K., Lee, R. W., Woolnough, S. J., & Boxall, L. J. (2020). The links between the Madden-Julian Oscillation and European weather regimes. *Theoretical and Applied Climatology*, *141*(1–2), 567–586. https://doi.org/10.1007/s00704-020-03223-2

Limbach, S., Schömer, E., & Wernli, H. (2012). Detection, tracking and event localization of jet stream features in 4-D atmospheric data. *Geoscientific Model Development*, *5*(2), 457–470. https://doi.org/10.5194/gmd-5-457-2012

Lorenz, E. N. (1963). Deterministic Nonperiodic Flow. *Journal of the Atmospheric Sciences*, *20*(2), 130–141. https://doi.org/10.1175/1520-0469(1963)020⟨0130:dnf⟩2.0.co;2

MacLachlan, C., Arribas, A., Peterson, K. A., Maidens, A., Fereday, D., Scaife, A. A., Gordon, M., Vellinga, M., Williams, A., Comer, R. E., Camp, J., Xavier, P., & Madec, G. (2014). Global Seasonal forecast system version 5 (GloSea5): a high-resolution seasonal forecast system. *Quarterly Journal of the Royal Meteorological Society*, *141*(689), 1072–1084. https://doi.org/10.1002/qj.2396

Madonna, E., Li, C., Grams, C. M., & Woollings, T. (2017). The link between eddy-driven jet variability and weather regimes in the North Atlantic-European sector. *Quarterly Journal of the Royal Meteorological Society*, *143*(708), 2960–2972. https://doi.org/10.1002/qj.3155

Manney, G. L., Hegglin, M. I., Daffer, W. H., Schwartz, M. J., Santee, M. L., & Pawson, S. (2014). Climatology of Upper Tropospheric–Lower

Stratospheric (UTLS) Jets and Tropopauses in MERRA. *Journal of Climate*, *27*(9), 3248–3271. https://doi.org/10.1175/jcli-d-13-00243.1

Marcheggiani, A., Robson, J., Monerie, P.-A., Bracegirdle, T. J., & Smith, D. (2023). Decadal Predictability of the North Atlantic Eddy-Driven Jet in Winter. *Geophysical Research Letters*, *50*(8). https://doi.org/10.1029/2022gl102071

Matthewman, N. J., Esler, J. G., Charlton-Perez, A. J., & Polvani, L. M. (2009). A New Look at Stratospheric Sudden Warmings. Part III: Polar Vortex Evolution and Vertical Structure. *Journal of Climate*, *22*(6), 1566–1585. https://doi.org/10.1175/2008jcli2365.1

Maycock, A. C., Masukwedza, G. I. T., Hitchcock, P., & Simpson, I. R. (2020). A Regime Perspective on the North Atlantic Eddy-Driven Jet Response to Sudden Stratospheric Warmings. *Journal of Climate*, *33*(9), 3901–3917. https://doi.org/10.1175/jcli-d-19-0702.1

McKenna, C. M., & Maycock, A. C. (2021). Sources of Uncertainty in Multimodel Large Ensemble Projections of the Winter North Atlantic Oscillation [e2021GL093258 2021GL093258]. *Geophysical Research Letters*, *48*(14), e2021GL093258. https://doi.org/https://doi.org/10.1029/2021GL093258

Mellado-Cano, J., Barriopedro, D., García-Herrera, R., Trigo, R. M., & Hernández, A. (2019). Examining the North Atlantic Oscillation, East Atlantic Pattern, and Jet Variability since 1685. *Journal of Climate*, *32*(19), 6285–6298. https://doi.org/10.1175/jcli-d-19-0135.1

Messori, G., & Caballero, R. (2015). On double Rossby wave breaking in the North Atlantic. *Journal of Geophysical Research: Atmospheres*, *120*(21), 11, 129–11, 150. https://doi.org/https://doi.org/10.1002/2015JD023854

Novak, L., Ambaum, M. H. P., & Tailleux, R. (2015). The Life Cycle of the North Atlantic Storm Track. *Journal of the Atmospheric Sciences*, *72*(2), 821–833. https://doi.org/10.1175/JAS-D-14-0082.1

O'Reilly, C. H. (2025). Signal-to-noise errors in early winter Euro-Atlantic predictions linked to weak ENSO teleconnections and pervasive jet biases. *Quarterly Journal of the Royal Meteorological Society*. https://doi.org/10.1002/qj.4952

O'Reilly, C. H., Drouard, M., Ayarzagüena, B., Ambaum, M. H. P., & Methven, J. (2024). The role of storm-track dynamics in the intraseasonal variability of the winter ENSO teleconnection to the North Atlantic. *Quarterly Journal of the Royal Meteorological Society*, *150*(761), 2069–2086. https://doi.org/10.1002/qj.4691

O'Sullivan, D., & Salby, M. L. (1990). Coupling of the Quasi-biennial Oscillation and the Extratropical Circulation in the Stratosphere through Planetary Wave Transport. *Journal of the Atmospheric Sciences*, *47*(5), 650–673. https://doi.org/10.1175/1520-0469(1990)047⟨0650:cotqbo⟩2.0.co;2

Oudar, T., Cattiaux, J., & Douville, H. (2020). Drivers of the Northern Extratropical Eddy-Driven Jet Change in CMIP5 and CMIP6 Models. *Geophysical Research Letters*, *47*(8). https://doi.org/10.1029/2019gl086695

Pahlavan, H. A., Fu, Q., Wallace, J. M., & Kiladis, G. N. (2021). Revisiting the Quasi-Biennial Oscillation as Seen in ERA5. Part I: Description and Momentum Budget. *Journal of the Atmospheric Sciences*, *78*(3), 673–691. https://doi.org/10.1175/jas-d-20-0248.1

Parfitt, R., & Kwon, Y.-O. (2020). The Modulation of Gulf Stream Influence on the Troposphere by the Eddy-Driven Jet. *Journal of Climate*, *33*(10), 4109–4120. https://doi.org/10.1175/jcli-d-19-0294.1

Parker, T., Woollings, T., Weisheimer, A., O'Reilly, C., Baker, L., & Shaffrey, L. (2019). Seasonal Predictability of the Winter North At-

lantic Oscillation From a Jet Stream Perspective. *Geophysical Research Letters*, *46*(16), 10159–10167. https://doi.org/10.1029/2019gl084402

Peings, Y., & Magnúsdóttir, G. (2014). "Forcing of the Wintertime Atmospheric Circulation by the Multidecadal Fluctuations of the North Atlantic Ocean". *Environmental Research Letters*. https://doi.org/10.1088/1748-9326/9/3/034018

Perez, J., Maycock, A. C., Griffiths, S. D., Hardiman, S. C., & McKenna, C. M. (2024). A new characterisation of the North Atlantic eddy-driven jet using two-dimensional moment analysis. *Weather and Climate Dynamics*, *5*(3), 1061–1078. https://doi.org/10.5194/wcd-5-1061-2024

Rossby, C.-G. (1939). Relation between variations in the intensity of the zonal circulation of the atmosphere and the displacements of the semi-permanent centers of action. *Journal of Marine Research*, *2*(1), 38–55. https://doi.org/10.1357/002224039806649023

Royal Meteorological Society. (2025). Figure 1: A cross section through the atmosphere showing air rising and forming deep clouds at the Intertropical Convergence Zone, and the Hadley, Ferrel and Polar cells [In Depth – The Global Atmospheric Circulation. Accessed 2025-05-30].

Saffin, L., McKenna, C. M., Bonnet, R., & Maycock, A. C. (2024). Large Uncertainties When Diagnosing the "Eddy Feedback Parameter" and Its Role in the Signal-To-Noise Paradox. *Geophysical Research Letters*, *51*(11). https://doi.org/10.1029/2024gl108861

Scaife, A. A., Arribas, A., Blockley, E., Brookshaw, A., Clark, R. T., Dunstone, N., Eade, R., Fereday, D., Folland, C. K., Gordon, M., Hermanson, L., Knight, J. R., Lea, D. J., MacLachlan, C., Maidens, A., Martin, M., Peterson, A. K., Smith, D., Vellinga, M., … Williams, A. (2014). Skillful long-range prediction of European and North

American winters. *Geophysical Research Letters*, *41*(7), 2514–2519. https://doi.org/10.1002/2014gl059637

Scaife, A. A., & Smith, D. (2018). A signal-to-noise paradox in climate science. *npj Climate and Atmospheric Science*, *1*(1). https://doi.org/10.1038/s41612-018-0038-4

Simpson, I. R., Bacmeister, J., Neale, R. B., Hannay, C., Gettelman, A., Garcia, R. R., Lauritzen, P. H., Marsh, D. R., Mills, M. J., Medeiros, B., & Richter, J. H. (2020). An Evaluation of the Large-Scale Atmospheric Circulation and Its Variability in CESM2 and Other CMIP Models. *Journal of Geophysical Research: Atmospheres*, *125*(13). https://doi.org/10.1029/2020jd032835

Simpson, I. R., Yeager, S. G., McKinnon, K. A., & Deser, C. (2019). Decadal predictability of late winter precipitation in western Europe through an ocean–jet stream connection. *Nature Geoscience*, *12*(8), 613–619. https://doi.org/10.1038/s41561-019-0391-x

Skinner, D. T., Matthews, A. J., & Stevens, D. P. (2022). North Atlantic Oscillation response to the Madden–Julian Oscillation in a coupled climate model. *Weather*, *77*(6), 201–205. https://doi.org/10.1002/wea.4215

Spensberger, C., Li, C., & Spengler, T. (2023). Linking Instantaneous and Climatological Perspectives on Eddy-Driven and Subtropical Jets. *Journal of Climate*, *36*(24), 8525–8537. https://doi.org/10.1175/jcli-d-23-0080.1

Spensberger, C., Spengler, T., & Li, C. (2017). "Upper-Tropospheric Jet Axis Detection and Application to the Boreal Winter 2013/14". *Monthly Weather Review*, *145*(6), 2363–2374. https://doi.org/10.1175/MWR-D-16-0467.1

Strommen, K. (2019). Jet Latitude Regimes and the Predictability of the North Atlantic Oscillation. *Quarterly Journal of the Royal Meteorological Society*. http://arxiv.org/abs/1910.00864

Strommen, K. (2020). Jet latitude regimes and the predictability of the North Atlantic Oscillation. *Quarterly Journal of the Royal Meteorological Society*, *146*(730), 2368–2391. https://doi.org/10.1002/qj.3796

Strommen, K., & Palmer, T. N. (2018). Signal and noise in regime systems: A hypothesis on the predictability of the North Atlantic Oscillation. *Quarterly Journal of the Royal Meteorological Society*, *145*(718), 147–163. https://doi.org/10.1002/qj.3414

Strommen, K., Woollings, T., Davini, P., Ruggieri, P., & Simpson, I. R. (2023). Predictable decadal forcing of the North Atlantic jet speed by sub-polar North Atlantic sea surface temperatures. *Weather and Climate Dynamics*, *4*(4), 853–874. https://doi.org/10.5194/wcd-4-853-2023

Strong, C., & Magnusdottir, G. (2008). Tropospheric Rossby Wave Breaking and the NAO/NAM. *Journal of the Atmospheric Sciences*, *65*(9), 2861–2876. https://doi.org/10.1175/2008jas2632.1

Thornton, H. E., Smith, D. M., Scaife, A. A., & Dunstone, N. J. (2023). Seasonal Predictability of the East Atlantic Pattern in Late Autumn and Early Winter. *Geophysical Research Letters*, *50*(1). https://doi.org/10.1029/2022gl100712

Toniazzo, T., & Scaife, A. A. (2006). The influence of ENSO on winter North Atlantic climate. *Geophysical Research Letters*, *33*(24). https://doi.org/10.1029/2006gl027881

Tung & Rosenthal. (1985). Theories of Multiple Equilibria-A Critical Reexamination. Part I: Barotropic Models. *Journal of Atmospheric Sciences, vol. 42, Issue 24, pp.2804-2819*, *53*(9), 1689–1699. 10.1175/1520-0469(1985)042%3C2804:TOMEAC%3E2.0.CO;2

Tung & Rosenthal. (1987). Theories of Multiple Equilibria-A Critical Reexamination. Part I: Barotropic Models. *Journal of Atmospheric Sci-*

ences, vol. 42, Issue 24, pp.2804-2819, *53*(9), 1689–1699. 10.1175/1520-0469(1985)042%3C2804:TOMEAC%3E2.0.CO;2

UC-Davis Climate Dynamics ATM 241 Course Materials. (2025). Zonal-mean zonal wind speed from ncep/ncar reanalysis (annual climatology, djf, jja).

Vallis, G. K. (2017, June). *Atmospheric and Oceanic Fluid Dynamics: Fundamentals and Large-Scale Circulation*. Cambridge University Press. https://doi.org/10.1017/9781107588417

van der Wiel, K., Bloomfield, H. C., Lee, R. W., Stoop, L. P., Blackport, R., Screen, J. A., & Selten, F. M. (2019). The influence of weather regimes on European renewable energy production and demand. *Environmental Research Letters*, *14*(9), 094010. https://doi.org/10.1088/1748-9326/ab38d3

Vautard, R. (1990). Multiple Weather Regimes over the North Atlantic: Analysis of Precursors and Successors. *Monthly Weather Review*, *118*(10), 2056–2081. https://doi.org/10.1175/1520-0493(1990)118⟨2056:mwrotn⟩2.0.co;2

Wallace, J. M., & Gutzler, D. S. (1981). Teleconnections in the Geopotential Height Field during the Northern Hemisphere Winter. *Monthly Weather Review*, *109*(4), 784–812. https://doi.org/10.1175/1520-0493(1981)109⟨0784:titghf⟩2.0.co;2

Waugh, D. N. W. (1997). Elliptical diagnostics of stratospheric polar vortices. *Quarterly Journal of the Royal Meteorological Society*, *123*(542), 1725–1748. https://doi.org/10.1002/qj.49712354213

Waugh, D. W., & Randel, W. J. (1999). Climatology of Arctic and Antarctic Polar Vortices Using Elliptical Diagnostics. *Journal of the Atmospheric Sciences*, *56*(11), 1594–1613. https://doi.org/10.1175/1520-0469(1999)056⟨1594:coaaap⟩2.0.co;2

Weisheimer, A., Baker, L. H., Bröcker, J., Garfinkel, C. I., Hardiman, S. C., Hodson, D. L. R., Palmer, T. N., Robson, J. I., Scaife, A. A., Screen,

J. A., Shepherd, T. G., Smith, D. M., & Sutton, R. T. (2024). The Signal-to-Noise Paradox in Climate Forecasts: Revisiting Our Understanding and Identifying Future Priorities. *Bulletin of the American Meteorological Society*, *105*(3), E651–E659. https://doi.org/10.1175/bams-d-24-0019.1

Wheeler, M. C., & Hendon, H. H. (2004). An All-Season Real-Time Multivariate MJO Index: Development of an Index for Monitoring and Prediction. *Monthly Weather Review*, *132*(8), 1917–1932. https://doi.org/10.1175/1520-0493(2004)132⟨1917:aarmmi⟩2.0.co;2

White, R. H., Hilgenbrink, C., & Sheshadri, A. (2019). The Importance of Greenland in Setting the Northern Preferred Position of the North Atlantic Eddy-Driven Jet. *Geophysical Research Letters*, *46*(23), 14126–14134. https://doi.org/10.1029/2019gl084780

Woollings, T., Barnes, E., Hoskins, B., Kwon, Y.-O., Lee, R. W., Li, C., Madonna, E., McGraw, M., Parker, T., Rodrigues, R., Spensberger, C., & Williams, K. (2018). Daily to Decadal Modulation of Jet Variability. *Journal of Climate*, *31*(4), 1297–1314. https://doi.org/10.1175/jcli-d-17-0286.1

Woollings, T., & Blackburn, M. (2012). The North Atlantic Jet Stream under Climate Change and Its Relation to the NAO and EA Patterns. *Journal of Climate*, *25*(3), 886–902. https://doi.org/10.1175/jcli-d-11-00087.1

Woollings, T., Hannachi, A., & Hoskins, B. (2010). Variability of the North Atlantic eddy-driven jet stream. *Quarterly Journal of the Royal Meteorological Society*. https://doi.org/10.1002/qj.625

Woollings, T., Hoskins, B., Blackburn, M., & Berrisford, P. (2008). A New Rossby Wave–Breaking Interpretation of the North Atlantic Oscillation. *Journal of the Atmospheric Sciences*, *65*(2), 609–626. https://doi.org/10.1175/2007jas2347.1

Yuan, J., Feldstein, S. B., Lee, S., & Tan, B. (2011). The Relationship between the North Atlantic Jet and Tropical Convection over the Indian and Western Pacific Oceans. *Journal of Climate*, *24*(23), 6100–6113. https://doi.org/10.1175/2011jcli4203.1